

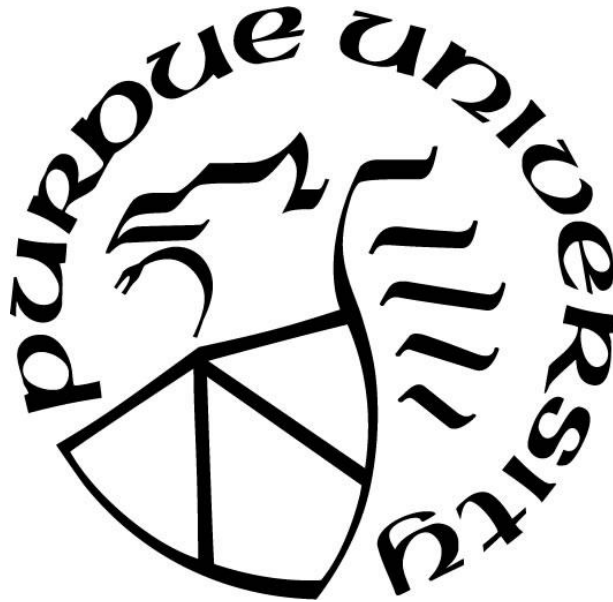
**REAL-TIME VISUALIZATION OF FIBER/MATRIX INTERFACIAL
DEBONDING BEHAVIOR**

by
Jou-Mei Chu

A Dissertation

*Submitted to the Faculty of Purdue University
In Partial Fulfillment of the Requirements for the degree of*

Doctor of Philosophy



School of Aeronautics & Astronautics

West Lafayette, Indiana

December 2018

**THE PURDUE UNIVERSITY GRADUATE SCHOOL
STATEMENT OF COMMITTEE APPROVAL**

Dr. Weinong Chen, Chair

School of Aeronautics and Astronautics

Dr. Jeffrey Youngblood

School of Materials Engineering

Dr. Michael Sangid

School of Aeronautics and Astronautics

Dr. Tyler Tallman

School of Aeronautics and Astronautics

Approved by:

Dr. Weinong Chen

Head of the Graduate Program

I would like to dedicate this dissertation to my family (Dad, Mom, sister) and loved ones who have helped and supported me throughout my research career.

ACKNOWLEDGMENTS

I would like to thank my financial support from JHU/MEDE/ARL (Army Research Laboratory and was accomplished under Cooperative Agreement Number W911NF-12-2-0022) program for my PhD career. I thank the MEDE program for giving me the opportunity to interact with other researchers in the field in person during our meetings (Fall meetings, MACH conferences, Summer meetings, and bi-weekly meetings). I thank the MEDE program for giving me a chance to be on the program's video interview.

I thank Applied Poleramic Inc for providing SC-15 epoxy – epoxy used in the current study.

I thank the APS Beamline scientists (Dr. Tao Sun, Dr. Kamel Fezzaa, Dr. Niranjana Parab, and Alex Deriy) for their professional help to make my experiments successful.

I also like to thank Dr. Daniel O'Brien, Dr. Chian-Fong Yen, and Dr. Brady Aydelotte from ARL for their input to my PhD work.

I would also like to thank my lab mates (Dr. Ben Claus, Boon Him Lim, Yizhou Nie, Dr. Waterloo Tsutsui, Dr. Hangjie Liao, Zherui Guo, and Nesredin Kadir) for their help and collaboration during my graduate study.

I thank my committee members, Prof. Jeffrey Youngblood, Prof. Michael Sangid, and Prof. Tyler Tallman, for their input and guidance to my PhD research.

Last and most importantly, I sincerely thank my advisor, Prof. Weinong Chen, for being my guidance and mentor throughout my graduate career. I thank him for taking me as his student when I knew nothing about Kolsky bars. I thank him for training me to become an independent scientist/engineer who can not only manage her own projects and tasks but also collaborate and work with others in the field. I thank him for giving me the confidence to step into the real world.

TABLE OF CONTENTS

LIST OF TABLES	7
LIST OF FIGURES	8
ABSTRACT	14
CHAPTER 1. INTRODUCTION	15
1.1 Applications of Fiber Reinforced Polymer Composites	15
1.2 Major Types of Fiber Reinforced Polymer Composites	15
1.3 Summary	16
CHAPTER 2. LITERATURE REVIEW AND RESEARCH GAP	18
2.1 Motivation	18
2.2 Types of Interfacial Debonding Test Methods	19
2.3 Interfacial Transverse Debonding	19
2.4 Interfacial Shear Debonding	26
2.5 Crack Velocity and Wave Speeds	28
2.6 Split-Hopkinson (Kolsky) Bars	29
2.6.1 Modified Kolsky Bar in This Research	30
2.6.2 Data Reduction	31
2.7 Research Gap	32
CHAPTER 3. EXPERIMENTAL METHODS	34
3.1 Dynamic Transverse Loading Experiments	34
3.1.1 High-Speed Synchrotron X-ray PCI	34
3.1.2 Modified Tension Kolsky Bar (in Beam line 32-ID-B)	36
3.1.3 Modified Tension Kolsky Bar (in ARMS B130, Purdue University)	37
3.2 Quasi-Static Transverse Loading Experiments	38
CHAPTER 4. MATERIALS AND SPECIMEN PREPARATION	41
4.1 Materials	41
4.2 Specimen Preparation	42
CHAPTER 5. RESULTS AND DISCUSSION	45
5.1 High-Speed Images with Corresponding Force History	47
5.2 Average Peak Debonding Force	58

5.3	Average Interfacial Crack Velocity	64
5.4	Average Interfacial Debonding Crack Geometry	68
5.5	Failure Surface of the Recovered Cruciform Specimens.....	74
CHAPTER 6. DYNAMIC VISUALIZATION OF INTERFACIAL SHEAR DEBONDING .		80
6.1	Abstract.....	81
6.2	Introduction.....	81
6.3	Materials and Methods.....	83
6.4	Results.....	88
6.5	Discussion.....	101
6.6	Conclusions.....	104
6.7	Acknowledgements.....	105
6.8	Conflicts of Interest.....	105
6.9	References.....	105
CHAPTER 7. CONCLUSIONS.....		109
CHAPTER 8. FUTURE WORK.....		111
8.1	Cross-Section View of the Cruciform Specimen Across the Fiber Diameter	111
8.2	Interfacial Stress Analysis and Fracture Mechanics	114
8.3	Curing and Post-Curing Effect of The Debonding Mechanisms	114
8.4	Mixed-Mode/Multi-Fiber/Toughened Epoxy Cruciform Experiments	115
APPENDIX.....		117
REFERENCES		123
VITA.....		129
PUBLICATIONS.....		131

LIST OF TABLES

Table 4.1. Material properties for S-2 glass, KM2, tungsten, and SC-15 epoxy	41
Table 5.1. Results obtained for the various fiber reinforced specimens at 0.25 mm/s and 2.5 m/s	60
Table 5.2. Anderson-Darling normality tests for peak debonding forces.....	64
Table 5.3. t-tests for peak debonding forces comparing different reinforced specimens	64
Table 5.4. t-tests for peak debonding forces comparing rate difference (0.25 mm/s and 2.5 m/s).....	64
Table 5.5. Percentage of the average crack speed of the different reinforced specimens to the Rayleigh wave speed of the epoxy	67
Table 5.6. Anderson-Darling normality tests for crack velocities	67
Table 5.7. t-tests for crack velocity comparing different reinforced specimens.....	67
Table 5.8. t-tests for peak debonding forces comparing rate difference (0.25 mm/s and 2.5 m/s).....	68
Table 6.1. Peak forces and interfacial shear stresses for the four studied fiber materials at 2.5 and 5.0 m s ⁻¹ averaged across all experiments.	90
Table 6.2. P-values from the Anderson-Darling normality test.....	103

LIST OF FIGURES

Figure 2.1. Upon impact, the fiber reinforced polymer composite plate undergoes penetration, transition, and perforation. Reprinted from [6], Copyright (2011), with permission from Elsevier.	18
Figure 2.2. Various testing methods to study the fiber/matrix interfacial debonding behavior of a single fiber reinforced polymer specimen.....	19
Figure 2.3. Angular stress distribution for (a) radial normal, (b) tangential normal, and (c) tangential shear stresses for a single fiber reinforced cruciform specimen loaded in transverse tension along $\theta = 0^\circ$. Reprinted from [25], Copyright (1999), with permission from Elsevier.....	21
Figure 2.4. Three interfacial failure mechanisms suggested by Gundel <i>et al.</i> Reprinted from [25], Copyright (1999), with permission from Elsevier.	21
Figure 2.5. Visualization of the interfacial debonding in (a) 30° off-axis specimen, (b) 45° off-axis specimen, and (c) 60° off-axis specimen and (d) debonded area along the fiber/matrix interface. Reprinted from [17]. Copyright (2002), with permission from Sage Journals.	22
Figure 2.6. A schematic of the cross-section of the modeled multi-fiber cruciform specimen. Reprinted by permission Springer Nature, Experimental Mechanics [26], Copyright (2006).	23
Figure 2.7. A schematic of the experimental setup for the reflective light testing technique. Reprinted by permission Springer Nature, Experimental Mechanics [26], Copyright (2006).	24
Figure 2.8. (a) A schematic of the experimental setup for the cruciform experiments. (b-d) images of the crack with height h at different forces. (e) A schematic of the cross-section across the fiber diameter showing the debonding angle evaluation scheme. Reprinted from [27], Copyright (2016), with permission from Elsevier.	25
Figure 2.9. A schematic of a traditional tension Kolsky bar.	30
Figure 2.10. A schematic of the modified tension Kolsky bar where the transmission bar of the traditional Kolsky bar is replaced by a load cell fixed on a stage.....	30
Figure 2.11. A schematic of the specimen section upon loading.....	31
Figure 3.1. A schematic of the high-speed synchrotron X-ray with Kolsky bars setup.	35

Figure 3.2. A panoramic view of the experimental apparatus in Beamline 32-ID-B hutch, APS.	36
Figure 3.3. A schematic of the experimental setup (modified tension Kolsky bar) in Beamline 32-ID-B hutch, APS. Reprinted by permission from Springer Nature, Journal of Materials Science [47], Copyright (2017).....	37
Figure 3.4. A picture of the experimental setup in Purdue.	38
Figure 3.5. Images of the quasi-static experimental setup with the laser back-light imaging technique with a quasi-static load frame.....	39
Figure 3.6. A schematic of the quasi-static experimental setup.	40
Figure 4.1. Cruciform specimen (a) and (b) preparation setup and (c) geometry.	44
Figure 5.1. A schematic of the cruciform specimen upon loading.	45
Figure 5.2. A schematic of the two imaging views: high-speed imaging and SEM imaging.....	46
Figure 5.3. Force-displacement history and force-time-crack length history with the corresponding high-speed images sequence of S-2 glass fiber reinforced cruciform specimen at 2.5 m/s. The scale bar on the initial frame indicates 250 μm	50
Figure 5.4. Force-displacement history and force-time-crack length history with the corresponding high-speed images sequence of S-2 glass fiber reinforced cruciform specimen at 2.5 m/s.	51
Figure 5.5. Force-displacement history and force-time-crack length history with the corresponding high-speed images sequence of S-2 glass fiber reinforced cruciform specimen at 2.5 m/s. The scale bar on the initial frame indicates 0.5 mm.	52
Figure 5.6. Force-displacement and force-time histories with the corresponding high-speed images sequence of S-2 glass fiber reinforced cruciform specimen at 0.25 mm/s. The scale bar on the initial frame indicates 0.5 mm.....	53
Figure 5.7. Force-displacement history and force-time-crack length history with the corresponding high-speed images sequence of KM2 fiber reinforced cruciform specimen at 2.5 m/s. The scale bar on the initial frame indicates 0.5 mm.	54
Figure 5.8. Force-displacement and force-time histories with the corresponding high-speed images sequence of KM2 fiber reinforced cruciform specimen at 0.25 mm/s. The scale bar on the initial frame indicates 0.5 mm.	55

Figure 5.9. Force-displacement history and force-time-crack length history with the corresponding high-speed images sequence of tungsten reinforced cruciform specimen at 2.5 m/s. The scale bar on the initial frame indicates 0.5 mm.	56
Figure 5.10. Force-displacement and force-time histories with the corresponding high-speed images sequence of tungsten reinforced cruciform specimen at 0.25 mm/s. The scale bar on the initial frame indicates 0.5 mm.....	57
Figure 5.11. Average peak debonding force for S-2 glass, KM2, and tungsten fiber reinforced cruciform specimens at 0.25 mm/s and 2.5 m/s.....	59
Figure 5.12. Force-displacement responses of S-2 glass fiber reinforced cruciform specimen at 0.25 mm/s and 2.5 m/s.....	62
Figure 5.13. Force-displacement responses of KM2 fiber reinforced cruciform specimen at 0.25 mm/s and 2.5 m/s.....	62
Figure 5.14. Force-displacement responses of tungsten fiber reinforced cruciform specimen at 0.25 mm/s and 2.5 m/s.....	63
Figure 5.15. Average crack velocity for S-2 glass, KM2, and tungsten fiber reinforced cruciform specimens at 0.25 mm/s and 2.5 m/s.....	66
Figure 5.16. Average crack length as a function of time for S-2 glass fiber reinforced cruciform specimens at 0.25 mm/s and 2.5 m/s.....	68
Figure 5.17. Average crack length as a function of time for KM2 fiber reinforced cruciform specimens at 0.25 mm/s and 2.5 m/s.....	69
Figure 5.18. Average crack length as a function of time for tungsten fiber reinforced cruciform specimens at 0.25 mm/s and 2.5 m/s.....	69
Figure 5.19. Average crack width as a function of time for S-2 glass fiber reinforced cruciform specimens at 0.25 mm/s and 2.5 m/s.....	70
Figure 5.20. Average crack width as a function of time for KM2 fiber reinforced cruciform specimens at 0.25 mm/s and 2.5 m/s.....	71
Figure 5.21. Ideal elliptical crack geometry progression obtained from the measured average crack length and width from $t = 0.2 \mu\text{s}$ to $t = 2 \mu\text{s}$ for S-2 glass reinforced cruciform specimens.	71

Figure 5.22. Ideal elliptical crack geometry progression obtained from the measured average crack length and width from $t = 0.2 \mu\text{s}$ to $t = 2 \mu\text{s}$ for KM2 glass reinforced cruciform specimens.	72
Figure 5.23. A schematic of the cross-section view of the cruciform specimen (fixed on the right-hand side and loaded on the left-hand side).	73
Figure 5.24. SEM imaging of the recovered S-2 glass fiber reinforced cruciform specimen at 2.5 m/s.	77
Figure 5.25. SEM imaging of the recovered S-2 glass fiber reinforced cruciform specimen at 0.25 mm/s.	77
Figure 5.26. SEM imaging of the recovered KM2 fiber reinforced cruciform specimen at 2.5 m/s and 0.25 mm/s.	78
Figure 5.27. SEM imaging of the recovered tungsten reinforced cruciform specimen at 2.5 m/s and 0.25 mm/s.	79
Figure 6.1. A schematic of S-2 glass, tungsten, and steel sample preparation. The two ends of the fiber were fixed in place by epoxy adhesives (DP 190 for S-2 glass and tungsten samples and JB Weld for steel samples) and SC-15 epoxy bead was formed on the center of the fiber. Prior to every experiment, the right-hand side of the sample was snipped away along the dashed lines. (b) Fiber material (with epoxy bead on the fiber) placed across a cardboard strip on top of a slotted aluminum bar.	85
Figure 6.2. (a) Sample preparation for Z-pin. OOMOO [®] 30 pourable silicone rubber was poured in the aluminum mold. Once cured, the silicone rubber was used to prepare the Z-pin samples. (b) The Z-pin was held in place by machined Teflon cylinders.	85
Figure 6.3. A schematic of the experimental setup in APS Beam line 32 ID-B. The section circled indicates the sample section which is further illustrated in Figs. 4 and 5.	87
Figure 6.4. Schematic of S-2 glass fiber, tungsten, and steel sample setup. The square around the epoxy bead indicates the X-ray window.	88
Figure 6.5. Schematic of Z-pin sample setup. The square around the epoxy bead indicates the X-ray window.	88

- Figure 6.6. Force-time response and the corresponding pull-out image sequence of S-2 glass fiber at 2.5 m s^{-1} with 1 million frames per second recording speed with 200 ns exposure time per frame and a $20\times$ lens. Epoxy bead residues were observed in front of and behind the bead which could be the cause of slope changes in the force history. The bead pointed to by the arrows allows us to track the debonding initiation and progression. 91
- Figure 6.7. Force-time response and the corresponding pull-out image sequence of S-2 glass fiber at 5.0 m s^{-1} with 2 million frames per second recording speed with 200 ns exposure time per frame and a $20\times$ lens. The bead pointed by the arrows allows us to track the debonding initiation and progression. 92
- Figure 6.8. Force-time response and the corresponding pull-out image sequence of tungsten wire at 2.5 m s^{-1} with 1 million frames per second recording speed with 200 ns exposure time per frame and a $20\times$ lens. The regions pointed by an arrow indicate the appearance of cracks. 93
- Figure 6.9. (a) A typical force-time response of catastrophic debonding mechanism of tungsten wire at 2.5 m s^{-1} and (b) 5.0 m s^{-1} 94
- Figure 6.10. Force-time response and the corresponding pull-out image sequence of tungsten wire at 5.0 m s^{-1} with 1 million frames per second recording speed with 200 ns exposure time per frame and a $20\times$ lens. The regions pointed by an arrow indicate the appearance of cracks. 94
- Figure 6.11. Force-time response and the corresponding pull-out image sequence of steel wire at 2.5 m s^{-1} with 1 million frames per second recording speed with 200 ns exposure time per frame and a $20\times$ lens. The regions pointed by an arrow indicate the appearance of cracks. 95
- Figure 6.12. A typical force-time response of stick-slip debonding mechanism of tungsten wire at 2.5 m s^{-1} and (b) a typical force-time response of catastrophic debonding mechanism of tungsten wire at 5.0 m s^{-1} 96
- Figure 6.13. Force-time response and the corresponding pull-out image sequence of steel wire at 5.0 m s^{-1} with 1 million frames per second recording speed with 200 ns exposure time per frame and a $20\times$ lens. The regions pointed by an arrow indicate the appearance of cracks. 96

- Figure 6.14. Force-time response and the corresponding pull-out image sequence of Z-pin at 2.5 m s^{-1} with 1 million frames per second recording speed with 200 ns exposure time per frame and a $10\times$ lens. The regions pointed by an arrow indicate the appearance of cracks. The diameter of the pin is also indicated in (a)..... 97
- Figure 6.15. Force-time response and the corresponding pull-out image sequence of Z-pin at 5.0 m s^{-1} with 1 million frames per second recording speed with 200 ns exposure time per frame and a $10\times$ lens. The regions pointed by an arrow indicate the appearance of cracks. The diameter of the pin is also indicated in (a)..... 98
- Figure 6.16. Force-time response and the corresponding pull-out image sequence of tungsten wire at 2.5 m s^{-1} with 1 million frames per second recording speed with 200 ns exposure time per frame and a $5\times$ lens..... 99
- Figure 6.17. Force-time response and the corresponding pull-out image sequence of steel wire at 2.5 m s^{-1} with 1 million frames per second recording speed with 200 ns exposure time per frame and a $5\times$ lens..... 99
- Figure 6.18. Failure surface of recovered epoxy beads and fiber materials examined via a NovaNano SEM..... 101
- Figure 8.1. Three view-points of the cruciform specimen: (a) high-speed imaging view, (b) SEM imaging view, and (c) cross-section across the fiber diameter view 113

ABSTRACT

Author: Chu, Jou-Mei (Jocelyn). PhD

Institution: Purdue University

Degree Received: December 2018

Title: Real-Time Visualization of Fiber/Matrix Interfacial Debonding Behavior

Committee Chair: Weinong Chen

The rate effect of fiber-matrix interfacial debonding behavior of SC-15 epoxy and various fiber reinforcements was studied via in-situ visualization of the debonding event. Special focus has been placed on the dynamic transverse debonding of single fiber reinforced polymer composites. In this study, the debonding force history, debonding initiation, debonding crack velocity, and crack geometry were characterized using a quasi-static load frame and a modified tension Kolsky bar at loading velocities of 0.25 mm/s and 2.5 m/s. Cruciform-shaped specimens were used for interfacial transverse debonding between SC-15 epoxy matrix and various fiber reinforcements including S-2 glass, Kevlar[®] KM2, and tungsten fiber materials. The load history and high-speed images of the debonding event were simultaneously recorded. A major increase was observed for the average peak debonding force and a minor increase was observed for the average crack velocity with increasing loading velocity. The crack geometry of the cruciform specimens under both loading velocities was also tracked. Scanning electron microscopy of the recovered specimens revealed the debonding direction along the fiber-matrix interface through angled patterns on the failure surface.

The dynamic shear debonding of single fiber reinforced plastic composites were also studied via the real-time visualization with the fiber pull-out method. The interfacial shear debonding was studied between SC-15 epoxy and fiber reinforcements including S-2 glass, tungsten, steel, and carbon composite Z-pin fiber materials at 2.5 m/s and 5.0 m/s. Both S-2 glass fiber and Z-pin experienced catastrophic interfacial debonding whereas tungsten and steel wire experienced both catastrophic debonding and stick-slip behavior. Scanning electron microscope imaging of recovered epoxy beads revealed a snap-back behavior around the meniscus region of the bead for S-2 glass, tungsten, and steel fiber materials at 5.0 m/s whereas those at 2.5 m/s exhibited no snap-back behavior.

CHAPTER 1. INTRODUCTION

1.1 Applications of Fiber Reinforced Polymer Composites

Fiber reinforced polymer composites are widely used from commercial to military applications due to their high strength-to-weight ratios and high impact resistance. Commercial aircraft such as the Boeing 787 Dreamliner is composed of approximately 50% of composite materials [1]. The novel jet, Boeing 777X, contains fiberglass reinforced polymer composite foldable winglets whereas the main wing bodies contain carbon fiber reinforced polymer composites. To reduced weight, automobiles and bicycles are also using fiber-reinforced polymer composites. For military applications, fiber reinforced polymer composites are utilized in military vehicle hulls, ballistic armor protection systems, and ballistic armors.

Fiber reinforcement is bonded to the polymer matrix in composites. The interface between the fiber and the matrix must be sufficiently strong to transfer load. When load isolation is desired, the interface must fail at a desired load level. Therefore, the understanding of and the ability to control the interfacial behavior is critical in composite material design. However, due to the complexity of composite materials, debonding initiation and propagation are not yet properly understood. Better understanding of the damage initiation and progression is necessary to improve the overall material strength.

1.2 Major Types of Fiber Reinforced Polymer Composites

There are many types of reinforcements for fiber reinforced polymer composites such as glass fiber, carbon fiber, and aramid fiber reinforcements. Different reinforcements have their own characteristics. For instance, glass fiber reinforced polymer composites have characteristics such as corrosion and chemical resistance and good heat and sound insulation [2]. Glass fiber reinforced composites are often found in military vehicle hulls, house buildings, and piping. Carbon fiber reinforced polymer composites have high stiffness and strength, high electrical and thermal conductivities, and high heat resistance [2]. Carbon fiber reinforced polymer composites are often found on aircraft, automobiles, and sports goods. Aramid fiber reinforced polymer composites such as Kevlar have high stiffness and tensile strength as well as fatigue resistance [2]. Aramid

fiber reinforced polymer composites are often found in body armors, helmets, flame-resistant clothing, and jet engine cowlings. The major market for the use of aramid fibers is for military and protection.

With the different types of fiber reinforced polymer composites, one factor remains the same: the importance of the interface between the fiber and matrix. Damage (e.g. debonding, delaminating, fiber/matrix failure) often initiates along this interface leading to material failure. The loss of adhesion at the interface can greatly reduce the material strength. Furthermore, the mechanical performance of fiber reinforced polymer composites is dependent on the interface [3]. Depending on the application of the fiber-reinforced composites, the interfacial properties may vary. For typical structural applications, a stronger bond between the fiber and matrix is desired. On the other hand, a weaker bond is desired for ballistic applications because the interfacial toughness is increased [4].

1.3 Summary

Fiber reinforced polymer composites can be viewed at four structural levels [5]:

1. molecular level – the chemical structure of fiber and matrix based on the Van der Waals forces, acid-base interactions and chemical bonds,
2. fiber level – the interfacial behavior between a single fiber and epoxy matrix based on parameters such as bond strength, interfacial shear strength (stress is not a material behavior), critical energy release rate, etc.,
3. meso level – the distribution of fiber reinforcements in the matrix system, and
4. macro level – the bulk composite material.

This research focused on the fiber level to study the interfacial behavior between a single fiber and an epoxy system.

The goal of this research is to improve the understanding of debonding mechanisms under tensile loading by visualizing the in-situ debonding and failure event. Different reinforcements with SC-15 epoxy matrix were used to perform debonding experiments under both quasi-static and dynamic loading conditions. The focus of the study is on the fiber/matrix interfacial transverse debonding behavior with S-2 glass fiber, KM2 fiber, and tungsten fiber reinforcements. A chapter

(Chapter 6) is dedicated to the fiber/matrix interfacial shear debonding behavior under dynamic loading conditions using a modified tension Kolsky bar with a high-speed synchrotron X-ray phase contrast imaging (PCI). The interfacial transverse dynamic debonding behavior were also performed using a modified tension Kolsky bar integrated with a high-speed synchrotron X-ray PCI as well as a laser back-light imaging technique. For the quasi-static debonding behaviors, the experiments were performed by using a quasi-static load frame integrated with a laser back-light imaging technique.

The dissertation is organized as follows: Chapter 2 provides the research background which includes the interfacial behaviors studied in previous researches and the research gaps. Chapter 3 presents the experimental methods used for the current study including the dynamic and quasi-static experimental setups. Chapter 4 introduces the material and specimen preparation. Results and Discussion are discussed in Chapter 5. Chapter 6 focuses on the fiber/matrix interfacial shear debonding. Chapter 8 summarizes the findings of the current research. Finally, Chapter 7 presents the potential future work of the current research.

CHAPTER 2. LITERATURE REVIEW AND RESEARCH GAP

2.1 Motivation

Fiber reinforced polymer composites are widely used nowadays, specifically those that undergo dynamic impact (e.g. body armors, military vehicle hulls, helmets, rotor blades, engine cowlings, and much more). When a composite plate is subjected to impact, the first few layers (where the projectile impacts first) often exhibit penetration, the middle layers exhibit transition, and the back layers exhibit perforation which includes the interlaminar and intralaminar failure modes, as shown in Figure 2.1 [6]. The interlaminar and intralaminar failure modes include delamination, fiber/matrix debonding, fiber pull-out, and fiber and/or matrix ruptures. The interlaminar and intralaminar failure modes play a crucial part in the energy absorption of the fiber reinforced polymer composites [7]. Thus, whether the bullet can be stopped by the armor/protection system, the last few layers of the composite armor system is of great importance. Thus, it is necessary to understand how the fiber/matrix debonds and fails under high rate loading.

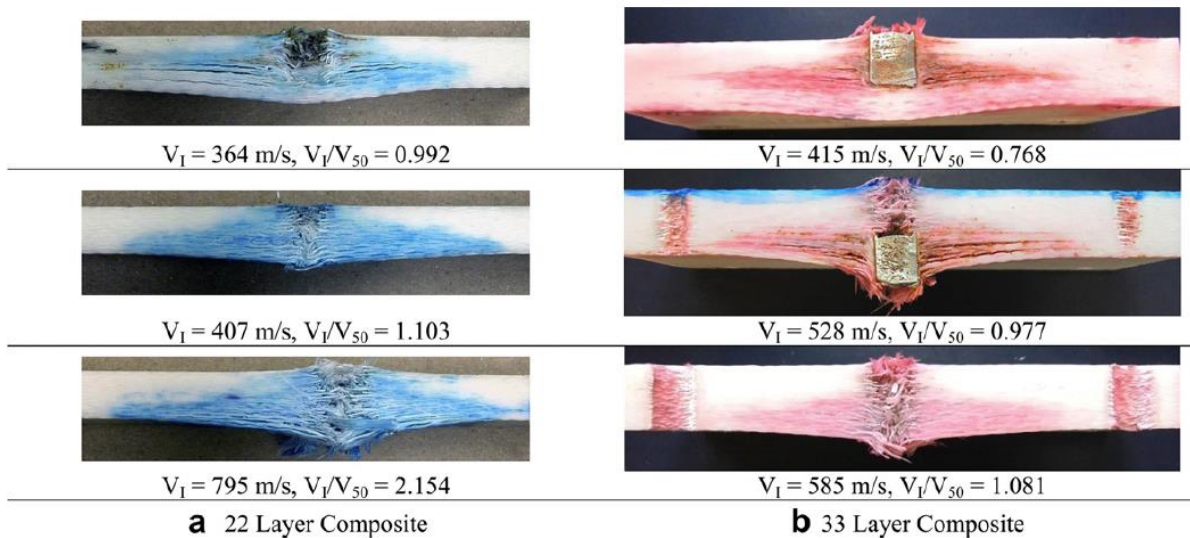


Figure 2.1. Upon impact, the fiber reinforced polymer composite plate undergoes penetration, transition, and perforation. Reprinted from [6], Copyright (2011), with permission from Elsevier.

2.2 Types of Interfacial Debonding Test Methods

Due to the importance of the interfacial behavior of fiber reinforced polymer composite materials, various techniques have been developed to study the interfacial properties including the pull-out [8, 9], push-out [10-12], microbond [3, 4, 13], single fiber fragmentation [14,15], and transverse debonding [16, 17] methods, as shown in Figure 2.2. The pull-out, push-out, microbond, and single fiber fragmentation methods are used to study the interfacial shear properties whereas transverse debonding method is used to study the interfacial normal behaviors. While these methods were mostly studied with quasi-static loading [3, 18-21], a few studies were performed under dynamic loading conditions.

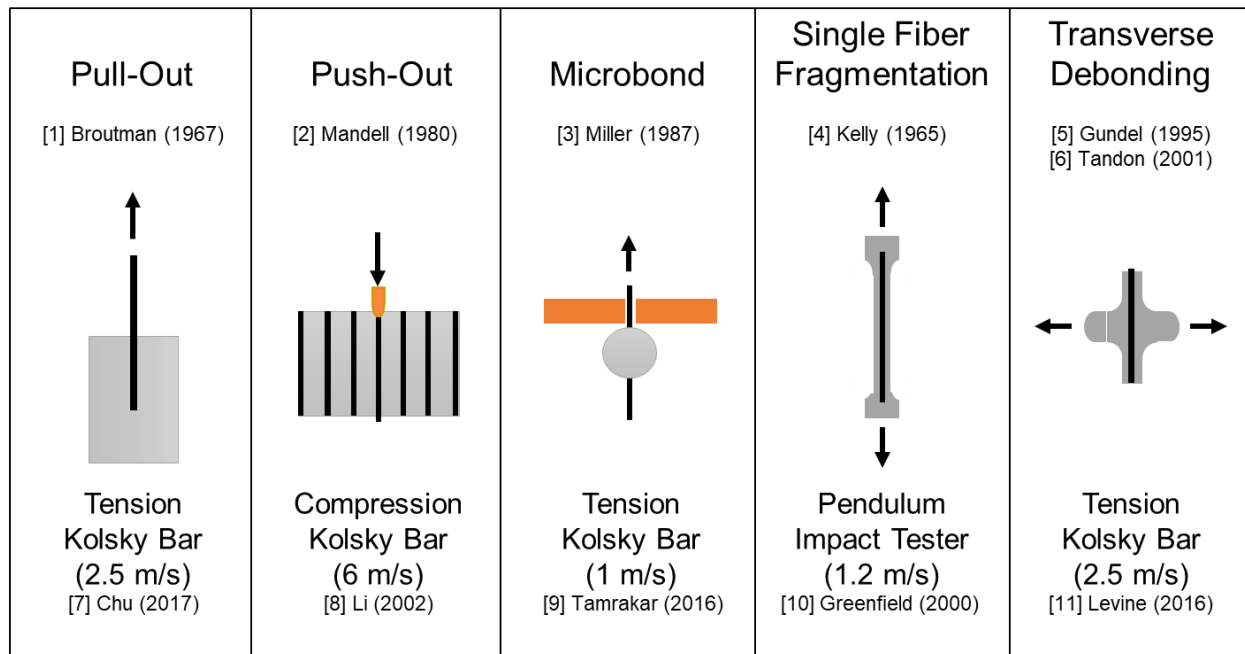


Figure 2.2. Various testing methods to study the fiber/matrix interfacial debonding behavior of a single fiber reinforced polymer specimen.

2.3 Interfacial Transverse Debonding

Even though researchers have developed various techniques to study the interfacial shear properties at both quasi-static and dynamic loading rates, it was often observed that the initial

debonding occurs in the transverse direction upon impact [22]. Thus, Gundel *et al.* developed a cross-shaped specimen with a single fiber placed in the center to study the interfacial normal stress [16]. The cross-shaped specimen allowed debonding to initiate in the center of the specimen in which the free edge effect can be avoided. The free edge effect is a stress concentration that exists at the point where the fiber meets the free surface in a fiber reinforced composite material [16, 17, 23]. Later, Tandon *et al.* improved the geometry and the design of a cross-shaped (cruciform) specimen by bonding face-sheets to the specimen to prevent premature failure in the fillet region and to encourage debond initiation at the center of the cruciform specimen [17].

Most studies on transverse debonding behavior of single fiber reinforced composites were performed under quasi-static loading. Gundel *et al.* conducted transverse loading studies at a quasi-static rate ($1.27 \mu\text{m/s}$) to study the transverse behavior of SiC/Ti-6Al-4V composites with different surface coatings, the stress distribution, and the interface failure modes [24, 25]. They found that fibers with carbon-rich coatings contained a range of interfacial strengths depending on the structure of the interface layers, whereas the interface of uncoated fibers had higher strength [24]. Of the three stresses (radial compressive stress, hoop stress, and tangential shear stresses stress), the radial compressive stress is of the most crucial to the transverse debonding between a fiber and the matrix system because the applied stresses around the interface must exceed the radial compressive stress for radial tensile stress at the interface to occur [25].

Using the Pagano-Tandon model, Gundel *et al.* derived the stress states along interface at different angles, as shown in Figure 2.3 [25]. From the modeled results, the radial stress is maximum at $\theta = 0^\circ$ and gradually decreases to a negative value (compressive) as the angle approaches $\theta = 90^\circ$. However, for the hoop (tangential normal) stress, the maximum value occurs at $\theta = 90^\circ$ [25]. For the tangential shear stress, the maximum was found at $\theta = 45^\circ$. Furthermore, Gundel *et al.* suggested three cases of interfacial failure mechanisms (Figure 2.4) [25]:

1. Radial normal stress exceeding the radial normal strength of the interface (no shear failure involved),
2. stable shear failure precedes normal failure, or
3. shear failure initiates normal failure immediately.

From the results, Gundel *et al.* found that shear failure prior to normal separation was most likely the sequence of failure [25].

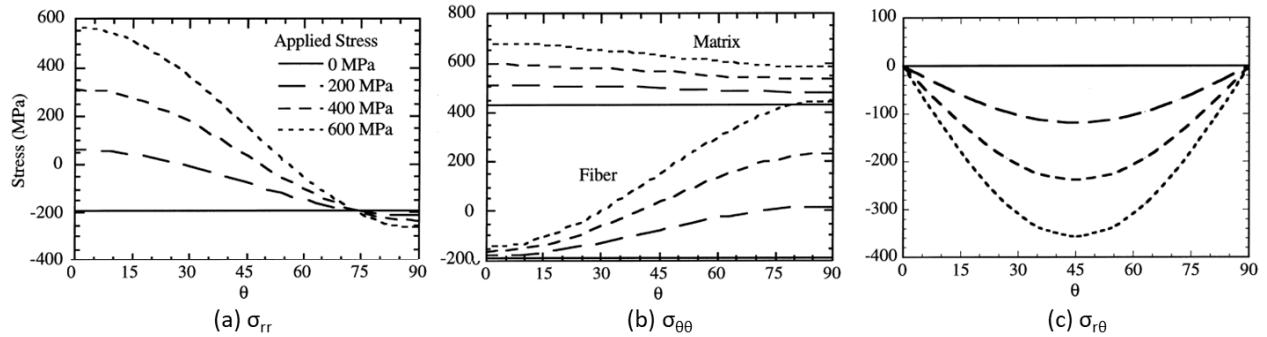


Figure 2.3. Angular stress distribution for (a) radial normal, (b) tangential normal, and (c) tangential shear stresses for a single fiber reinforced cruciform specimen loaded in transverse tension along $\theta = 0^\circ$. Reprinted from [25], Copyright (1999), with permission from Elsevier.

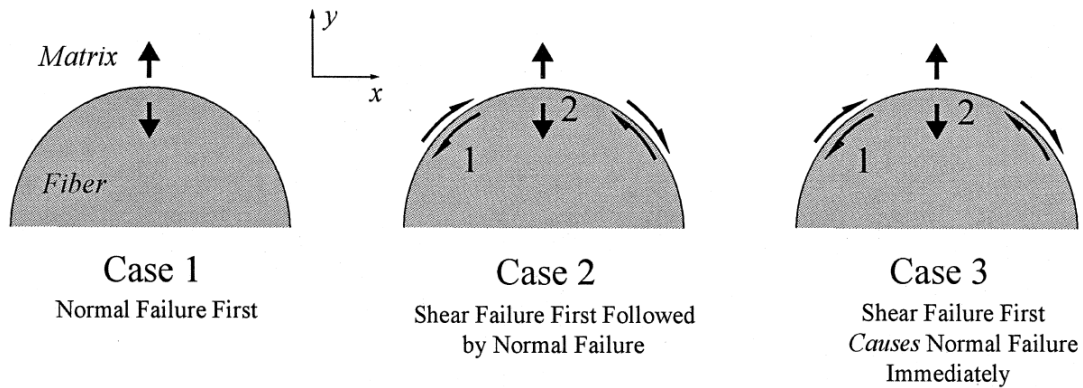


Figure 2.4. Three interfacial failure mechanisms suggested by Gundel *et al.* Reprinted from [25], Copyright (1999), with permission from Elsevier.

Tandon *et al.* [17] adapted the cruciform-shaped specimen with the reflected light technique to study the fiber/matrix interfacial debonding behavior under transverse and combined (tensile and shear) loading. For the combined loading, the cruciform specimen contains an off-axis cruciform geometry in which the wings of the cruciform specimen were inclined at an angle with

respect to the loading direction. Tandon *et al.* [17] used an uncoated SiC fiber (SCS-0 from Textron) with a diameter of $140\ \mu\text{m}$ with Epon 828 (Shell Chemical Co.) epoxy resin. Three off-axis angles (30° , 45° , 60°) were used to study the mixed loading of the interfacial debonding behavior, as shown in Figure 2.5. The radial stress concentration factor was maximum for the 90° specimen and the magnitude decreased as the off-axis angle θ decreased [17]. For the shear stress, the maximum was found to be the 45° off-axis specimens [17].

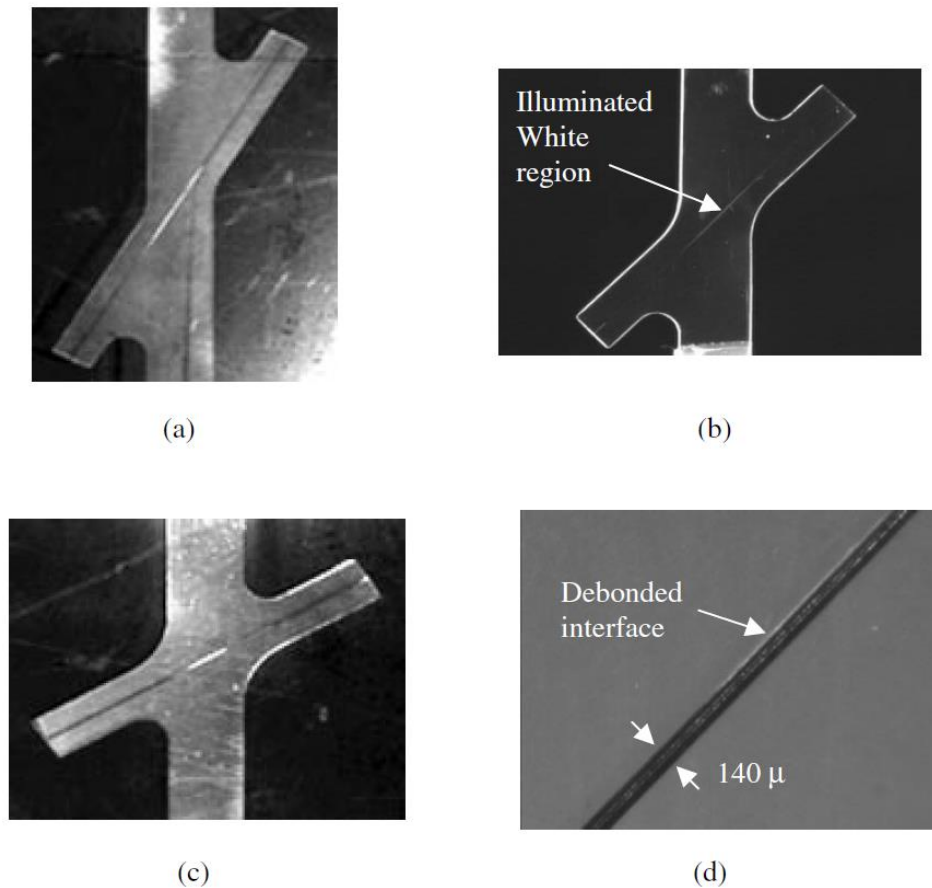


Figure 2.5. Visualization of the interfacial debonding in (a) 30° off-axis specimen, (b) 45° off-axis specimen, and (c) 60° off-axis specimen and (d) debonded area along the fiber/matrix interface. Reprinted from [17]. Copyright (2002), with permission from Sage Journals.

Foster *et al.* [26] also implemented the cruciform geometry specimen to evaluate the failure behavior of transversely loaded unidirectional model composites. Stainless-steel wires with

diameter of 0.36 mm were used with Epon 828 bisphenol A epoxy resin (Miller-Stephenson Chemical Company) with a curing agent Jeffamine D-230 polyoxypropylenediamine (Huntsville Chemical Company) [26]. The experiments were at a loading velocity of $8.5 \mu\text{m}/\text{sec}$ [26]. Multi-fiber cruciform specimens were made, as shown in Figure 2.6, to study the influence of fiber spacing on the failure initiation [26]. Three multi-fiber spacing cruciform specimens, $6d_f$, $2.5d_f$, $1.9d_f$, to represent isolated, closely packed, and densely packed fiber distribution [26]. The failure initiation of the specimen was observed via the reflected light method, as shown in Figure 2.7. From the results, it was found that debonding initiated at a point on the interface in the loading direction in either the top or bottom corner fiber for most $6d_f$ and $2.5d_f$ specimens [26]. On the other hand, damage initiated in the form of matrix cavitation instead of debonding was found for the $1.9d_f$ specimens [26]. The matrix cavitation failure initiation was characterized as non-uniform/irregular shaped spots developing in the matrix under loading due to the triaxial stress state resulting from the constraining influence of the stiff fibers [26]. For wider fiber spacings, fiber/matrix debonding occurred whereas for smaller fiber spacings, matrix cavitation occurred [26].

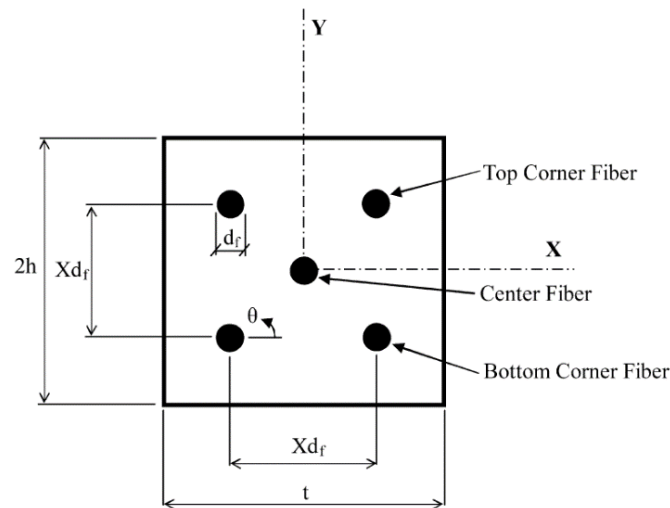


Figure 2.6. A schematic of the cross-section of the modeled multi-fiber cruciform specimen. Reprinted by permission Springer Nature, Experimental Mechanics [26], Copyright (2006).

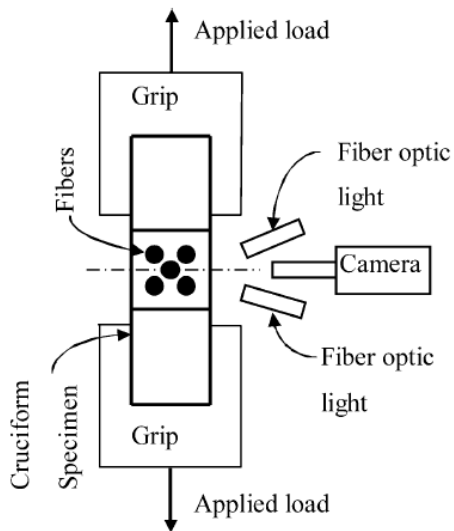


Figure 2.7. A schematic of the experimental setup for the reflective light testing technique. Reprinted by permission Springer Nature, *Experimental Mechanics* [26], Copyright (2006).

Li *et al.* [27] conducted cruciform experiments with single Borosilicate glass fiber (5 mm in diameter) embedded in EPON 828 epoxy at 0.381 mm/min with a camera to record the growth of the debonding crack, as shown in Figure 2.8 [27]. Li *et al.* [27] obtained the stress-strain curve from the DIC readings. From the images, they observed the crack opening. Li *et al.* also compared their experimental result to the FE model. From the FE model, the stress distribution was obtained around the circumference of the fiber/matrix interface [27]. Li *et al.* [27] also performed cruciform experiments at different quasi-static loading rates: 1.27 mm/min, 12.7 mm/min, and 127 mm/min to find that the rate-dependent interfacial failure behavior required the cohesive zone model to explain [27].

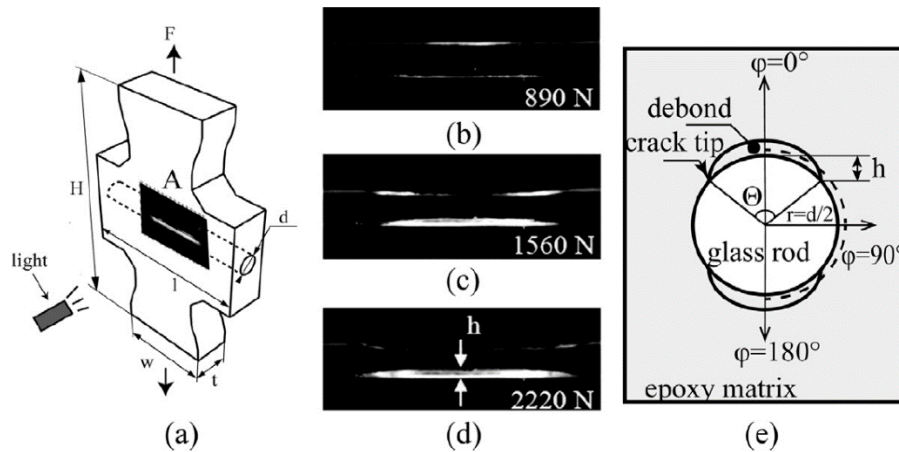


Figure 2.8. (a) A schematic of the experimental setup for the cruciform experiments. (b-d) images of the crack with height h at different forces. (e) A schematic of the cross-section across the fiber diameter showing the debonding angle evaluation scheme. Reprinted from [27], Copyright (2016), with permission from Elsevier.

For dynamic loading condition, Levine *et al.* [28] studied cruciform transverse debonding by visualizing the crack initiation and propagation using a modified tension Kolsky bar and high-speed synchrotron X-ray with a loading velocity of 2.6 m/s [28]. Levine *et al.* [28] designed a cruciform specimen with SC-15 epoxy and S-2 glass fiber that allows debonding to occur along the fiber/matrix interface with the fiber being 10 μm in diameter. SC-15 epoxy with S-2 glass fiber was used to perform the dynamic transverse debonding experiments [28]. The cruciform specimens were cured in room temperature for 48 hours. From the results, the peak debonding force was 7.67 N [28]. Levine *et al.* [28] also performed quasi-static loading experiments at 0.01 m/s to compare the results of the peak debonding force. The result obtained was 7.31 N for quasi-static loading which was only 4.6% difference between the two loading conditions [28].

More recently, Tabiai *et al* [29]. performed quasi-static transverse loading on single fiber reinforced polymer composite to study the strain field using the DIC method. Polytetrafluoroethylene (PTFE) with a diameter of 0.99 mm and galvanized steel fiber with a diameter of 0.9 mm were manufactured with Epon 862 epoxy resin with 4 parts of Epikure 3274 as curing agent to produce their specimens [29]. They found that upon debonding, crack kinking initiated in the matrix for both types of specimens [29]. However, the matrix kinking occurred at

different locations with respect to the fiber/matrix interface depending on the fiber reinforcement used. For the PTFE (lower modulus: 0.39 - 0.60 GPa) specimen, crack kinked in the 90° and -90° with respect to the loading direction (0°) [29]. On the other hand, for the steel fiber (higher modulus: 200 GPa) specimen, crack kinked in the 45° , -45° , 135° , -135° directions with respect to the loading direction [29].

2.4 Interfacial Shear Debonding

The microbond technique was first developed by Miller *et al.* to study the fiber-matrix interfacial shear properties [4]. The motivation of the microbond technique came from the difficulty of producing a small embedded length using the pull-out technique [13]. However, the results obtained from the microbond method were scattered due to the variation in the following parameters: fiber diameter, embedded length, and blade position [21, 30]. According to Zhi *et al.* [21], for smaller diameter fiber (0.012 mm), the high contact friction stress is distributed along the interface whereas the high contact friction stress points for larger diameter fibers (one order of magnitude larger) are located near the ends of the interface. Furthermore, the area ratio between high stress region and interface contact area decreases with increasing embedded length [21].

At quasi-static loading rates, Yang and his coworkers studied the interfacial strengths and failure modes of E-glass fiber-polypropylene obtained by using the pull-out and microbond techniques at $0.17 \mu\text{m/s}$ [19]. Adhesive interfacial failure (no residual resin around the debonded area of fibers) was found for the pull-out recovered specimens [19]. On the other hand, two failure modes were found for the microbond recovered specimens: adhesive interfacial failure (little to no residual resin was observed) and cohesive matrix failure (2-7 μm thickness of residual resin was observed around the debonded area of the fibers) [19].

Furthermore, Gao *et al.* conducted a systematic study on glass-epoxy interphase structure by tailoring the adhesion between constituents and the textures to control the interfacial strength and energy absorption through mechanical interlocking between the fiber material and epoxy matrix under quasi-static loading (0.003 mm/s) [3]. However, it is known that increasing the interfacial shear strength often leads to a reduction in the energy absorption [2, 31, 32]. He found that hybrid sizing with the incorporation of nanoparticles greatly improved the impact resistance (energy

absorption) without sacrificing its structural performance. The interfacial shear stress and debonding energy Gao used are calculated from equations (1) and (2) [3], where τ is the average interfacial shear stress, E_{deb} is the interfacial energy absorption until the peak debonding force, F is the peaking debonding force, d is the diameter of the fiber reinforcement, l_e is the embedded length, δ_i is the initial displacement, and δ_{deb} is the debonded displacement. The peak debonding force is defined as the maximum force recorded in the force history where the specimen can no longer take further loading.

$$\tau = \frac{F}{\pi d f l_e} \quad (1)$$

$$E_{deb} = \frac{\int_{\delta_i}^{\delta_{deb}} F d\delta}{\pi d f l_e} \quad (2)$$

At dynamic loading rates, Hudspeth *et al.* performed pull-out experiments using a modified tension Kolsky bar with high-speed synchrotron x-ray PCI at a pull-out speed of 4 m/s to observe the debonding event of Dyneema SK-62 2640 dTex fibers with an epoxy matrix [9]. Tamrakar *et al.* also used a modified tension Kolsky bar to study the rate effects of interfacial shear strength and debonding energy for S-2 glass fiber with (3-glycidoxypropyl) trimethoxy silane coupling agent and epoxy resin DER 353 mixed with bis (p-aminocyclohexyl) methane curing agent at 1 $\mu\text{m/s}$ and 1 m/s using the microbond technique [4]. The interfacial shear strength and debonding energy increased by factors of 1.7 and 2.6 respectively when the loading rate was increased by six orders of magnitude [4].

Pull-out mechanisms are important in studying the interfacial debonding behavior. According to Bannister, three types of pull-out mechanisms are observed for brittle fiber/resin system: catastrophic debonding, minor stick-slip after peak debonding force, and peaks in the ascending region [33]. Catastrophic debonding was often observed for strongly bonded interfaces or weak interfaces where the embedded length is small [33]. This means that the stored energy within the interface system is high enough the cause the fiber to debond entirely after the initiation of the interfacial failure [33]. Minor stick-slip is observed after the peak debonding force. In other words, the fiber is being extracted progressively until final failure [33]. Lastly, the peaks in the ascending region are caused by frictional damage developed along the interface. Researchers who

have conducted microbond/pullout studies have observed catastrophic debonding [3, 4, 21, 34] as well as stick-slip debonding [20, 35-38].

2.5 Crack Velocity and Wave Speeds

The crack speed and wave speeds of materials are related [39]. Ravi-Chandar studied the problems of dynamic crack propagation experimentally including crack initiation and arrest, microstructural aspects, steady-state crack propagation and crack branching, and the interaction of stress waves with propagating cracks using thin sheets of Homalite-100 [39-42]. The main difference between quasi-static fracture and dynamic fracture is the effect of inertia forces [39]. Most studies on fracture were performed under quasi-static loading. However, most fracture problems occur under dynamic loading such as ballistic impact, impact damage of fan blades, aircraft and automobile structures. Thus, Ravi-Chandar *et al.* performed experiments on Homalite-100 at a loading rate of 2.5×10^6 MPa/sec to study the dynamic crack propagation [39].

The criterion for crack to initiate is that the energy required to create new surfaces must be equal to the energy released by the solid in deforming to the new configuration [39]. However, under dynamic loading, the energy required to create a new surface may be dependent on the rate of applied loading [39]. The crack propagates at some velocity governed by the applied load and the material properties [39]. The theoretical calculations based on the elastodynamic stress field have shown that the Rayleigh wave speed sets a limit on the velocity with which the crack may propagate [43]. However, experimental studies have shown that the maximum crack velocities are much lower than that of the Rayleigh wave speed (typically around 50%) [39]. A reason of such a phenomenon was due to the idealization of the crack growth as the propagation of a crack [39].

When the stress intensity factor reaches a critical value, the crack would initiate and progress. Ravi-Chandar *et al.* found that as the rate of loading increased to 10^5 MPa/sec, the stress intensity factor required to initiate crack growth increased [39]. The crack velocity remained constant regardless of the stress intensity factor, indicating that the stress intensity effect did not occur due to rapid wave interaction [39]. As the crack continued to propagate, the concomitant unloading caused the stress intensity to decrease [39]. As the stress intensity factor decreased to a certain level such that the energy release rate was no longer sufficient to maintain stable crack propagation,

the crack arrested [39]. From the results, Ravi-Chandar *et al.* found that the “arrest stress intensity factor” was a material property because the experiments on crack arrest indicated that the instantaneous stress intensity factor at arrest seemed to have a fixed value for the tested material [39]. The crack arrested abruptly without any deceleration phase at a stress intensity below the initiation stress intensity [39].

2.6 Split-Hopkinson (Kolsky) Bars

To characterize dynamic behavior of single fiber reinforced plastic composites, a scientific loading device, the Split-Hopkinson (Kolsky) bar, was used [44]. There are different forms of Kolsky bars including, tension, compression, torsion, and compression/torsion bars [44, 45]. However, all Kolsky bars are governed by the same concept which is to use the stress waves in elastic bars to load the specimen and to measure the specimen response.

A Kolsky bar is composed of five main parts: the incident bar, the transmission bar, a striker, a flange, and a momentum trap, as shown in Figure 2.9. The striker impacts the flange which then generates a stress wave (incident strain) that travels toward the specimen section (in between the incident bar and the transmission bar). Due to impedance mismatch between the bar and the specimen, part of the wave (transmitted strain) transmits through the specimen and to the transmission bar and part of the wave (reflective strain) reflects back to the incident bar. Using the three strains measured in the bars using two pairs of strain gages (one pair on each bar), the stress-strain curve of the material can be calculated. Furthermore, because the Kolsky bar is an open-loop system, the strain rates obtained may not be constant. Thus, a pulse shaper is typically utilized to obtain constant strain rate.

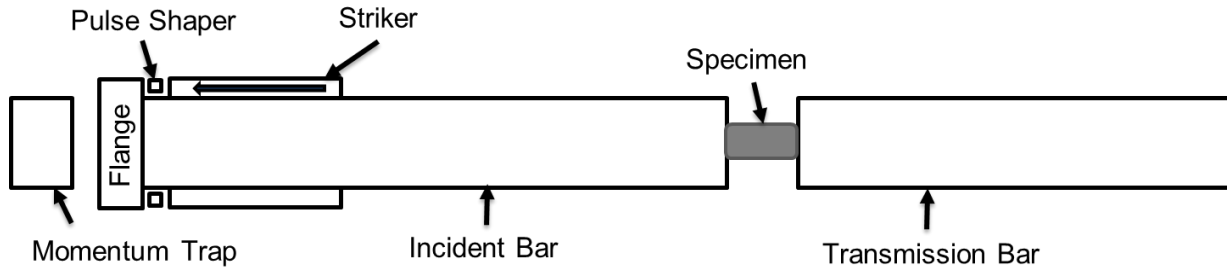


Figure 2.9. A schematic of a traditional tension Kolsky bar.

2.6.1 Modified Kolsky Bar in This Research

Since the current study used the tension Kolsky bar to load the specimens under dynamic transverse loading, emphasis is placed on discussing the tension Kolsky bar. The main difference between a traditional and the tension Kolsky bar modified in this research is that the transmission bar is replaced with a load cell, as shown in Figure 2.10. The load cell is fixed on a stage which allows direct measurement of the load history of the material. The motivation behind using a modified tension Kolsky bar is that for soft materials, the transmission bar would not be sufficient to obtain the transmitted signal [46]. In other words, for soft materials (e.g. polymers), it is difficult to measure the transmitted signal from the transmission bar due to the low amplitude of the transmitted signal. Furthermore, in the current research, another motivation to use the modified tension Kolsky bar is due to the space restriction at APS Beamline 32-ID-B, Argonne National Laboratory. The limited space in the beamline hutch requires the replacement of the transmission bar with a load cell.

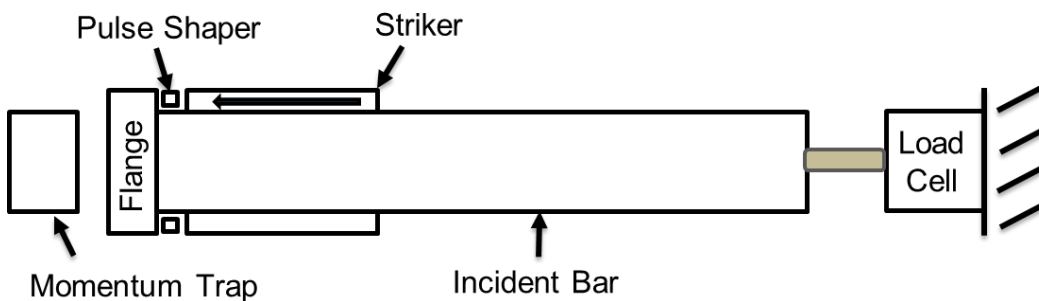


Figure 2.10. A schematic of the modified tension Kolsky bar where the transmission bar of the traditional Kolsky bar is replaced by a load cell fixed on a stage.

2.6.2 Data Reduction

The main concept behind the Kolsky bar follows the one-dimensional stress wave analysis [44]. Assuming no dispersion occurs when the stress wave propagates through the incident and transmission bars, the particle velocity at both ends of the specimen are related to the incident strain (ε_I), reflected strain (ε_R), and the transmitted strain (ε_T) via the one-dimensional stress wave theory as follows [44],

$$v_1 = c(\varepsilon_I - \varepsilon_R), \quad (3)$$

$$v_2 = c\varepsilon_T, \quad (4)$$

where c indicates the elastic bar wave speed. A schematic of the strains and particle velocities are shown in Figure 2.11. The incident, reflected, and transmitted strains came from the strains in the incident and the transmission bars. These strains are measured by using two pairs of strain gages, a pair on the incident bar and the other on the transmission bar.

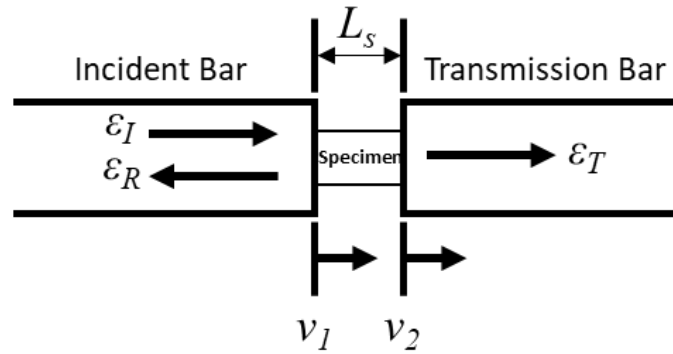


Figure 2.11. A schematic of the specimen section upon loading.

The average strain rate in the specimen is the change the particle velocity per gage length of the specimen as follows [44],

$$\frac{d\varepsilon}{dt} = \frac{d}{dx} \left(\frac{\Delta L}{L_s} \right) = \frac{\Delta V}{L_s} = \frac{v_1 - v_2}{L_s} \quad (5)$$

where L_s is the gage length of the specimen. Substituting the obtained particle velocities on both ends of the specimen to Equation 5, the strain rate of the specimen can be written as follows [44],

$$\frac{d\varepsilon}{dt} = \frac{c}{L_s} (\varepsilon_I - \varepsilon_R - \varepsilon_T). \quad (6)$$

To find the strain in the specimen, we integrate the strain rate with respect to time. For traditional Kolsky bar (with a transmission bar), the stresses at both ends of the specimen are calculated from the measured incident, reflected, and transmitted strains as follows,

$$\sigma_1 = \frac{A_b E_b}{A_s} (\varepsilon_I + \varepsilon_R), \quad (7)$$

$$\sigma_2 = \frac{A_b E_b}{A_s} \varepsilon_I, \quad (8)$$

where A_b , A_s , and E_b are the cross-sectional areas of the bar and specimen and the Young's modulus of the bar material, respectively.

For the modified Kolsky bar, since the transmission bar is replaced by a load cell, the calculation to obtain the stress-strain response of the specimen is more direct: 1. the load cell resembles a fixed end, therefore, the particle velocity is zero ($v_2 = 0$), 2. no transmission bar is used, therefore, the transmitted strain is also zero ($\varepsilon_T = 0$), and 3. the stress of the specimen can be calculated from the recorded load history divided by the cross-sectional area of the specimen.

2.7 Research Gap

Even though an extensive number of studies have been done on the interfacial properties of fiber reinforced composite materials, it is still uncertain how the crack initiates and propagates leading to the complete failure of the interface since most toughened epoxy matrices are typically opaque. Furthermore, since most fiber-matrix transverse debonding studies focused on the interfacial stress analysis with quasi-static loading, it is still uncertain how the loading velocity affects the fiber-matrix interfacial debonding behavior (e.g. debonding load, debonding crack velocity, crack geometry) specifically for fibers with diameters in the range of 10 μm . Thus, to develop a physical understanding of the dynamic debonding process, the in-situ visualization of the interfacial behavior during the debonding event is desired.

The aim of this study was to investigate the rate effect of the transverse debonding behavior of SC-15 epoxy with various reinforcements including, S-2 glass fiber, Kevlar KM2, and tungsten reinforcements by visualizing the dynamic and quasi-static debonding event in real time at 2.5 m/s and 0.25 mm/s using high-speed imaging techniques. For the dynamic loading experiments, a modified tension Kolsky bar along with a high-speed synchrotron X-ray phase contrast imaging was utilized to studying the dynamic debonding event. A laser back-light imaging method with a modified tension Kolsky bar was also utilized to capture the real-time debonding event. For quasi-static loading experiments, a quasi-static load frame with a laser back-light imaging technique was used to study the quasi-static transverse debonding event. Finally, the failure surfaces of the recovered cruciform specimens were examined via scanning electron microscopy to analyze the failure mechanisms among different single fiber reinforced polymer composites.

CHAPTER 3. EXPERIMENTAL METHODS

3.1 Dynamic Transverse Loading Experiments

The dynamic transverse loading experiments were performed at the Advanced Photon Source (APS) Beamline 32-ID-B, Argonne National Laboratory and at Purdue University. The experiments performed at APS allowed us to see through the opaque matrix and to observe the fiber/matrix debonding failure because a high-speed synchrotron X-ray phase contrast imaging (PCI) technique was utilized. However, due to the limited amount of time at APS, most the experiments were performed in Purdue using a laser back-light imaging technique to quantify the results.

3.1.1 High-Speed Synchrotron X-ray PCI

A high-speed synchrotron x-ray phase contrast imaging (PCI) technique with a modified tension Kolsky bar was used to visualize the *in-situ* dynamic debonding event. The intense high-energy x-ray (~ 25 keV pink beam), generated using an undulator (1.8-cm period), allows us to see through the opaque epoxy matrix with high spatial and temporal resolutions [47]. The experiments were performed with the standard operation mode of the APS, where 24 bunches of electrons are stored in a circular ring with a circumference of 1140 meters, as shown in Figure 3.1. A pair of slow and fast x-ray shutters was used to define a short time window to prevent damage of the experimental apparatus and specimen from the intense x-ray beam. A set of adjustable slits (1-2 mm²) were used to collimate the x-ray beam. A single crystal Lu₃Al₅O₁₂:Ce scintillator with a thickness of 100 μ m was used to convert the x-rays into visible light which was then captured using a high-speed camera (Shimadzu HPV-X2, Kyoto, Japan) via a 45-degree mirror and an objective lens (5 \times , 10 \times , and 20 \times magnifications).

The PCI method as opposed to other x-ray imaging methods was used because PCI imaging allows us to capture the crack formation in our material specimen efficiently and effectively [47 - 49]. The x-ray PCI uses the change in the phase of the x-rays and refraction of the x-rays as they pass through the specimen containing materials with different densities [48 - 50]. X-ray PCI

provides higher contrast between the different constitutive phases of the specimen in the high-speed imaging experiments.

The high-speed camera used in the current study allows us to take 256 frames per experiment. Note that the temporal resolution of the transverse debonding high-speed imaging was 5 MHz for all performed experiments (both dynamic and quasi-static). This means that for experiment, we can only capture 51.2 μs of the failure event. Thus, it is critical to set the timing right to capture the entire failure process. To set the timing properly, there are two components that are crucial: the gas gun (that fires the striker of the Kolsky bar) and the slow shutter. The slow shutter in our setup closes and opens within 60 ms. The gas gun loaded the striker around a hundred milliseconds depending on the firing pressure. Thus, prior to experiments, 10 testing shots were performed to obtain an average timing for the firing system and to utilize this timing to find the delay from firing to the slow shutter opening. The oscilloscope was triggered by the incident wave passing through the strain-gages on the incident bar. Then, the camera and fast shutters were triggered. The timing required delay generators to capture the event successfully.

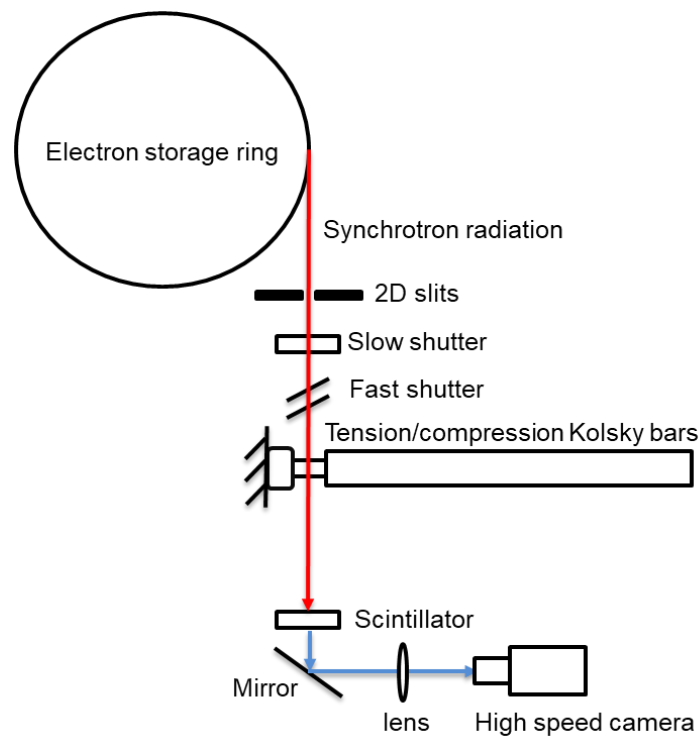


Figure 3.1. A schematic of the high-speed synchrotron X-ray with Kolsky bars setup.

3.1.2 Modified Tension Kolsky Bar (in Beam line 32-ID-B)

The modified tension Kolsky bar consisted of an incident bar (aluminum 7075-T6) with 12.7 mm in diameter and 2200 mm in length and a coaxial brass striker tube with the inner diameter of 17 mm, an outer diameter of 19 mm, and a length of 450 mm. Two layers of annular shaped masking tape (0.3 mm) were used as the pulse shaper. A 50-lbf quartz load cell (Model 9712B50, Kistler, Amherst NY, USA) was fixed on a three-dimensional adjustable stage to record the load history of the debonding event. A panoramic view and a schematic of the experimental setup are presented in Figures 3.2 and 3.3. Prior to each experiment, the wings (left and right sides) of the cruciform specimen were clamped in place by mechanical grips that were mounted onto the incident bar and the load cell. The striker was launched by a gas gun which then impacted the flange. Upon impact, a tensile stress wave was generated to travel from the flange end of the incident bar to the specimen end of the incident bar which then loaded the cruciform specimen in the transverse direction. The square shown in Figure 14 indicates the X-ray window.

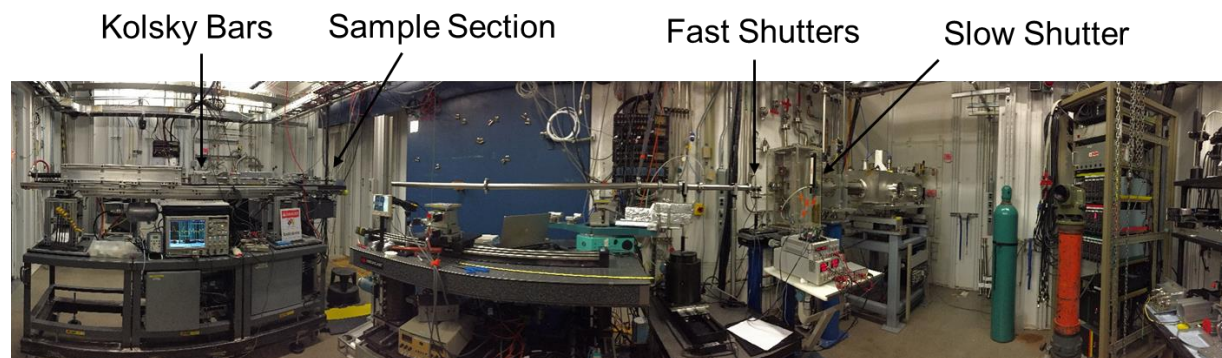


Figure 3.2. A panoramic view of the experimental apparatus in Beamline 32-ID-B hutch, APS.

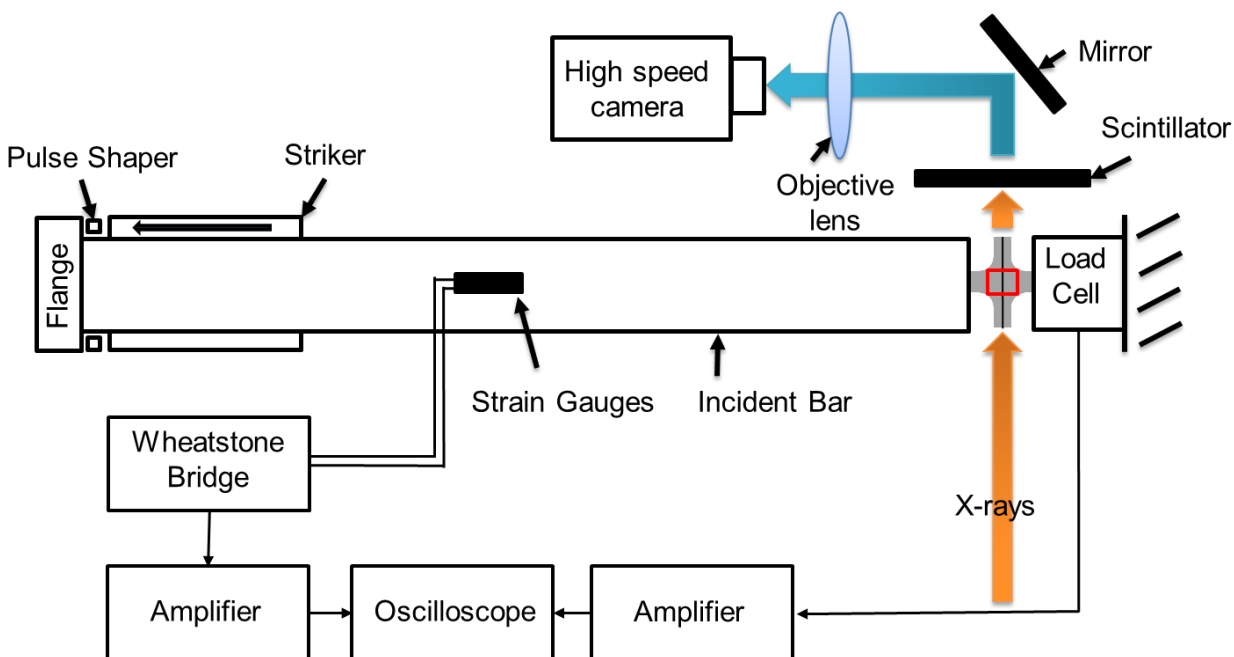


Figure 3.3. A schematic of the experimental setup (modified tension Kolsky bar) in Beamline 32-ID-B hutch, APS. Reprinted by permission from Springer Nature, Journal of Materials Science [47], Copyright (2017).

3.1.3 Modified Tension Kolsky Bar (in ARMS B130, Purdue University)

The modified tension Kolsky bar in Purdue was slightly different from the one in APS Beam line 32-ID-B in terms of the incident bar length and the striker length. The modified tension Kolsky bar consisted of the incident bar (aluminum 7075-T6) with 12.7 mm in diameter and 3600 mm in length and a coaxial brass striker tube with the inner diameter of 0.43 mm, an outer diameter of 0.48 mm, and a length of 900 mm. The modified tension Kolsky was built on an optical table so the modified tension Kolsky is often referred to as a “desktop tension Kolsky bar”. The experimental setup in Purdue is presented in Figure 3.4.

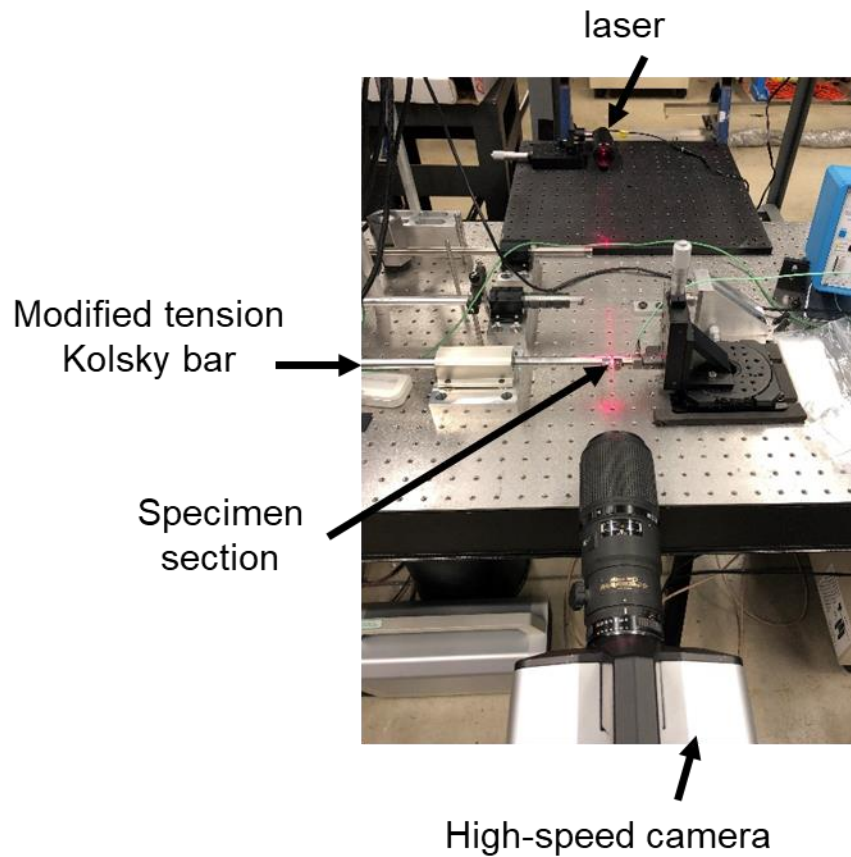


Figure 3.4. A picture of the experimental setup in Purdue.

3.2 Quasi-Static Transverse Loading Experiments

A quasi-static load frame with a high-speed camera was used to study the transverse debonding behavior at a lower velocity. A laser back-light was used as a light source to allow the crack initiation and progression to be tracked. A 50-lbf quartz load cell was fixed on a fixed circular plate to record the load history of the debonding event. Pictures and a schematic of the quasi-static transverse debonding experimental setup are shown in Figures 3.5 and 3.6. An electrical actuator was used to load the cruciform specimen in the transverse direction at 0.25 mm/s. The rectangle on the cruciform specimen indicates the camera window in Figure 3.6.

The same high-speed camera (Shimadzu HPV-X2) was used for the quasi-static loading and the dynamic loading. We used a negative trigger of the load signal to trigger the camera. In other

words, the camera was triggered when the load drops. Then, the camera saved 246 frames (post-trigger was set to 246 frames) before the time of trigger and 10 frames after. 246 frames = 49.2 μ s, meaning the first image taken was 49.2 μ s before the load dropped. The spatial and temporal resolutions for the quasi-static experimental setup were 20 μ m/pix and 5 MHz, respectively.

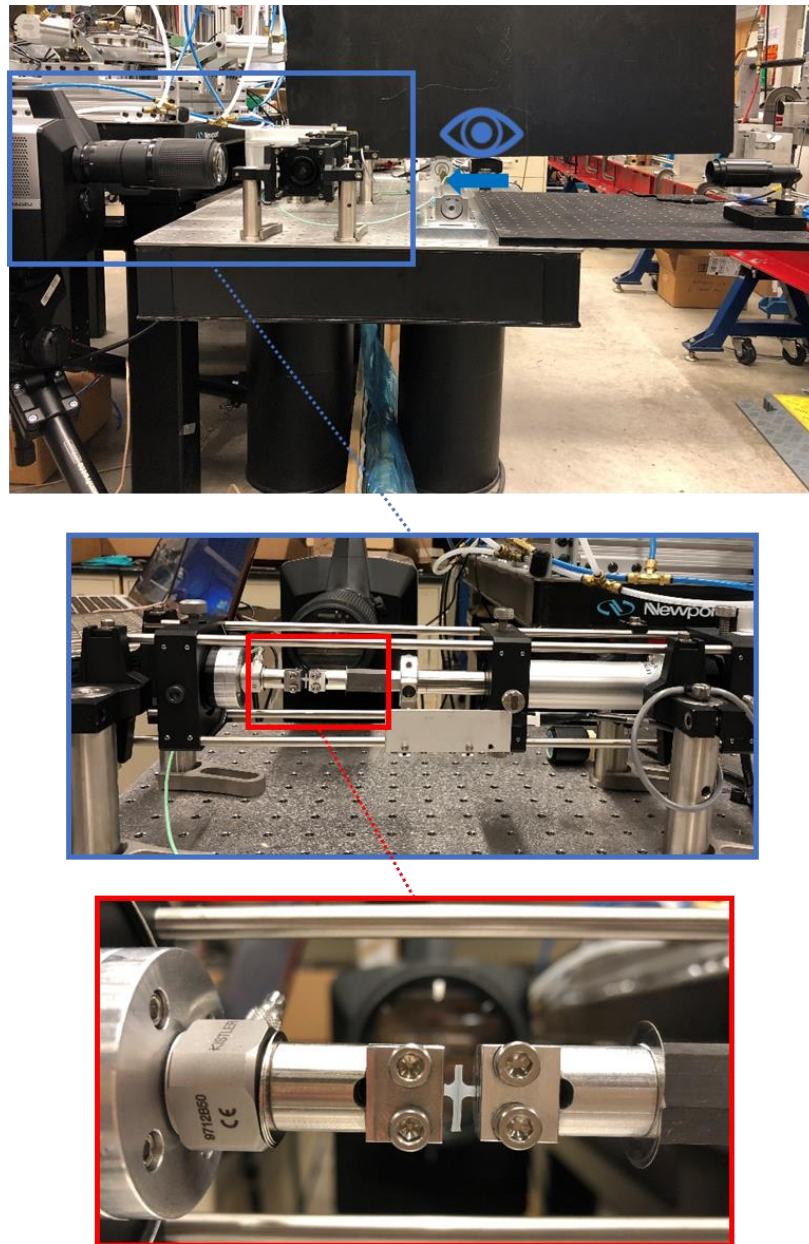


Figure 3.5. Images of the quasi-static experimental setup with the laser back-light imaging technique with a quasi-static load frame.

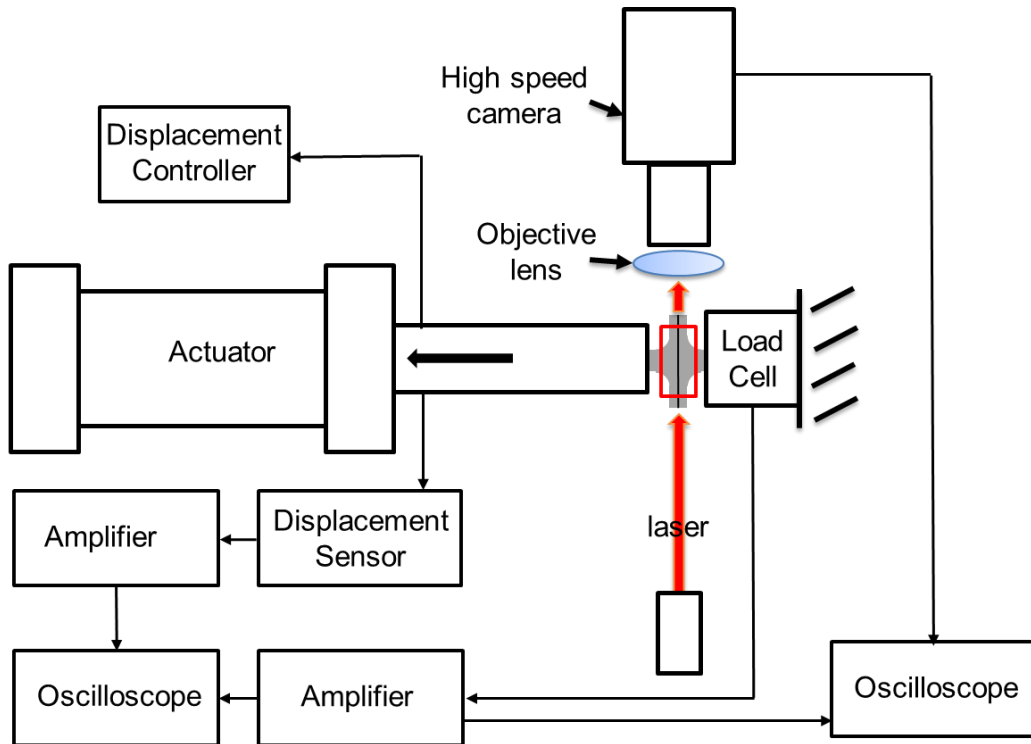


Figure 3.6. A schematic of the quasi-static experimental setup.

CHAPTER 4. MATERIALS AND SPECIMEN PREPARATION

4.1 Materials

An opaque, rubber toughened epoxy (SC-15, Applied Poleramic, Benicia, CA, USA) with S-2 glass fiber (Owens Corning, Toledo, OH, USA), Kevlar KM2 (DuPont, Wilmington, DE, USA), and tungsten (McMaster, Elmhurst, IL, USA) reinforcements were used to manufacture the cruciform specimens. Table 4.1 lists the transverse modulus, Poisson's ratio, and diameter of the reinforcements and the epoxy resin.

The SC-15 epoxy was selected for the current study because it is a high-performance epoxy for Army composite applications [51]. SC-15 is a toughened commercial vacuum-assisted resin transfer molding (VARTM) and a two-phase toughened epoxy cured with a cycloaliphatic amine [51]. The resin has good damage resistance in structural and ballistic applications [51]. The ratio of SC-15 resin and hardener is 100:30 by weight. Different curing cycles have been studied in the literary (e.g. cure for 4 hours of incremental increase from ambient temperature to 52 °C and the post-cure at 125 °C for 2 hours [52]). However, for the current study, the cruciform was cured in room temperature for 48 hours and post-cured at 125 °C for 2 hours so we can have a better comparison of the results from the study performed by Levine *et al.* [28] (48 hours in room temperature). Note that no additional sizing or surface modifiers was used on the as-received fiber surface of the studied reinforcement types.

Table 4.1. Material properties for S-2 glass, KM2, tungsten, and SC-15 epoxy

Materials	Transverse Modulus [GPa]	Poisson's Ratio	Density [kg/m ³]	Diameter [um]
S-2 Glass [53]	86	0.23	2.46	10
KM2 [54, 55]	4	0.24	1.44	12
Tungsten [56]	340-405	0.28	19.30	50
SC-15 Epoxy only	Low Rate: 1.69 High Rate: 2.15	0.35 [57]	1.09 [58]	n/a

S-2 glass fiber with SC-15 epoxy fiber reinforced composites is of interest to the Army applications [51, 52]. Of the different reinforcement types, glass fiber, namely S-2 glass fiber

(manufactured by Owens Corning but now supported by AGY), is of interest to the ballistic protection of ground vehicles. The “S” in S-2 stands for “Strength” meaning S-2 glass could be used when high tensile strength (modulus) is crucial. The as-received S-2 glass fiber with the diameter of 10 μm was treated with an amino-silane. The S-2 glass fiber consists of numerous G-filament continuous glass strands and has a linear density of 675 TEX [59].

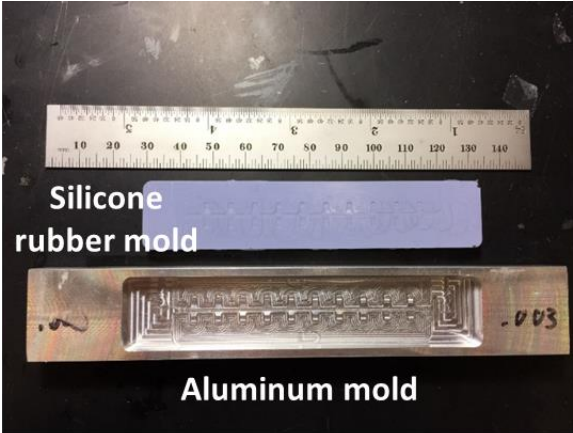
Kevlar, a para-aramid fiber, is known for its application in the body armor/protection system due to its high strength and abrasion resistance. In the current study, the Kevlar KM2 with a diameter of 12 μm was used as a reinforcement to study the interfacial debonding behavior. KM2 fiber is a transversely isotropic material that exhibits a strong anisotropy in its mechanical properties caused by the highly oriented chains of molecules [60]. The Young’s modulus in the longitudinal direction (~ 84 GPa) of the fiber is much higher than that in the transverse direction (~ 4 GPa) [54, 60]. For Kevlar, mixture or emulsion (often consists of oils) is applied to the fiber surface to reduce friction and to improve processing and/or end-use performance [61].

The last reinforcement used was tungsten wire. The motivation behind using a tungsten wire was that it is a metal reinforcement (high electron density) and it has a larger fiber diameter (50 μm). With larger diameter and higher electron density compared to the SC-15 epoxy system, we expected to see the debonding and crack progression more clearly.

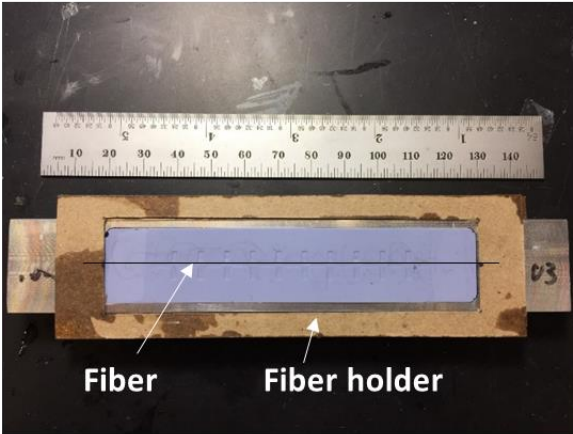
4.2 Specimen Preparation

The cruciform specimen design in the current study was adapted from Levine *et al.* [28]. To manufacture the cruciform specimens, a silicone rubber mold was made from an aluminum form by pouring a low viscosity silicone rubber (OOMOO® 30, Smooth-On, Macungie PA, USA) into the form and allowed to cure for 8 hours (Figure 4.1). Next, the silicone rubber mold was removed from the aluminum form and placed back in the form with the cruciform cavities facing up. Then, a single S-2 glass fiber was fixed on a fiber holder (made of cardboard) to position the fiber on the center of the silicone rubber mold. Once the fiber was adjusted to lay in the center of the mold strip, the fiber was taped down to the rubber mold and snipped away from the cardboard. The SC-15 epoxy was then poured in the cavity of the silicone mold which allowed 10 cruciform specimens to be produced at a time. The rubber mold with the filled cavities was placed in vacuum chamber

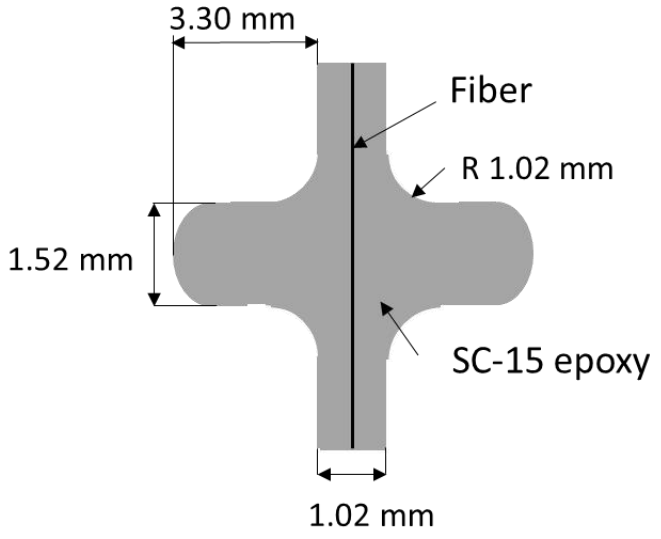
with 40 kPa for an hour to remove trapped gas. Then, the rubber mold was removed from the vacuum chamber and a flat piece of silicone rubber was placed on top of the rubber mold to ensure flatness of the cruciform surface. The flat sheet of rubber was removed after curing for 24 hours at room temperature. Another 24 hours were given for additional curing after removing the rubber sheet at room temperature. Lastly, the specimens were placed in the furnace to post-cure for 2 hours at 125 °C.



(a)



(b)



(c)

Figure 4.1. Cruciform specimen (a) and (b) preparation setup and (c) geometry.

CHAPTER 5. RESULTS AND DISCUSSION

The SC-15 epoxy with S-2 glass fiber, Kevlar® KM2, and tungsten reinforcements cruciform specimens were used to study the rate effects on the interfacial transverse debonding behavior including the peak debonding force, the debonding crack velocity, and the crack geometry at loading velocities of 0.25 mm/s and 2.5 m/s. A schematic of the transverse debonding experiment is shown in Figure 5.1. At least eight repeated experiments were performed for each loading condition. The failure surface of the recovered cruciform specimen was examined using a scanning electron microscope. The current study concentrated on two imaging views: high-speed imaging and SEM imaging (shown in Figure 5.2). The high-speed imaging focused on the center of the cruciform specimen where the debonding and crack initiated. The SEM imaging focused on the cross-section of the recovered specimen along the fiber direction.

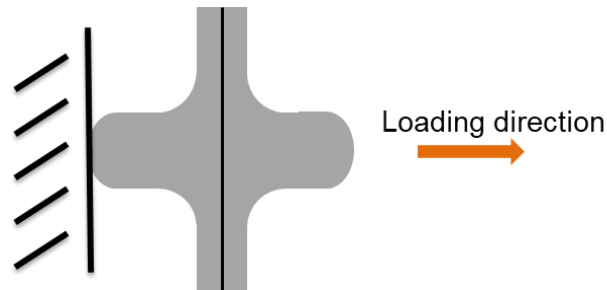


Figure 5.1. A schematic of the cruciform specimen upon loading.

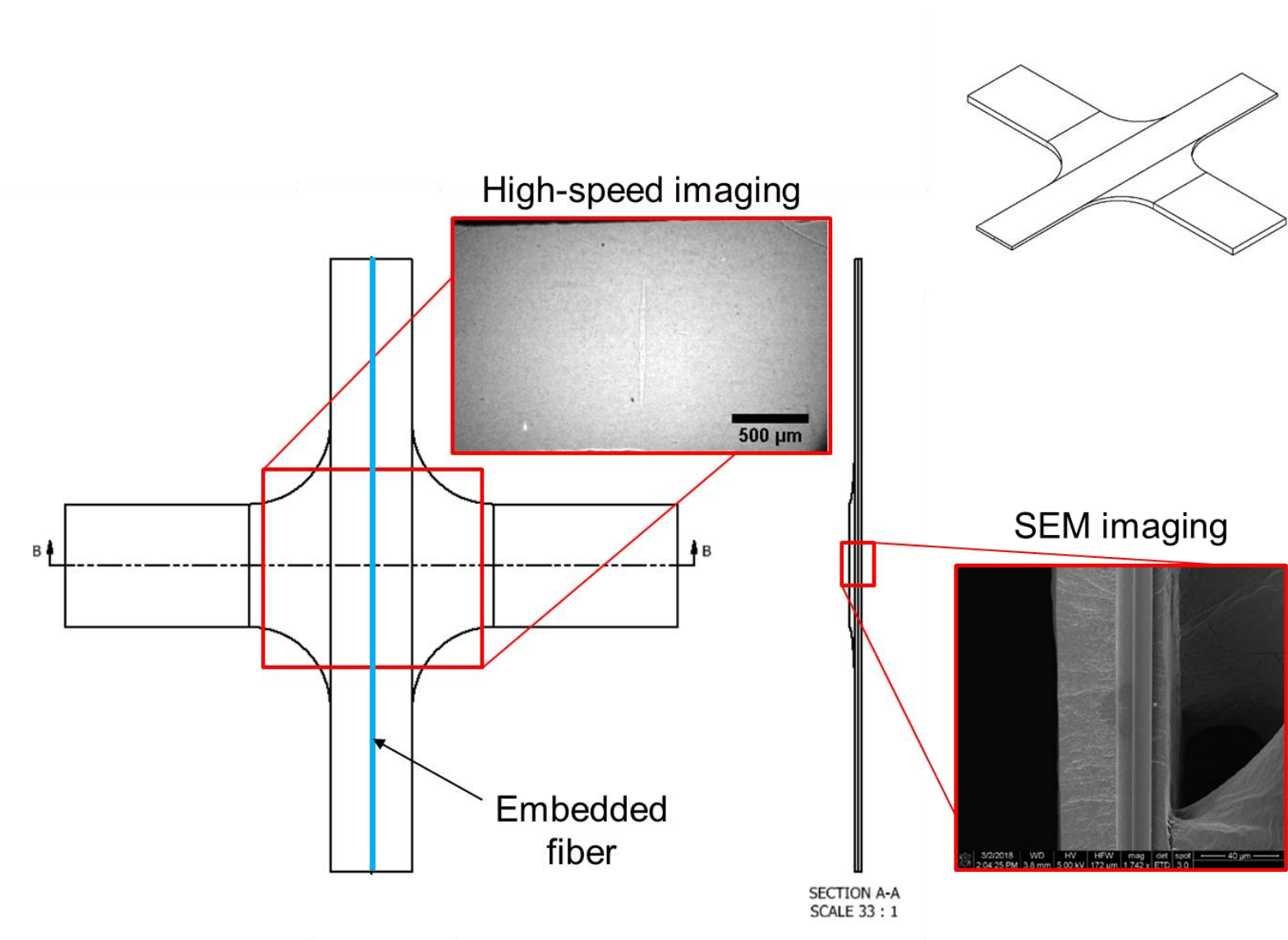


Figure 5.2. A schematic of the two imaging views: high-speed imaging and SEM imaging.

5.1 High-Speed Images with Corresponding Force History

Representative force-displacement responses and the corresponding high-speed images of S-2 glass, KM2, and tungsten reinforced cruciform specimens from debonding initiation to crack propagation until the crack propagated beyond the camera field-of-view at 2.5 m/s (the high-speed synchrotron X-ray and laser back-light imaging method) and 0.25 mm/s (the laser back-light imaging method) are discussed in this subsection. For the images taken using the high-speed synchrotron x-ray, the spatial resolutions ranged from 1.5 $\mu\text{m}/\text{pix}$ to 6 $\mu\text{m}/\text{pix}$. For the images taking using the laser back-light imaging method, the resolution ranged from 17 $\mu\text{m}/\text{pix}$ to 21 $\mu\text{m}/\text{pix}$. The time interval between each frame was 0.2 μs .

Figures 5.3 and 5.4 present the dynamic transverse loading, the force-displacement history, force-time-crack length history, and the corresponding high-speed images from experiments performed in APS Beamline 32-ID-B, Argonne National Laboratory using high-speed synchrotron X-ray PCI with a modified tension Kolsky bar. The spatial resolutions were 6.06 $\mu\text{m}/\text{s}$ and 1.5 $\mu\text{m}/\text{s}$, respectively. The corresponding high-speed images extracts 11 images, starting from the crack initiation frame ($t = t_0$) following with 10 frames ($t = t_0 + 2 \mu\text{s}$), from the stack of 256 frames. The crack continued to propagate after the 5th frame, but the limited area of the camera window prohibited us from capturing the progression after the 5th frame. The force-time-crack length plot shown in Figure 5.3 presents the progression (force and crack length with respect to time) of the 0.8 μs from where the crack initiated. In the first 0.8 μs from where the crack initiated, the load was still increasing with increasing crack length. The load continued to increase slightly after the crack initiated may be a result of the inertia effect of the specimen upon loading. Under dynamic loading, specimens would experience inertia effect upon loading, thus this phenomenon may cause time and force variance in the force response.

For Figure 5.4, a more detailed debonding event was observed since the magnification objective lens was increased from 5 \times to 20 \times . The advantage for using a 20 \times lens was that we were able to observe the details of debonding in the initiation site and the fiber was more apparent in this case. The disadvantage for using a higher magnification lens was that we could not track the crack progression because the crack tips would be out of the window frame after the 3rd frame. Furthermore, it was more likely to miss the debonding initiation with a higher magnification lens

due to the smaller window area. From the high-speed images shown in Figure 5.4, slight debonding/cracking was observed in the initial frame. The crack opened-up as time progressed. The fiber debonded on opposite sides (top debonded on the right side and bottom debonded on the left side), forming a diagonal line between the crack gap. Upon further loading, the fiber started to debond on both sides of the cruciform. In this case, another crack propagated from the upper side of the specimen. Such a phenomenon was not a common observation – debonding and matrix crack from the side. Typically, the fiber and matrix would debond or matrix failure would take place, but not both occurring in the same specimen.

The dynamic transverse loading of the S-2 glass fiber reinforced cruciform experiments performed at Purdue using the laser back-light imaging with a modified tension Kolsky bar is presented in Figure 5.5. The window frame was larger for these sets of experiments because the magnification used was lower than the ones used in APS to track the crack progression in more frames. From the force-time-crack length plot shown in Figure 5.5, the load remained near constant in the first 5 frames and started to drop after the 5th frame. At the same time, the crack continued to propagate regardless of the decrease in the load history. Such an observation was similar to that observed in the X-ray high-speed imaging (Figure 5.3) since the load had not dropped yet in the first 5 frames upon crack initiation.

Figure 5.6 presents the quasi-static transverse loading of the S-2 glass fiber reinforced cruciform experiments performed in Purdue using the laser back-light imaging with a quasi-static load frame. Due to the large time scale between the force/displacement/time history and the high-speed image recording history, the force-time-crack length plot was not constructed. Instead, a simple force-time history is presented. As precisely mentioned in the experimental method section (Ch. 3.2), the camera was triggered when the load dropped. The camera was set to save 246 frames before the time of trigger and 10 frames after. 246 frames = 49.2 μ s, meaning the first image taken was 49.2 μ s before the load drops. The crack initiation frame occurred on the 149th frame, which is 29.8 μ s after the first image was taken. Subtracting the time when crack initiated from the time the first image was taken (49.2 μ s - 29.8 μ s), the time when crack initiated prior to the load drop was calculated (19.4 μ s). In other words, the crack initiated 19.4 μ s prior to the load drop. In this case (Figure 5.6), the time of load drop was $t_f = 0.6576$ s.

The dynamic transverse loading of the KM2 fiber reinforced cruciform specimen performed using the laser back-light imaging with a modified Kolsky bar is shown in Figure 5.7. From the high-speed images, the crack propagating in the KM2 specimen appeared to be slower than that observed in the S-2 glass fiber specimen. From the force-time-crack length plot, the load remained constant for the first 6 frames and dropped afterwards. The crack continued to propagate after the drop in the load history. The quasi-static transverse loading of the KM2 specimen is shown in Figure 5.8. The crack for KM2 specimen under quasi-static loading appeared to propagate slightly slower than that of the S-2 glass specimen under the same loading conditions. Since the crack initiation frame was the 146th frame for this experiment, the crack initiated 20 μs prior to the load drop.

The dynamic and quasi-static transverse loading of tungsten reinforced cruciform specimens are presented in Figures 5.9 and 5.10, respectively. From Figure 5.9, the force-time-crack length graph revealed the load began to drop after the 4th image while the crack continued to propagate. Tungsten specimens were more difficult to track the crack length and crack width because the tungsten wire would block the crack tip and the crack gap. For quasi-static loading (Figure 5.10), the crack initiation frame was the 136th frame meaning the crack initiated 27.2 μs prior to the load drop.

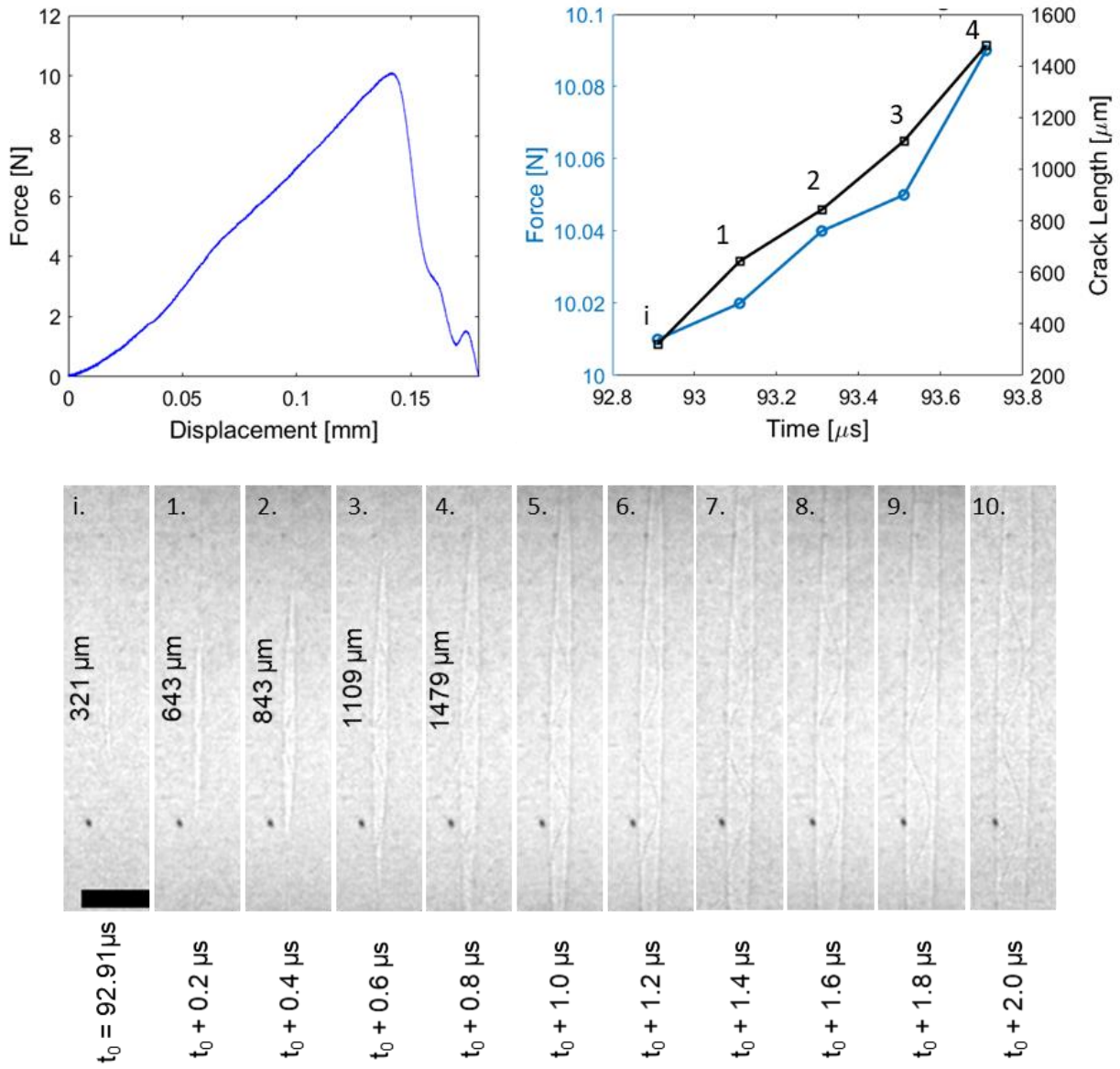


Figure 5.3. Force-displacement history and force-time-crack length history with the corresponding high-speed images sequence of S-2 glass fiber reinforced cruciform specimen at 2.5 m/s. The scale bar on the initial frame indicates 250 μm .

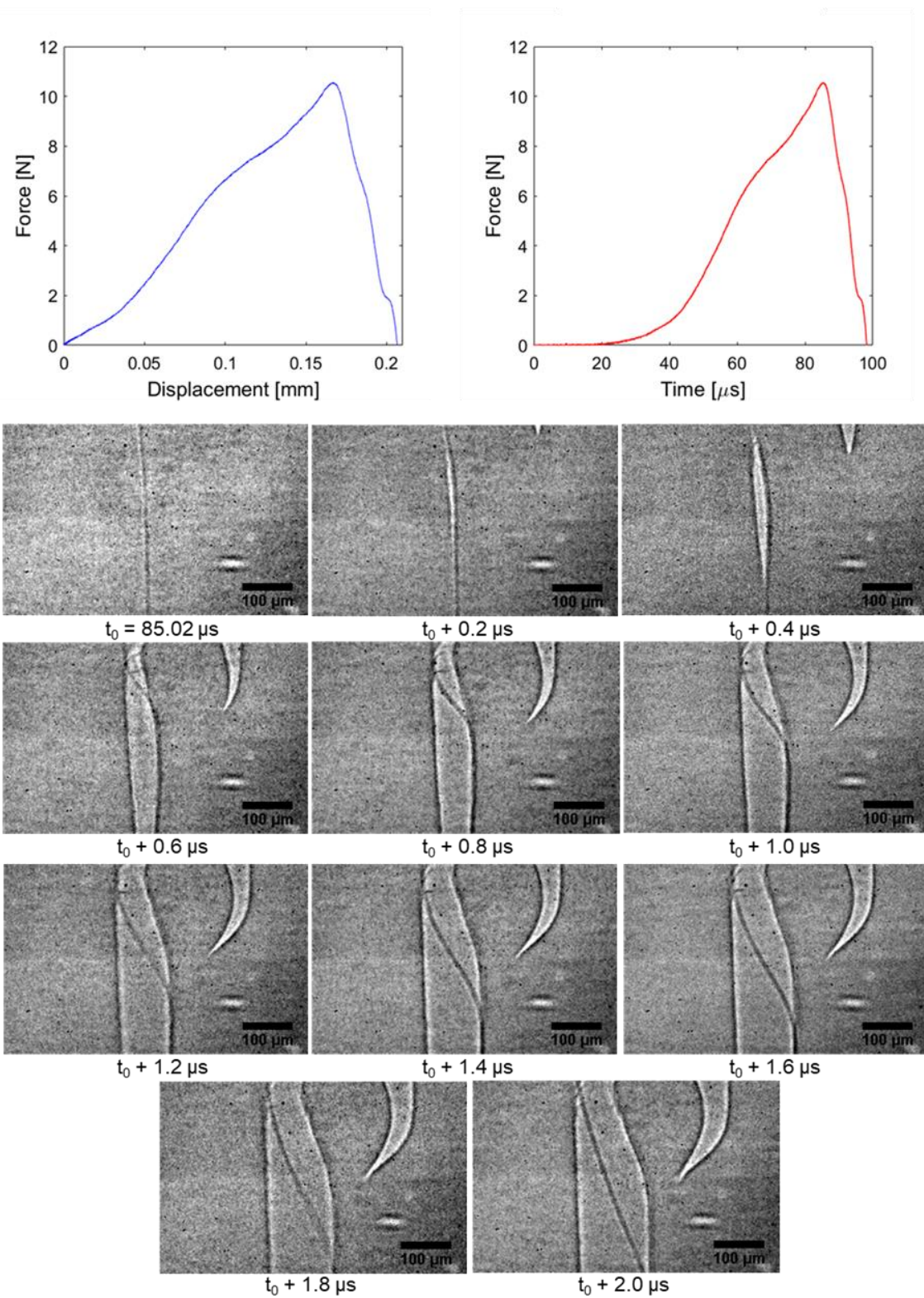


Figure 5.4. Force-displacement history and force-time-crack length history with the corresponding high-speed images sequence of S-2 glass fiber reinforced cruciform specimen at 2.5 m/s.

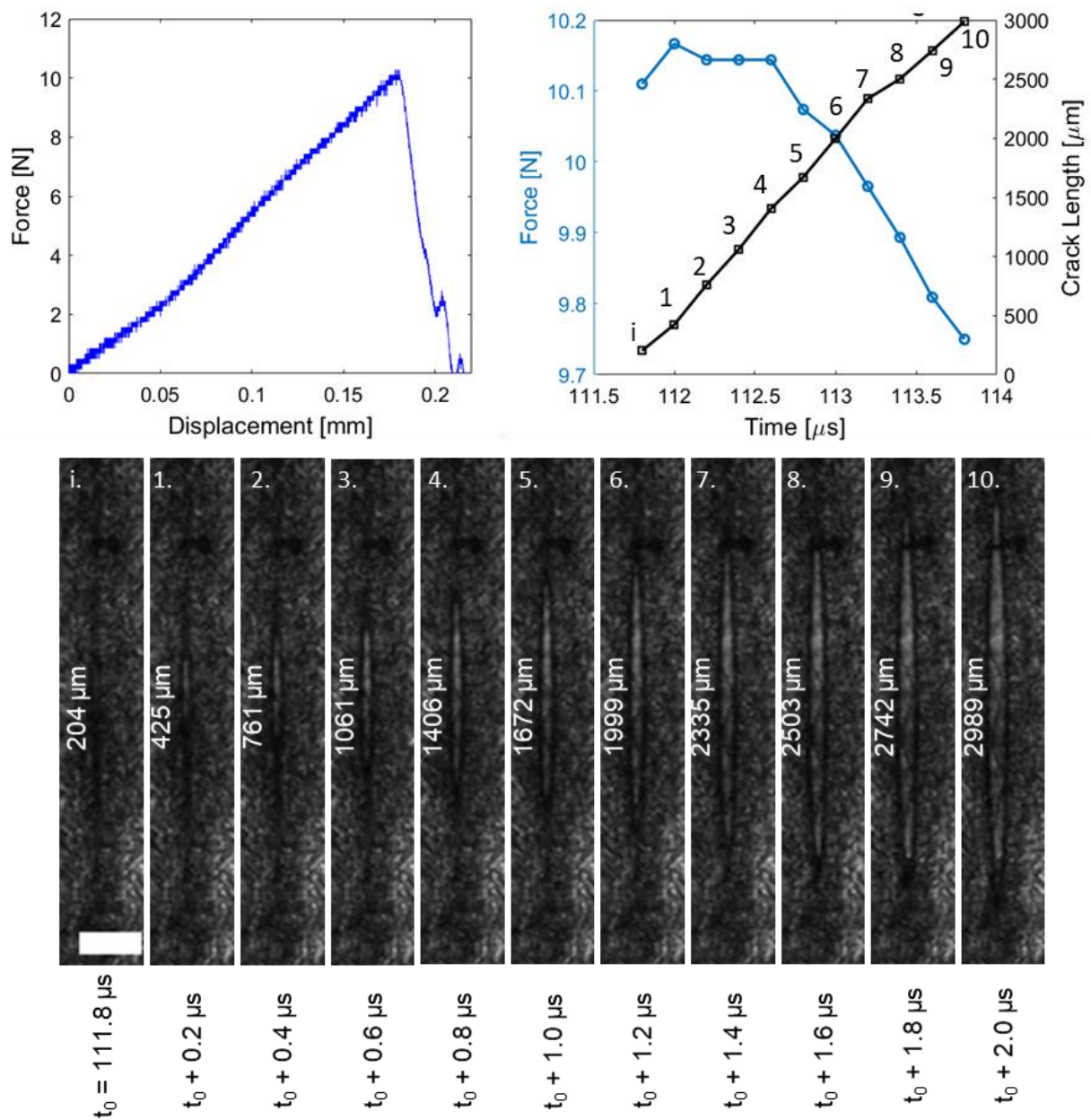


Figure 5.5. Force-displacement history and force-time-crack length history with the corresponding high-speed images sequence of S-2 glass fiber reinforced cruciform specimen at 2.5 m/s. The scale bar on the initial frame indicates 0.5 mm.

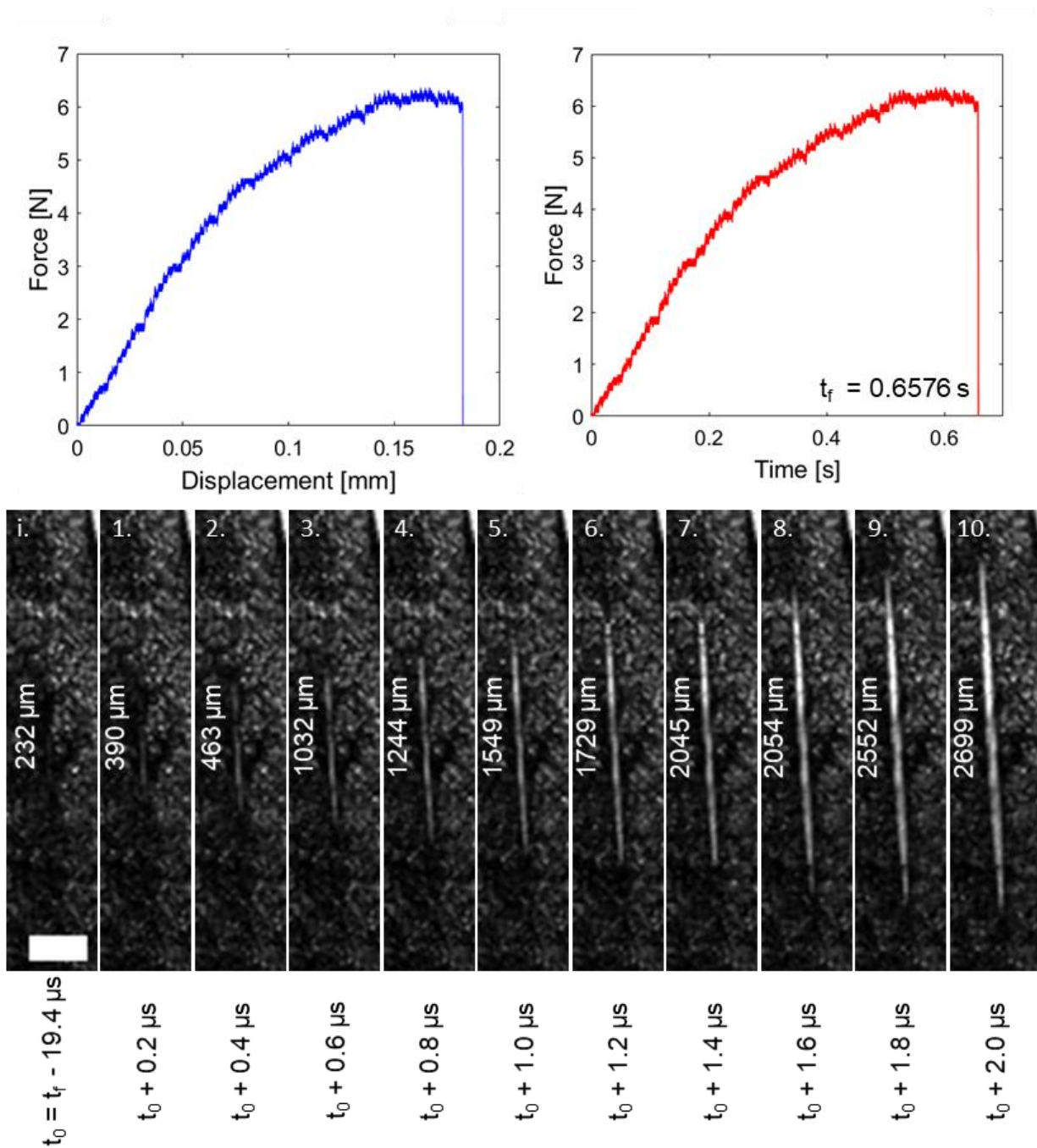


Figure 5.6. Force-displacement and force-time histories with the corresponding high-speed images sequence of S-2 glass fiber reinforced cruciform specimen at 0.25 mm/s. The scale bar on the initial frame indicates 0.5 mm.

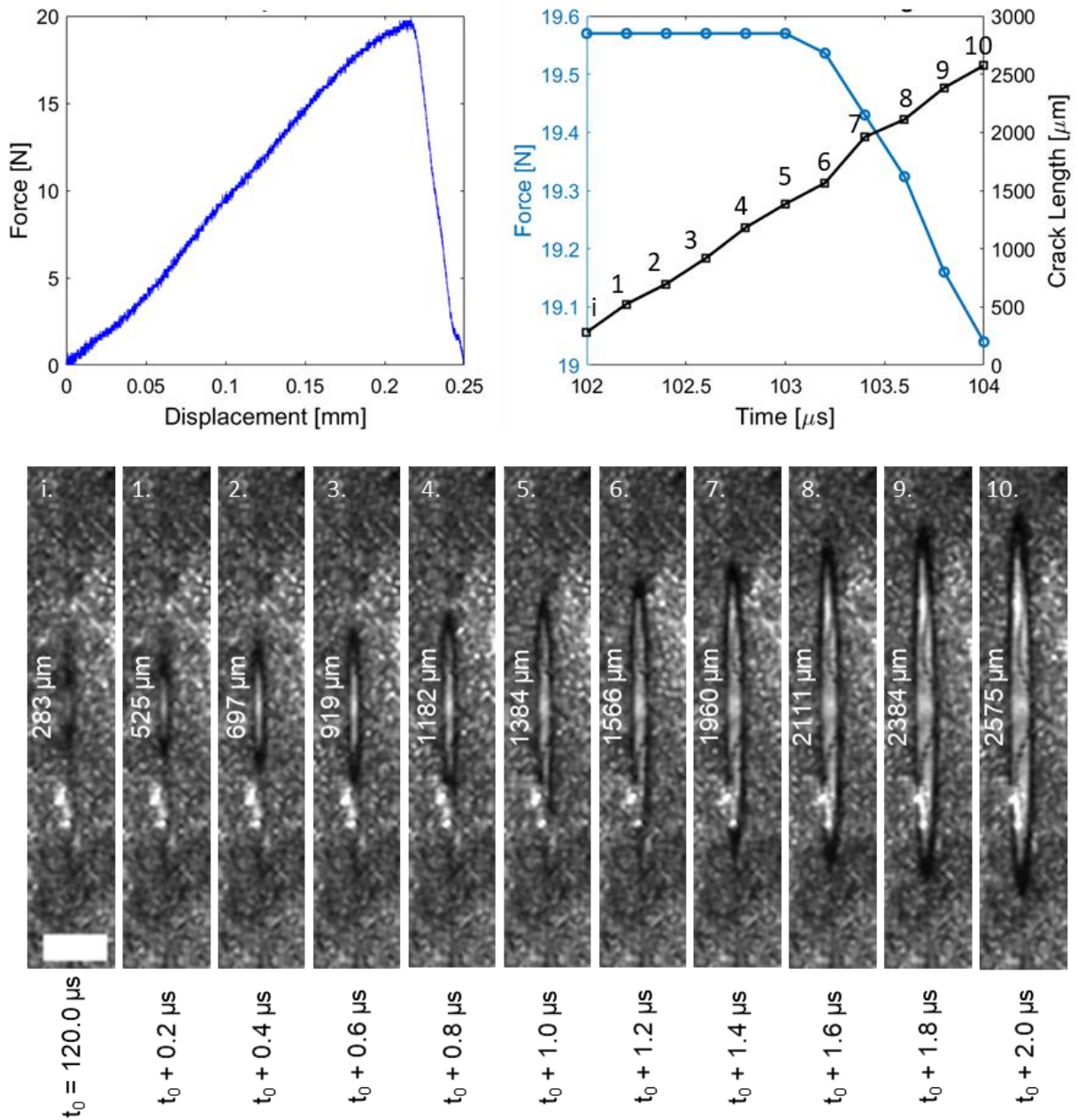


Figure 5.7. Force-displacement history and force-time-crack length history with the corresponding high-speed images sequence of KM2 fiber reinforced cruciform specimen at 2.5 m/s. The scale bar on the initial frame indicates 0.5 mm.

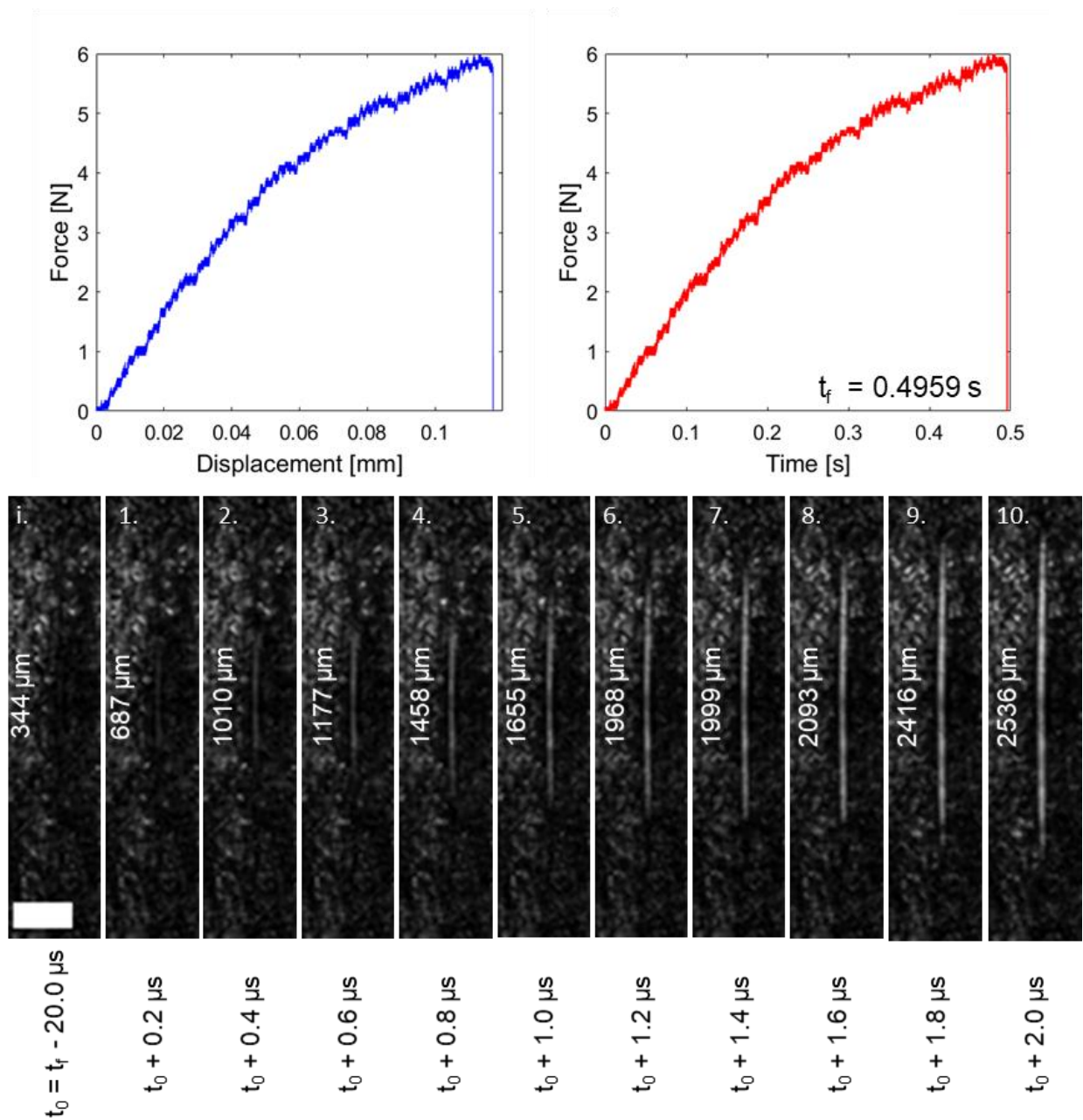


Figure 5.8. Force-displacement and force-time histories with the corresponding high-speed images sequence of KM2 fiber reinforced cruciform specimen at 0.25 mm/s. The scale bar on the initial frame indicates 0.5 mm.

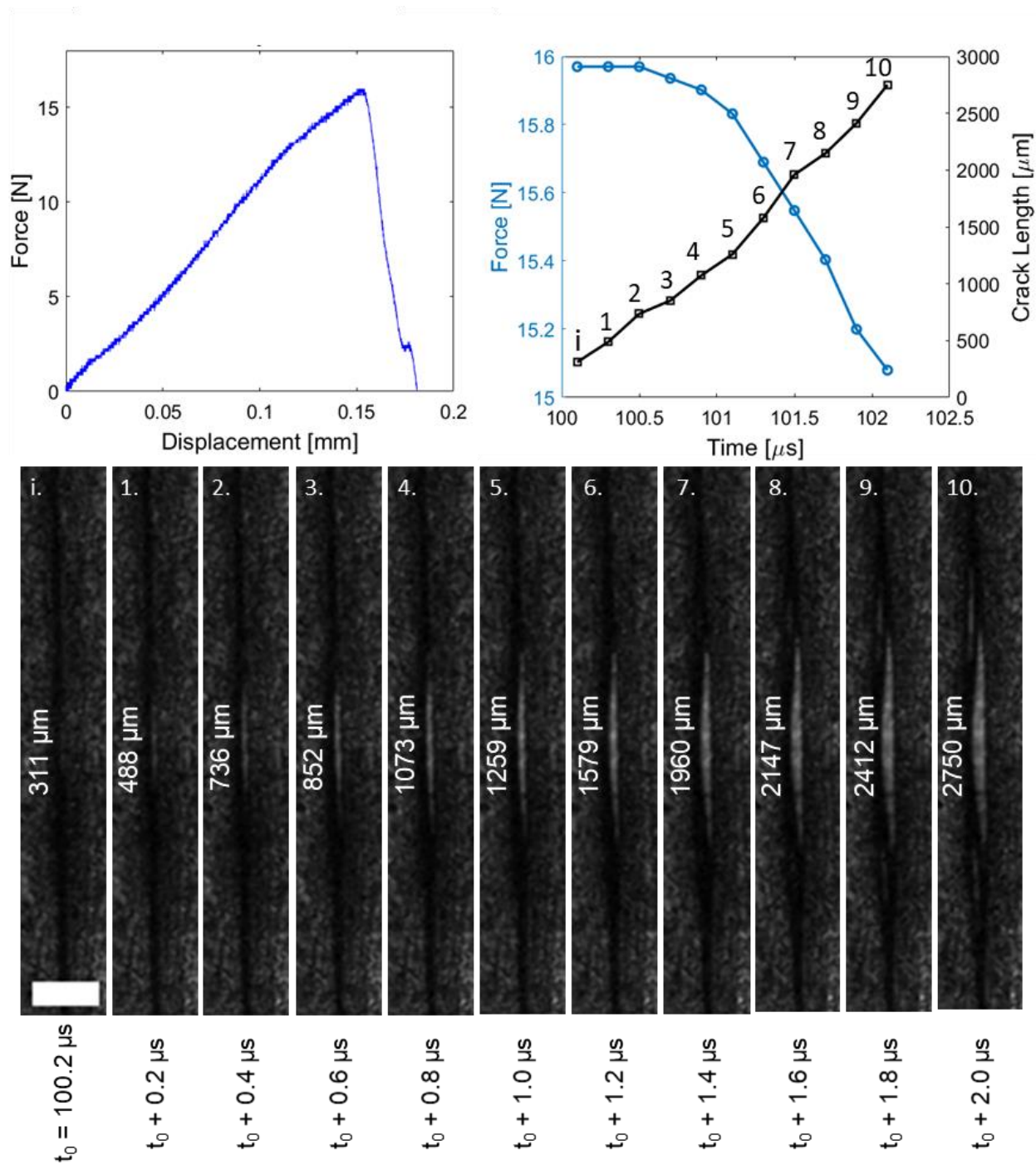


Figure 5.9. Force-displacement history and force-time-crack length history with the corresponding high-speed images sequence of tungsten reinforced cruciform specimen at 2.5 m/s. The scale bar on the initial frame indicates 0.5 mm.

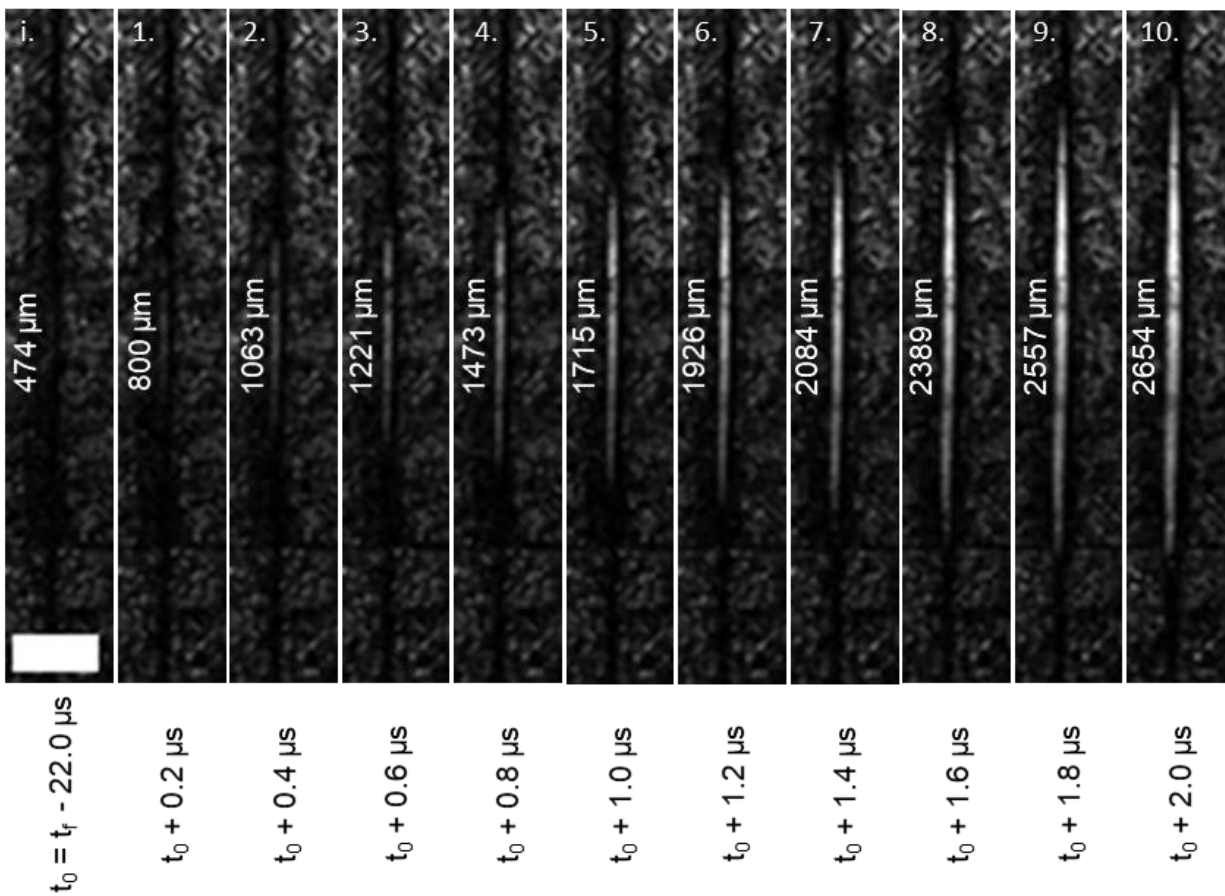
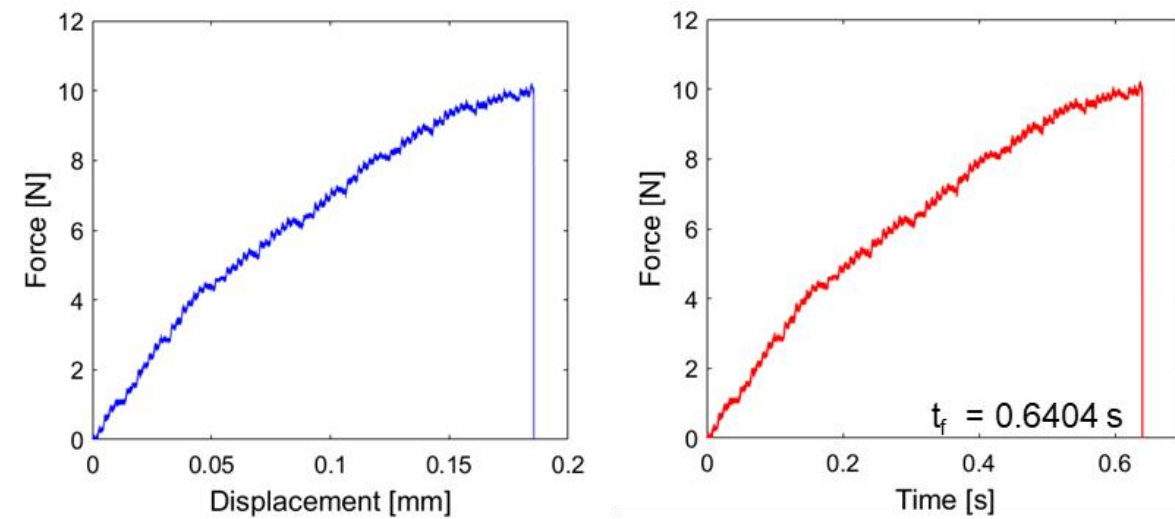


Figure 5.10. Force-displacement and force-time histories with the corresponding high-speed images sequence of tungsten reinforced cruciform specimen at 0.25 mm/s. The scale bar on the initial frame indicates 0.5 mm.

5.2 Average Peak Debonding Force

The peak debonding force was recorded for the transverse debonding experiments at 0.25 mm/s and 2.5 m/s. The peak debonding force is the maximum force measured in the load history prior to load drop. From the result shown in Figure 5.11, the average peak debonding forces of S-2 glass fiber with SC-15 epoxy at 0.25 mm/s and 2.5 m/s were 7.11 ± 0.83 N and 12.89 ± 2.51 N, respectively. The average peak debonding forces for KM2 reinforced specimens at 0.25 mm/s and 2.5 m/s were 7.06 ± 1.10 N and 15.46 ± 3.05 N, respectively. The average peak debonding forces for tungsten reinforced specimens at 0.25 mm/s and 2.5 m/s were 10.13 ± 1.69 N and 15.64 ± 0.85 N, respectively. A summary of the result is presented in Table 5.1. A reason that caused the scatter in the average peak debonding forces was from the specimen preparation. The thickness of the specimens was not uniform for all specimens. Furthermore, the fiber may be not be in the exact center of the cruciform specimen when the fiber was placed on the silicone rubber mold for specimen preparation.

All three reinforcement types revealed higher average peak debonding force at 2.5 m/s as opposed to 0.25 mm/s. A reason for such an increase in the average peak debonding force includes rate sensitivity of the SC-15 epoxy. To verify the rate sensitivity of the epoxy matrix system, five repeated experiments were performed on the SC-15 epoxy without a fiber in it at both 0.25 mm/s and 2.5 m/s. The average peak forces for the SC-15 epoxy at 0.25 mm/s and 2.5 m/s were 10.13 ± 1.69 and 15.64 ± 0.85 N, respectively.

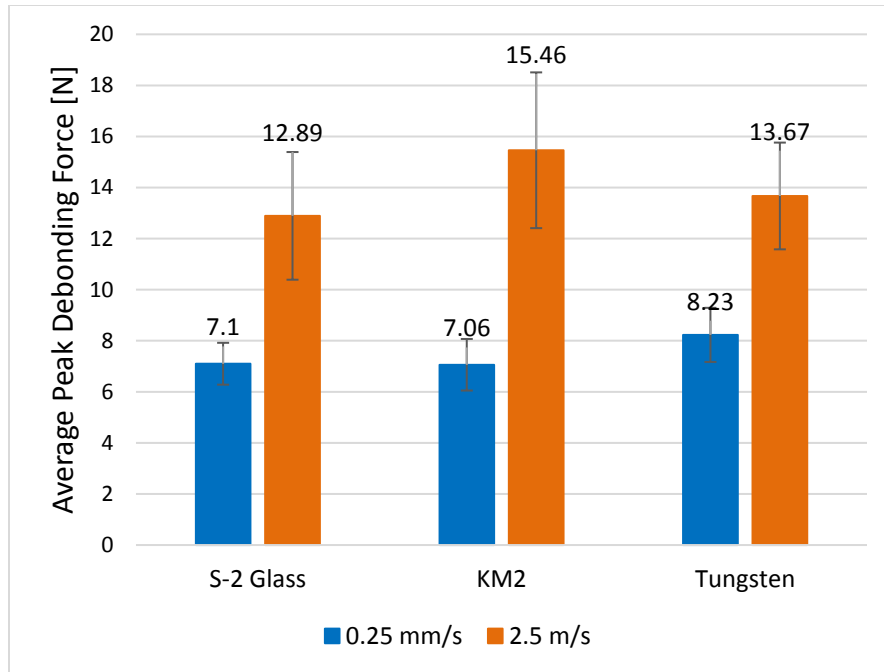


Figure 5.11. Average peak debonding force for S-2 glass, KM2, and tungsten fiber reinforced cruciform specimens at 0.25 mm/s and 2.5 m/s.

Table 5.1. Results obtained for the various fiber reinforced specimens at 0.25 mm/s and 2.5 m/s

Fiber Type	Thickness [um]	Average Peak Force [N] at 0.25 mm/s	Average Peak Force [N] at 2.5 m/s	Diameter to Thickness ratio	Average crack velocity [m/s] at 0.25 mm/s	Average crack velocity [m/s] at 2.5 m/s
S-2 Glass	63.4	7.11 ± 0.83	12.89 ± 2.51	0.16	587.43 ± 23.40	683.57 ± 18.34
KM2	69.9	7.06 ± 1.10	15.46 ± 3.05	0.17	534.09 ± 23.02	593.94 ± 29.48
Tungsten	101.7	8.23 ± 1.06	13.67 ± 2.09	0.49	598.93 ± 69.67	646.25 ± 50.56

For quasi-static loading, the average peak debonding force for all three reinforcements revealed similar results with tungsten being slightly higher. Such a slight increase of the average peak debonding force for tungsten may result from the increase in the thickness of the specimen or the increase in the fiber diameter to specimen thickness ratio. For tungsten, the average thickness of the specimen was $101.7 \pm 6.6 \mu\text{m}$. For S-2 glass and KM2 reinforced cruciform specimens, the average thicknesses were $63.4 \pm 5.5 \mu\text{m}$ and $69.9 \pm 10.2 \mu\text{m}$. The ratio of the fiber diameter to the sample thickness for S-2 glass, KM2, and tungsten were calculated to be 0.16, 0.17, and 0.49, respectively.

The displacement for KM2 and S-2 glass reinforced cruciform specimens were higher than that of the tungsten reinforced cruciform specimens, specifically for dynamic loading conditions (Figures 30-32). The lower displacement for the tungsten reinforced cruciform specimen may be caused by the high ratio of fiber diameter to the specimen thickness (0.49). In other words, smaller cross-section of the matrix along the failure surface caused tungsten reinforced specimens to have lower displacement. From the results, the cohesive bond for the matrix appeared to result in a higher displacement (or strain) whereas the adhesive bond between the matrix and fiber appeared to result in a lower displacement (or strain).

The dynamic and quasi-static loading history for each types of cruciform specimens revealed different slopes (Figures 5.12 - 5.14). The dynamic loading history revealed a more brittle failure manner whereas the quasi-static loading history revealed a less brittle failure behavior since the load did not drop directly back to zero after reaching the peak debonding force. A cause of such a phenomenon may be the rate sensitivity of the matrix failure mechanisms.

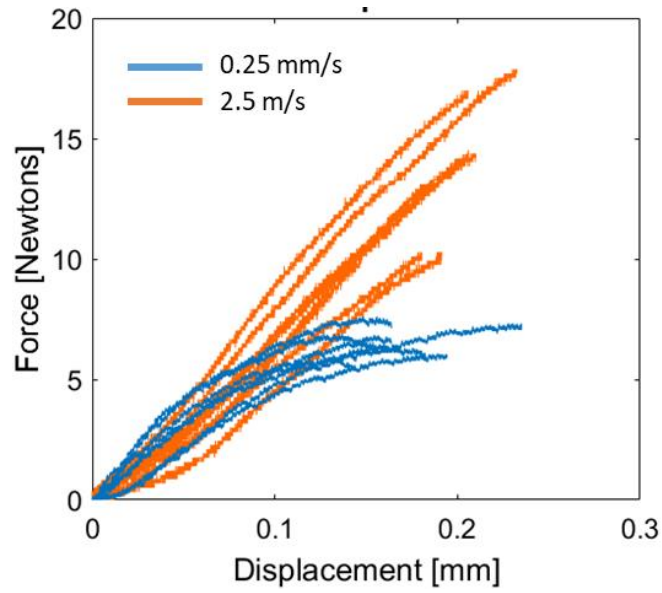


Figure 5.12. Force-displacement responses of S-2 glass fiber reinforced cruciform specimen at 0.25 mm/s and 2.5 m/s.

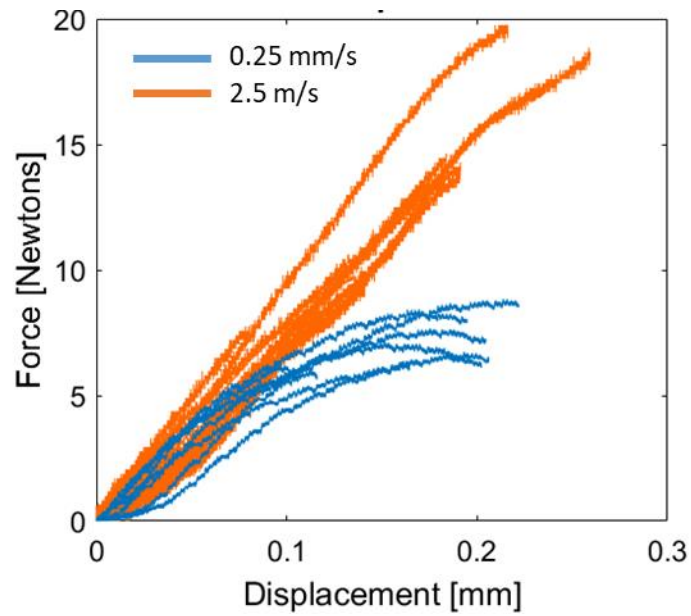


Figure 5.13. Force-displacement responses of KM2 fiber reinforced cruciform specimen at 0.25 mm/s and 2.5 m/s.

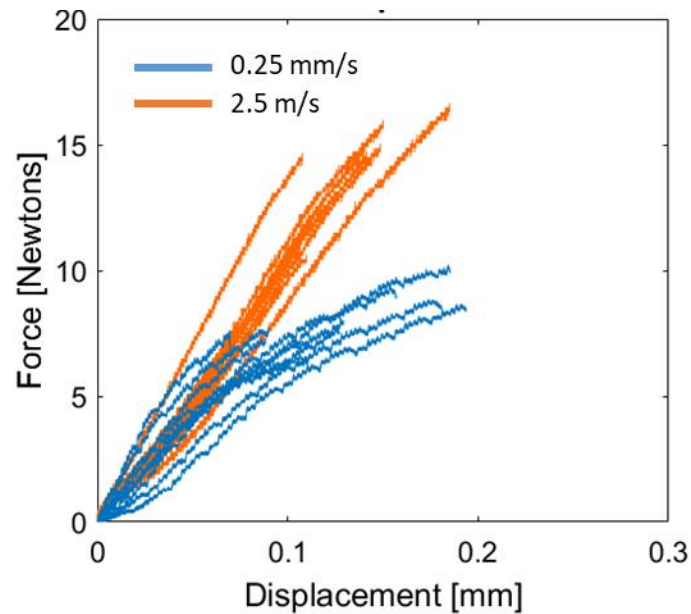


Figure 5.14. Force-displacement responses of tungsten fiber reinforced cruciform specimen at 0.25 mm/s and 2.5 m/s.

To rigorously analyze the rate dependence and the reinforcement dependence of the peak debonding force, statistical hypothesis tests (t-tests) were performed. The Anderson-Darling normality test was performed prior the t-test to investigate the normality of the experimental results. At the level of 0.05, all the results were significantly drawn from a normally distributed population (Table 5.2). Thus, we proceeded to the t-tests to investigate the statistical difference between different reinforcements and between the same reinforcements but at different rates. Examining the three reinforcements (S-2 glass, KM2, and tungsten) at 0.25 mm/s (at the level of 0.05), there is statistical difference between tungsten reinforced specimens and the two other fiber reinforced specimens (S-2 glass and KM2), as shown in Table 5.3. There is no significant difference between KM2 and S-2 glass fiber reinforced specimens. At 2.5 m/s, there is no significant difference among the three reinforced specimens. Comparing the rate dependence, there is significant difference for all three types of reinforcements between quasi-static and dynamic loading conditions, as shown in Table 5.4.

Table 5.2. Anderson-Darling normality tests for peak debonding forces

	S-2 Glass	KM2	Tungsten
0.25 mm/s	0.61	0.06	0.68
2.5 m/s	0.14	0.58	0.21

Table 5.3. t-tests for peak debonding forces comparing different reinforced specimens

	S2 vs KM2	S2 vs Tungsten	KM2 vs Tungsten
0.25 mm/s	0.73	0.003	0.01
2.5 m/s	0.99	0.75	0.99

Table 5.4. t-tests for peak debonding forces comparing rate difference (0.25 mm/s and 2.5 m/s)

S-2 Glass	KM2	Tungsten
0.00	0.00	0.00

5.3 Average Interfacial Crack Velocity

The average interfacial crack velocities were measured for both loading velocities of 0.25 mm/s and 2.5 m/s. The average interfacial debonding crack velocity was calculated by taking the full crack length divided by the time difference between the initial crack image and the eleventh image. The calculated value was then divided by 2 since crack propagated in both directions (top and bottom). The reason this method was used to calculate the average crack velocity instead of tracking the cracking tip on either side of the crack was that the average interfacial crack velocity was different between the top and bottom crack tips of a cruciform specimen. This behavior was due to the minor misalignment when placing the specimen in the grips. The difference between the top and the bottom tip velocities for dynamic experiments various from 3 m/s to 200 m/s with an average of 115 ± 78 m/s. Such a difference in the top and bottom crack tip velocities was ~20% of the average crack velocity calculated meaning that the tip velocities were sensitive to the local stress-strain state.

For S-2 glass fiber reinforced cruciform specimens, the average crack velocities at 0.25 mm/s and 2.5 m/s were 587.43 ± 23.40 m/s and 683.57 ± 18.34 m/s, respectively. For KM2 fiber reinforced cruciform specimens, the average crack velocity at 0.25 mm/s and 2.5 m/s were 534.09 ± 23.02 m/s and 593.94 ± 29.48 m/s, respectively. The average crack velocity for tungsten reinforced cruciform was 598.93 ± 69.67 m/s and 646.25 ± 50.56 m/s, respectively. The larger scatter in the tungsten average crack velocity resulted from the difficulty to pin-point where and when the crack initiated leading to the material failure because the tungsten wire would be blocking the crack tips.

A summary of the crack velocities for S-2 glass fiber, KM2 fiber, and tungsten reinforced cruciform specimens is presented in Figure 5.15. The average crack velocities for the three fiber materials increased with increasing loading velocities. Comparing S-2 glass fiber with KM2 fiber reinforced specimens, the average crack velocities for both loading conditions were higher for the S-2 glass fiber reinforced specimens than that of the corresponding loading velocities for KM2 fiber reinforced specimens. The reason for such a decrease in the average crack velocity for KM2 specimens is discussed in the post-mortem analysis section since it may be caused by the difference in the failure mechanism between S-2 glass fiber and KM2 fiber reinforced cruciform specimens. The crack velocity for all three materials did not reveal a major difference with the same loading conditions.

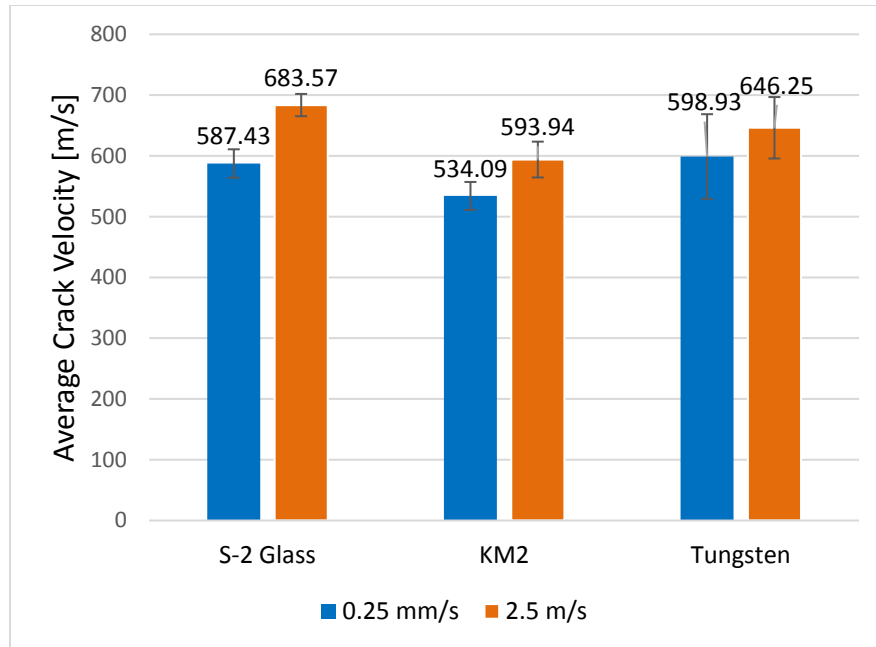


Figure 5.15. Average crack velocity for S-2 glass, KM2, and tungsten fiber reinforced cruciform specimens at 0.25 mm/s and 2.5 m/s.

The longitudinal, shear, and Rayleigh wave speeds for the SC-15 epoxy were calculated using the material properties listed in Table 1 to compare with the average crack speeds obtained for the three types of fiber reinforced cruciform specimens. The calculated longitudinal, shear, and Rayleigh wave speeds under quasi-static loading were 1250 m/s, 815 m/s, and 760 m/s, respectively. The calculated longitudinal, shear, and Rayleigh wave speeds under dynamic loading were 1400 m/s, 914 m/s, and 854 m/s, respectively. According to Rave-Chandar *et al.*, the Rayleigh wave speed of the material sets the limit to the crack speed [38]. In the current study, the S-2 glass, KM2, and tungsten reinforced cruciform specimens under quasi-static loading were 77%, 70%, and 79%, respectively. For dynamic loading, the percentages were 80%, 70%, and 76%, respectively. A summary of the percentage of the average crack speed of the different reinforced specimens to the Rayleigh wave speed under both quasi-static and dynamic loading conditions are presented in Table 5.5.

Table 5.5. Percentage of the average crack speed of the different reinforced specimens to the Rayleigh wave speed of the epoxy

Fiber Type	Percentage for 0.25 mm/s	Percentage for 2.5 m/s
S-2 Glass	77%	80%
KM2	70%	70%
Tungsten	79%	76%

To analyze the average crack velocity further, the Anderson-Darling normality test and the t-test were used. Most of the data sets were significantly drawn from a normally distributed population at the 0.05 level (Table 5.6). Thus, the t-tests were performed comparing the significant difference in the average crack velocity among the different reinforced specimens and the rate dependence between the same specimens. At 0.25 mm/s, significant differences were found between KM2 and the two other reinforced specimens (S-2 glass and tungsten) and no significant difference was found between S-2 glass and tungsten reinforced specimens at the 0.05 level (Table 5.7). Similar results were obtained for those at 2.5 m/s: significant differences between KM2 and the two other reinforced specimens and none between S-2 glass and tungsten reinforced specimens. Investigating the rate dependence of each reinforced specimens, significant differences were obtained for S-2 glass and KM2 between quasi-static and dynamic loading conditions (Table 5.8). No significant difference was found for tungsten with increasing loading velocities.

Table 5.6. Anderson-Darling normality tests for crack velocities

	S-2 glass	KM2	Tungsten
0.25 mm/s	0.71	0.016	0.88
2.5 m/s	0.74	0.82	0.36

Table 5.7. t-tests for crack velocity comparing different reinforced specimens

	S2 vs KM2	S2 vs Tungsten	KM2 vs Tungsten
0.25 mm/s	0.002	0.39	0.025
2.5 m/s	0	0.08	0.026

Table 5.8. t-tests for peak debonding forces comparing rate difference (0.25 mm/s and 2.5 m/s)

S-2 Glass	KM2	Tungsten
0	0	0.27

5.4 Average Interfacial Debonding Crack Geometry

To analyze the crack geometry, the crack length and crack width were plotted as a function of time to study the change in crack geometry as time progressed within the first 2.0 μs . The average crack lengths as a function of time for S-2 glass, KM2, and tungsten fiber reinforced cruciform specimens at 0.25 mm/s and 2.5 m/s are presented in Figures 5.16-5.18, respectively. The crack velocities for both loading rates appeared to be almost linear for the three types of specimens. This observation agrees well with previous findings in literature, e.g., Ravi-Chandar and Knauss [38], that crack propagation occurs at a constant velocity. Ravi-Chandar and Knauss found that the crack velocity is dependent on the stress intensity factor because crack propagation occurs when microcracks linked up [38]. The crack lengths as a function of time for both loading velocities were similar in the beginning of the crack but as the crack progressed to 2 μs , the average crack length for those at 2.5 m/s was higher than those at 0.25 mm/s.

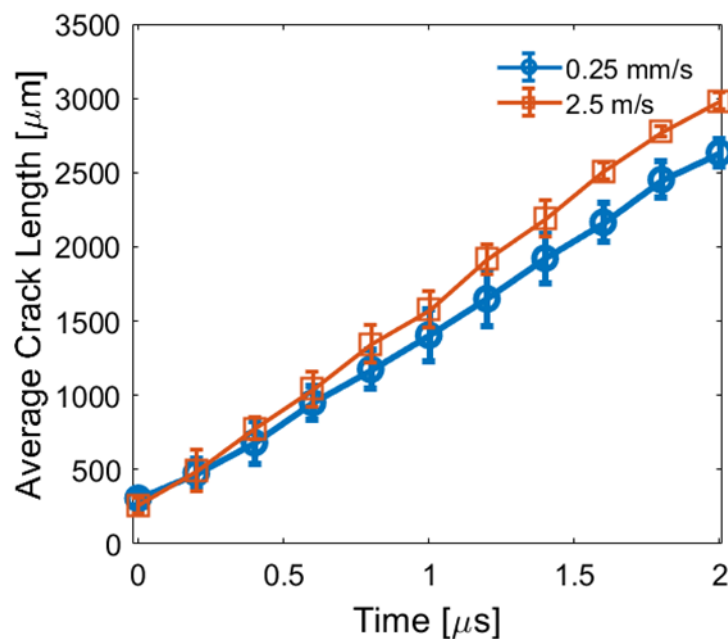


Figure 5.16. Average crack length as a function of time for S-2 glass fiber reinforced cruciform specimens at 0.25 mm/s and 2.5 m/s.

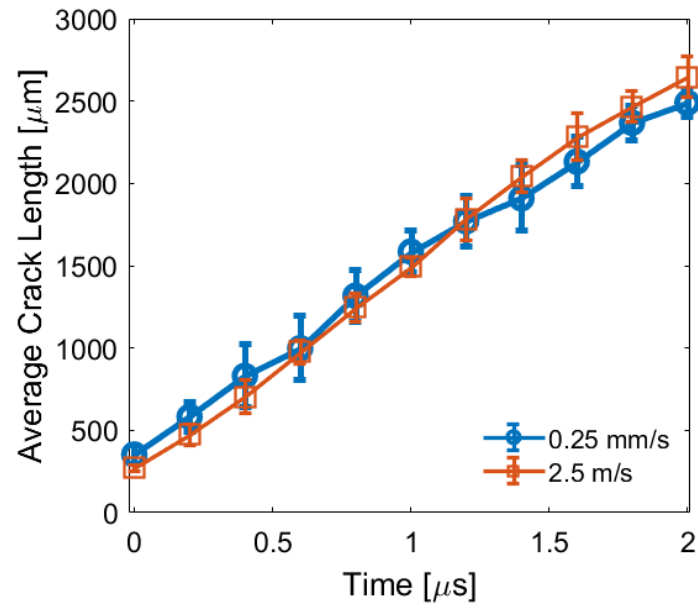


Figure 5.17. Average crack length as a function of time for KM2 fiber reinforced cruciform specimens at 0.25 mm/s and 2.5 m/s.

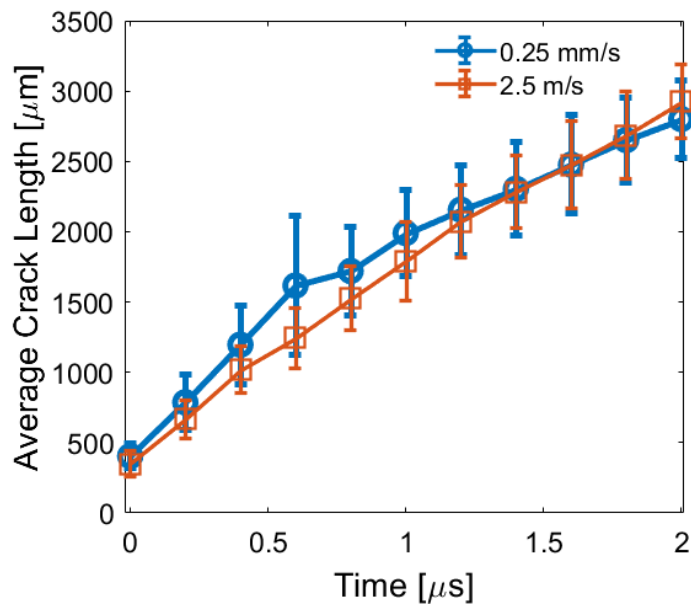


Figure 5.18. Average crack length as a function of time for tungsten fiber reinforced cruciform specimens at 0.25 mm/s and 2.5 m/s.

The crack widths as a function of time for S-2 glass and KM2 fiber reinforced cruciform specimens are presented in Figures 5.19 and 5.20. The starting time (initial frame) of the crack length was chosen to be $t = 0.2 \mu\text{s}$ (instead of $t = 0 \mu\text{s}$ like those for the crack length) because it was difficult to measure the width when the crack first split opened (initial frame) with the current spatial resolution for quasi-static setup. Note that the method to calculate the average crack opening velocity was similar to the method to calculate the average crack velocity (e.g. taking the full crack width divided by the time difference between the initial crack image and the eleventh image and then the calculated value was divided by 2). Figures 5.21 and 5.22 present the ideal elliptical crack geometry progression obtained from the measured average crack length and width from $t = 0.2 \mu\text{s}$ to $t = 2 \mu\text{s}$ for S-2 glass and KM2 reinforced cruciform specimens, respectively.

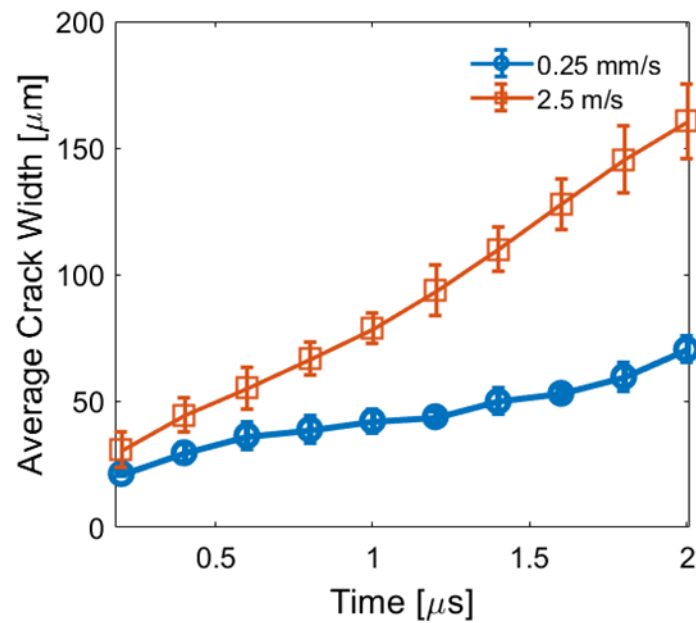


Figure 5.19. Average crack width as a function of time for S-2 glass fiber reinforced cruciform specimens at 0.25 mm/s and 2.5 m/s.

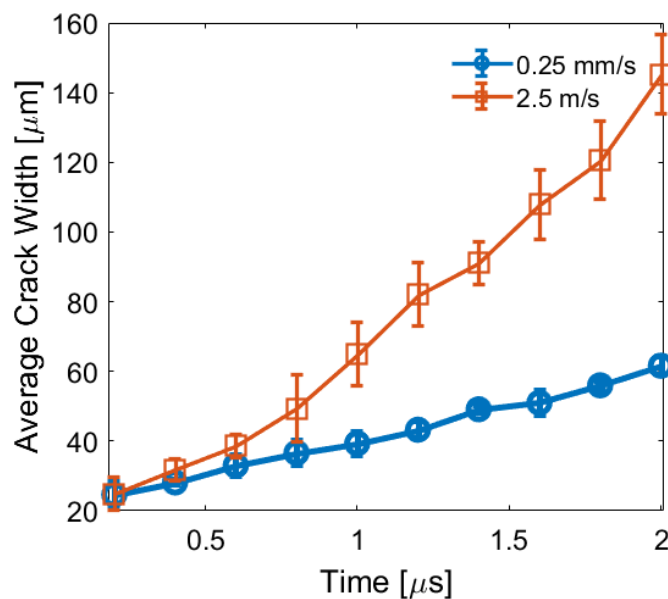


Figure 5.20. Average crack width as a function of time for KM2 fiber reinforced cruciform specimens at 0.25 mm/s and 2.5 m/s.

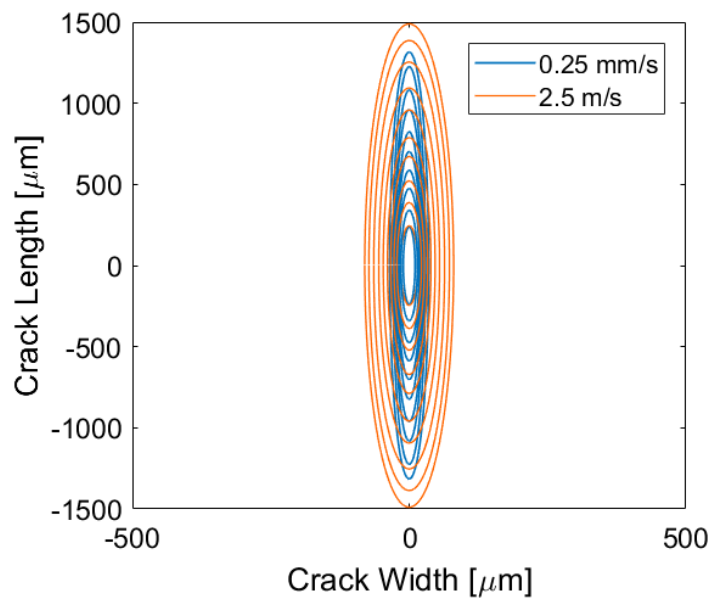


Figure 5.21. Ideal elliptical crack geometry progression obtained from the measured average crack length and width from $t = 0.2 \mu\text{s}$ to $t = 2 \mu\text{s}$ for S-2 glass reinforced cruciform specimens.

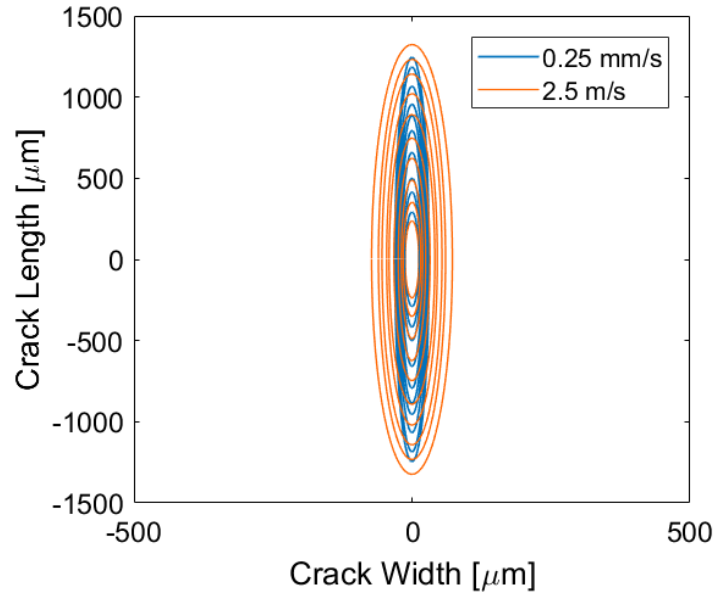


Figure 5.22. Ideal elliptical crack geometry progression obtained from the measured average crack length and width from $t = 0.2 \mu\text{s}$ to $t = 2 \mu\text{s}$ for KM2 glass reinforced cruciform specimens.

For the S-2 glass reinforced cruciform specimens, the average crack opening velocities at 2.5 m/s and 0.25 mm/s were $35.52 \pm 3.49 \text{ m/s}$ and $13.65 \pm 1.30 \text{ m/s}$, respectively. For the KM2 reinforced cruciform specimens, the average crack opening velocities at 2.5 m/s and 0.25 mm/s were $33.44 \pm 3.47 \text{ m/s}$ and $10.28 \pm 1.25 \text{ m/s}$, respectively. Due to the resolution and the nature of the tungsten reinforced cruciform specimens, it was difficult to track the opening width, specifically for quasi-static loading condition. However, from the high-speed images of tungsten experiments, the crack opening velocity for dynamic loading appeared to be higher than that of quasi-static loading too.

The crack opening velocity for dynamic loading was higher than that of quasi-static loading for both fiber-reinforced cruciform specimens. Since the crack opening direction was the same as the loading direction, with higher loading velocity, the crack opening velocity was also expected to be higher. S-2 glass fiber reinforced cruciform specimens revealed a slightly higher average crack opening velocity compared to that of KM2 fiber reinforced cruciform specimens.

From the high-speed images taken from the experiments under both quasi-static and dynamic loadings, the crack profiles were symmetric. Such a phenomenon indicated that the fracture was mode I dominated since mode II fracture would distort the symmetric shape. Moreover, the fibers debonded on both sides of the matrix which revealed that the matrix crack may have initiated from the center along the thickness direction, as shown in Figure 5.23. Such a phenomenon did not contradict previous study [27] when they mentioned the debonding initiated on the loading direction sides of the specimen. It is important to point out that the damage/crack initiation site and debonding initiation site could be different. Note that even though one side of the cruciform specimen was loaded, and the other was fixed, there was no specific side where the fiber would debond. It is interesting to note that for tungsten specimen under quasi-static loading, the specimen only debonded on one side (either left or right).

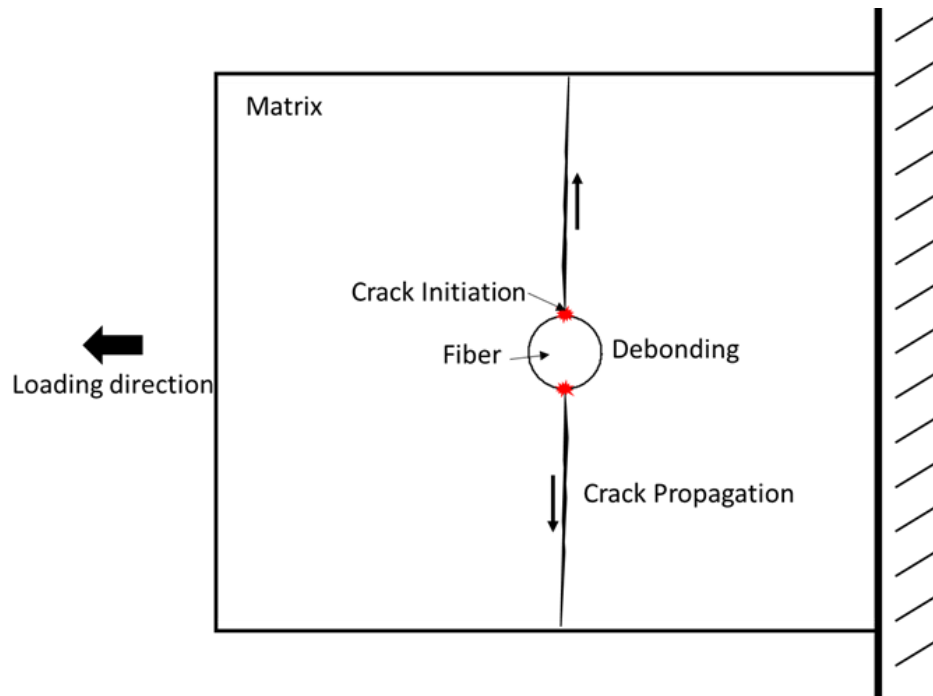


Figure 5.23. A schematic of the cross-section view of the cruciform specimen (fixed on the right-hand side and loaded on the left-hand side).

According to Gundel *et al.* [25], the radial normal stress was maximum at 0° (loading direction) and approaches a negative value (compression) as the angle approaches 90° . On the other hand, the circumferential (hoop) stress was in compression at 0° and becomes maximum (tension) as the angle approaches 90° . Such results from Gundel *et al.*'s concentric cylinder model is aligned with and explains the physical behavior of our transverse failure modes of the single fiber reinforced cruciform specimens. From our imaging views, we observed fiber/matrix debonding initiation at 0° and matrix crack initiation at 90° . Such a result indicated that the maximum radial normal stress occurred at 0° causing the debonding between the fiber and matrix and the maximum hoop stress occurred at 90° causing matrix to initiate crack that traveled from the fiber/matrix interface to matrix surface.

5.5 Failure Surface of the Recovered Cruciform Specimens

The failure surface of the recovered cruciform specimens for all three materials at both loading velocities were examined under a SEM (Figures 5.24-5.27). All reinforced specimens at both loading velocities revealed directional patterns on the failure surface. Such a directional pattern can be referred to as the 'river mark' that is typically found in epoxy or thermoset polymers [62]. The failure surface of the quasi-static specimens appeared to have larger and apparent patterns compared to that of dynamic specimens. Such an appearance may be the result of the rate dependence of the matrix failure mode. These marks indicated that, to some extent, plastic deformation had occurred. Referring to the force-displacement plots from Figures 5.12-1.14, a more brittle failure was found for the specimens under the dynamic loading and a slightly more ductile failure was found for the specimens under quasi-static loading. For quasi-static loading, the larger the 'river mark' patterns could indicate the higher level of plastic deformation the matrix underwent upon loading, resulting in a more ductile behavior in the force-displacement history. Besides the different failure surface of the epoxy matrix, the fiber track, where the fiber was located before debonding, was also observed from the SEM. The fiber track and the fiber surface revealed smooth surfaces.

As previously discussed from the high-speed images, the matrix crack may have initiated from the top and bottom of the cross-section view whereas debonding initiated on the left and right sides of the fiber/matrix interface as indicated in Figure 5.23. In other words, the crack propagated

in the thickness direction from the fiber/matrix interface to the surface of the matrix. Such a phenomenon was also observed through the patterns on the failure surfaces. A recent study on the full field measurements of single fiber composite under transverse debonding under quasi-static rate via a 3D digital imaging correlation performed by Tabiai *et al.* [29] has indicated that upon fiber/matrix debonding in the loading directions (0° and 180°), the matrix crack initiation occurred in the 90° and 270° directions. Even though the reinforcements used in Tabiai *et al.*'s [29] study were macro-fibers, similar results were found in the present study. From the initiation site, horizontal patterns were observed, indicating the crack propagating from the interface to the matrix surface (in the through-thickness direction). Upon the formation of the crack in the initiation site, the crack started to propagate along the fiber direction, both along the interface and the matrix surface.

As the crack propagated in the in-plane direction, the crack speed along the interface appeared to be slower than the crack speed along the surface of the matrix. Such a difference in the crack speed allowed the formation of the angled patterns observed on the failure surface of the recovered specimens. Recovered specimens with no embedded fibers (e.g. pure epoxy) under transverse loading were examined under the SEM. No such patterns were observed for the recovered specimens without embedded fiber. The surface crack speed appeared to exceed the interfacial crack speed because the matrix surface crack speed should be near the Rayleigh wave speed, which is often the limit a crack can propagate at [39]. Furthermore, the adhesive bond between the fiber and matrix tends to be stronger than the cohesive bond of the matrix itself upon crack initiation. In other words, the crack travels across an adhesive bond slower than a cohesive bond when both bonds have initiation sites. Furthermore, the peel failure mechanism may be another cause of the angled 'river mark' patterns. Crack or failure initiated as transverse tension may progressively change to peel as the crack propagates away from the initiation site [62].

The failure mechanisms had a direct effect on the fiber/matrix interfacial debonding behavior. The failure mechanism for S-2 glass fiber reinforced cruciform specimens were similar to that of the tungsten reinforced ones – the fiber material remained intact upon debonding, as shown in Figures 5.24, 5.25, and 5.27. For S-2 glass fiber and tungsten reinforcements, the failure mechanisms were debonding along the fiber/matrix interface and matrix failure. On the other hand,

KM2 fiber reinforced cruciform demonstrated a different failure mechanism which is failure of the KM2 fiber material (fibrillation/fiber splitting), as shown in Figure 5.26. Fibrillation is a common failure mode for aramid fibers like KM2 [63].

Three failure mechanisms were found for KM2 reinforced cruciform specimens: fiber/matrix debonding, matrix failure, and fiber failure. Such failure mechanisms suggest that the interfacial strength between the KM2 fiber and the SC-15 epoxy matrix is higher than the transverse strength of the KM2 fiber itself. The transverse modulus for KM2, S-2 glass, and tungsten fiber materials are 4 GPa, 85 GPa, and ~350 GPa, respectively. Since the transverse modulus for KM2 is much lower than those of S-2 glass and tungsten fiber materials, it is reasonable that the fiber failure mechanism was observed in KM2 fiber reinforced cruciform specimens.

Furthermore, since the KM2 fibers are composed of fibrils bonded together, the results revealed that the bonding between the KM2 fiber and the matrix may be stronger than the bonding between the fibrils of the KM2 fibers. From the SEM images, the KM2 fiber under quasi-static transverse tension remained more intact (only slight fibrillation occurred on the fiber surface) compared to those of under dynamic transverse tension. Such a phenomenon could suggest that the transverse tensile modulus of the KM2 fiber may be strain-rate dependent which was also mentioned in [54].

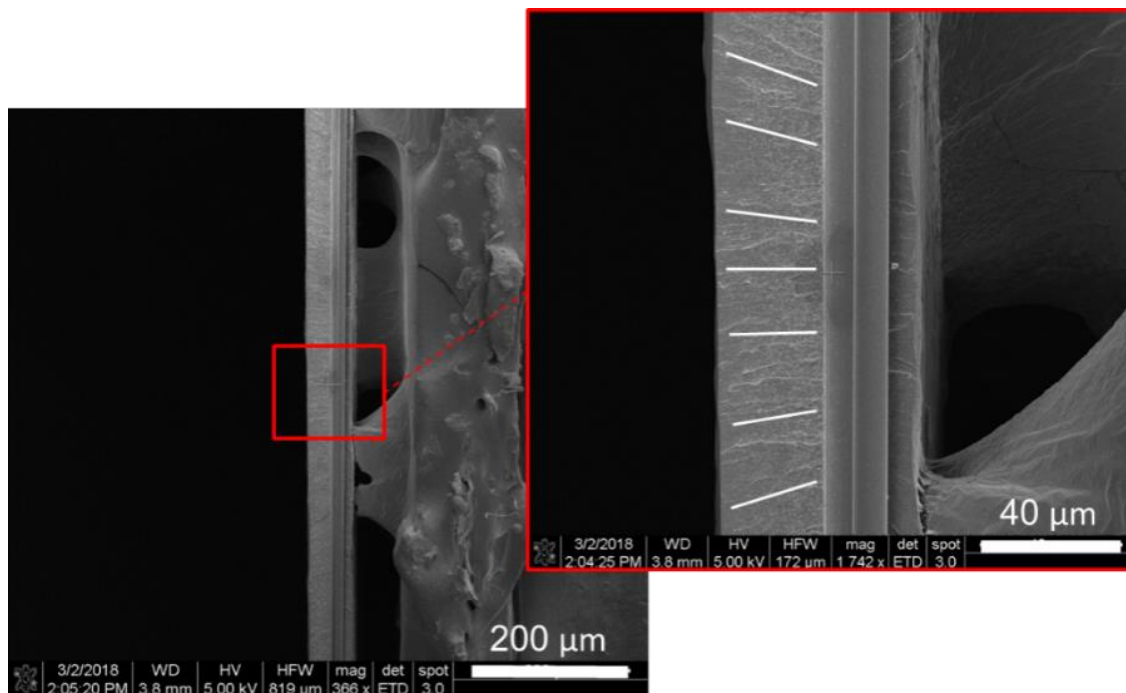


Figure 5.24. SEM imaging of the recovered S-2 glass fiber reinforced cruciform specimen at 2.5 m/s.

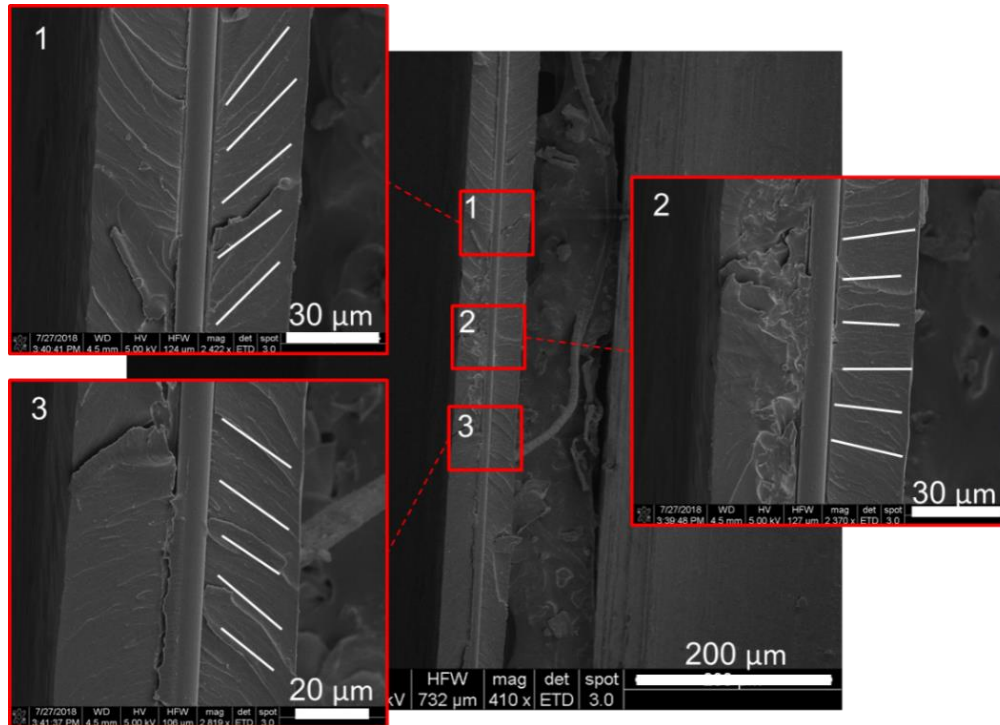


Figure 5.25. SEM imaging of the recovered S-2 glass fiber reinforced cruciform specimen at 0.25 mm/s.

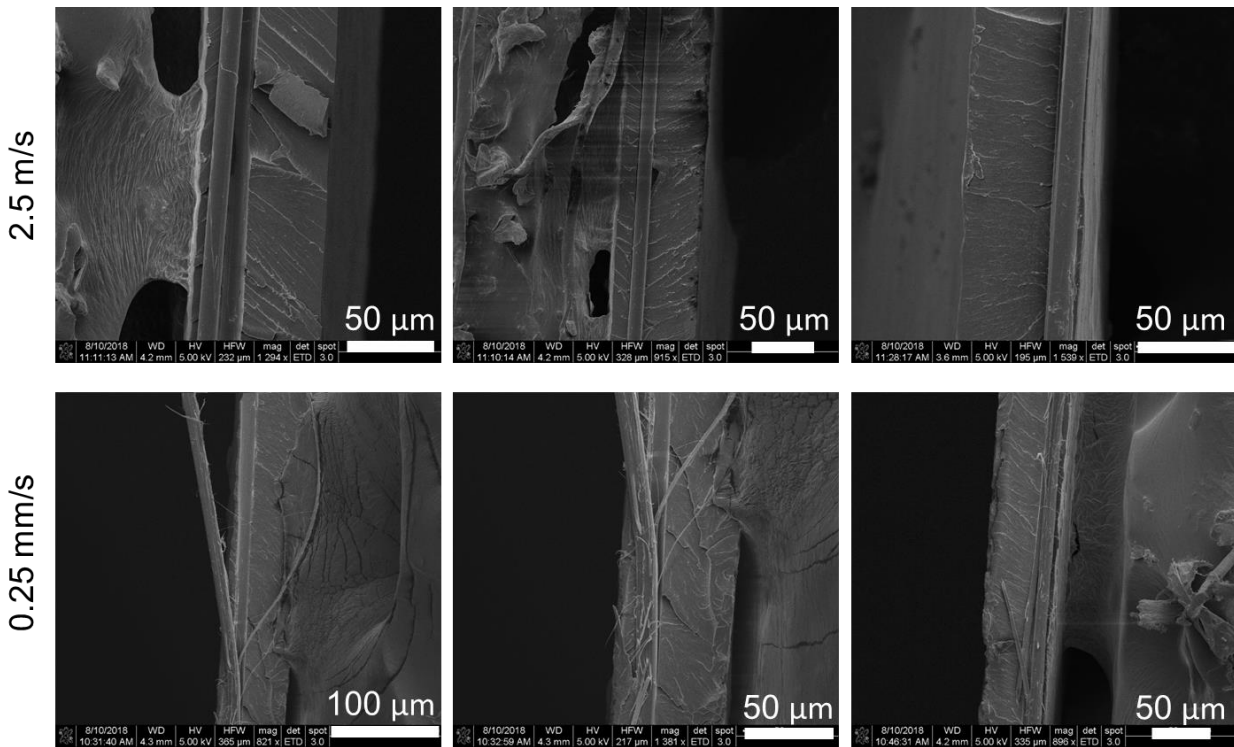


Figure 5.26. SEM imaging of the recovered KM2 fiber reinforced cruciform specimen at 2.5 m/s and 0.25 mm/s.

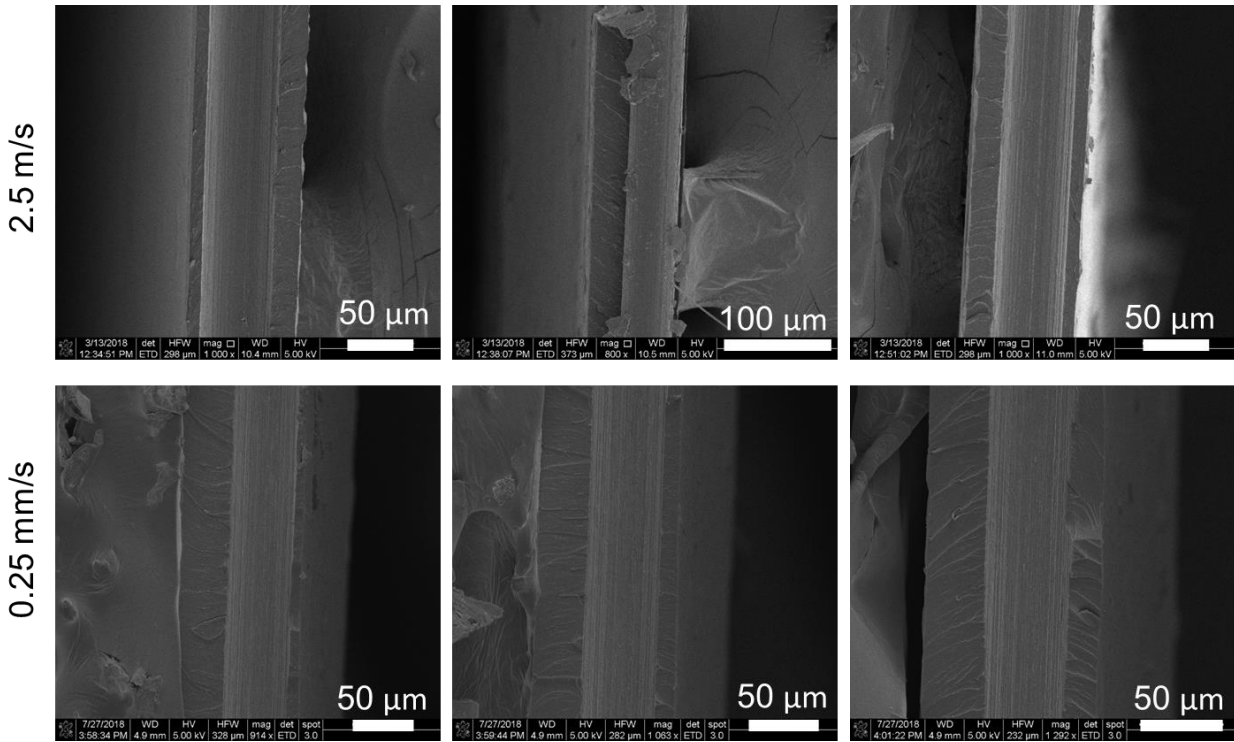


Figure 5.27. SEM imaging of the recovered tungsten reinforced cruciform specimen at 2.5 m/s and 0.25 mm/s.

CHAPTER 6. DYNAMIC VISUALIZATION OF INTERFACIAL SHEAR DEBONDING

(A version of this chapter has been published in Journal of Materials Science [47])

Title: **Visualization of Dynamic Fiber/Matrix Interfacial Shear Debonding**

Authors : Jou-Mei Chu*¹

Benjamin Claus¹

Niranjan Parab²

Daniel O'Brien³

Tao Sun²

Kamel Fezzaa²

Wayne Chen¹

Purdue University, 701 W. Stadium Ave., West Lafayette, IN 47907, U.S.A.¹

X-ray Science Division, Advanced Photon Source, Argonne National Laboratory, 9700 Cass Ave,
Lemont, IL 60439, U.S.A.²

U.S. Army Research Laboratory, 2800 Powder Mill Rd, Adelphi, MD 20783, U.S.A.³

Jou-Mei Chu, chu82@purdue.edu, 909-569-4510

Benjamin Claus, bclaus@purdue.edu

Niranjan Parab, nparab@anl.gov

Daniel O'Brien, daniel.j.obrien58.civ@mail.mil

Tao Sun, taosun@aps.anl.gov

Kamel Fezzaa, fezzaa@aps.anl.gov

Wayne Chen, wchen@purdue.edu

6.1 Abstract

To visualize the debonding event in real time for the study of dynamic crack initiation and propagation at the fiber-matrix interface, a modified tension Kolsky bar was integrated with a high-speed synchrotron X-ray phase contrast imaging setup. In the gage section, the pull-out configuration was utilized to understand the behavior of interfacial debonding between SC-15 epoxy matrix and S-2 glass fiber, tungsten wire, steel wire, and carbon fiber composite Z-pin at pull-out velocities of 2.5 and 5.0 m s⁻¹. The load history and images of the debonding progression were simultaneously recorded. Both S-2 glass fiber and Z-pin experienced catastrophic interfacial debonding whereas tungsten and steel wire experienced both catastrophic debonding and stick-slip behavior. Even though S-2 glass fiber and Z-pin samples exhibited a slight increase and tungsten and steel wire samples exhibited a slight decrease in average peak force; and average interfacial shear stress as the pull-out velocities were increased, no statistical difference was found for most properties when the velocity was increased. Furthermore, the debonding behavior for each fiber material is similar with increasing pull-out velocity. Thus, the debonding mechanism, peak force, and interfacial shear stress were rate insensitive as the pull-out velocity doubled from 2.5 to 5.0 m s⁻¹. Scanning electron microscope imaging of recovered epoxy beads revealed a snap-back behavior around the meniscus region of the bead for S-2 glass, tungsten, and steel fiber materials at 5.0 m s⁻¹ whereas those at 2.5 m s⁻¹ exhibited no snap-back behavior.

Keywords: Kolsky bar, pull-out technique, interfacial shear stress, phase contrast imaging, high-speed synchrotron X-ray

6.2 Introduction

Fiber-reinforced composite materials are widely used, specifically under dynamic loading conditions, due to their high strength-to-weight ratios and high impact resistance. For an effective composite material, the interface between the fiber and matrix must be able to transfer load from fiber into the matrix and subsequently to other fibers. The loss of adhesion at the interface can greatly reduce the material strength. On the other hand, a sudden failure of a strong interface is not desired for applications that require absorption of impact energy. Furthermore, the control of interfacial strength between the fiber and the matrix could be used to control the material properties

of the composite materials. Thus, various techniques have been developed to study the interfacial properties of fiber-reinforced composite materials including the pull-out [1], push-out [2], microbond [3], and single fiber fragmentation methods [4]. Detailed comparisons among these techniques are discussed elsewhere [5, 6].

While most of the studies reported in literature were conducted at quasi-static rates [5, 6, 7], a few of them were also performed under dynamic loading conditions. At a quasi-static loading level, Yang and his coworkers studied the interfacial strengths and failure modes of E-glass fiber-polypropylene obtained by using the pull-out and microbond techniques at 0.01 mm min^{-1} [7]. Adhesive interfacial failure, leaving a clean surface with no residual resin around the debonded area, was found for the pull-out recovered samples [7]. On the other hand, two failure modes were found for the microbond recovered samples: adhesive interfacial failure and cohesive matrix failure (2-7 μm thickness of residual resin was observed around the debonded area of the fibers) [7].

At the dynamic loading level, Hudspeth *et al.* performed pull-out experiments using a modified tension Kolsky bar with a high-speed synchrotron X-ray imaging system. The pull-out speed was 4 ms^{-1} to observe the debonding event of high performance, ultrahigh molecular weight polyethylene fibers in an epoxy matrix [8]. Tamrakar *et al.* also used a modified tension Kolsky bar to study the rate effects of interfacial shear strength and debonding energy for S-2 glass fiber with (3-glycidoxypropyl) trimethoxy silane coupling agent and epoxy resin DER 353 mixed with bis (p-aminocyclohexyl) methane curing agent at $1 \mu\text{m s}^{-1}$ and 1 m s^{-1} using the microbond technique [9]. The interfacial shear strength and debonding energy increased by factors of 1.7 and 2.6 respectively when the loading rate was increased by six orders of magnitude [9]. Li. *et al.* conducted dynamic push-out experiments using a compression Kolsky bar at a sliding rate of 6 m s^{-1} and found that the maximum push-out force increased with increasing loading rate [10]. Tanoglu *et al.* also performed dynamic push-out experiments at 3 mm s^{-1} via a dynamic interphase-loading apparatus (DILA) to obtain the interfacial shear stress and energy absorption and found that the strength and energy absorption of E-glass/epoxy-amine interface are sensitive to loading rate [11, 12]. Greenfield developed a high strain-rate single fiber fragmentation technique to study the interfacial shear stress at 1.2 m s^{-1} [13].

Even though an extensive number of studies have been done on the interfacial properties of fiber reinforced composite materials, it is still uncertain how the crack initiates and propagates leading to the complete failure of the interfaces. Furthermore, the effects of loading rate on the debonding mechanisms needs to be studied. To develop a physical understanding of the dynamic debonding process, the visualization of the interfacial behavior during the debonding event is desired in real time. Since the most common epoxy matrix used in fiber-reinforced composites (e.g. fill/toughened epoxy) is opaque to visible light, typical high-speed imaging techniques are not sufficient to study the sub-surface damage and fracture behavior. Thus, a high-speed synchrotron X-ray phase-contrast imaging (PCI) technique was used to observe the interfacial behavior during the debonding event. The PCI technique provides high spatial and temporal resolutions to capture the failure initiation and progression under dynamic loading [14]. Four reinforcement types: S-2 glass fiber, tungsten wire, steel wire, and carbon fiber composite Z-pin, with SC-15 epoxy bead were used to study the interfacial behavior under high rate loading.

6.3 Materials and Methods

Materials

The interfacial behavior under various loading rates was investigated for an epoxy bead (SC-15, Applied Poleramic, Benicia CA, U.S.) bonded to four types of fiber materials: S-2 glass fiber (Owens Corning, Toledo OH, U.S.), tungsten wire (McMaster-Carr, Elmhurst IL, U.S.) phosphate-coated 1080 carbon steel wire (McMaster-Carr, Elmhurst IL, U.S.), and carbon composite Z-pin. The Z-pins are made from pultruded carbon/epoxy rod stock (DPP Pultrusion, Tilburg, Netherlands). The S-2 glass fiber consists of numerous G-filament continuous glass strands and has a linear density of 675 TEX. Tungsten and steel wires were used because of their high electron densities compared to the SC-15 epoxy bead, which led to high contrast between epoxy bead and the reinforcements. S-2 glass fiber is a common fiber used in fiber reinforced composite materials and Z-pins are commonly used in composite materials in the through-the-thickness direction to reduce delamination [15, 16]. Furthermore, the Z-pins used in this study have a larger diameter as compared to S-2 glass which improved the visibility of the interface. The diameters for S-2 glass fibers, tungsten wire, steel wire, and Z-pins were 11 μm , 50 μm , 150 μm , and 500 μm respectively.

The surfaces of the four types of studied fiber material were cleaned with isopropyl prior to sample preparation to remove impurities from handling. The as-received S-2 glass was treated with an amino-silane and steel wire was treated with phosphate by the manufacturers. No additional surface modifiers or treatments were used on the as-received fiber surface in the current study. The SC-15 epoxy was mixed with a resin to hardener ratio of 100:30 by mass. The epoxy resin was placed in a vacuum chamber at 300 torr for five hours prior to sample preparation to remove trapped gases. After the epoxy was removed from the vacuum chamber, the epoxy was doped with 5% by mass of 1-22 μm -diameter stainless steel microspheres (Cospheric, Santa Barbara CA, U.S.).

For S-2 glass fiber, tungsten and steel wires, the fiber material was placed on a cardboard strip with a 6.35 mm hole punched in the middle and the fiber material running across a slotted aluminum bar. The slot prevented the fiber material from contacting the work surface. The fiber material was fixed to the cardboard strip by placing epoxy adhesive ((DP-190, 3M Inc., St. Paul, MN for S-2; JB Weld, J-B Weld Co., Sulphur Springs, TX for tungsten and steel wires) on both ends of the fiber (Figure 6.1). Then, SC-15 epoxy beads were placed on the middle section of fiber using a steel pin with a diameter of 150 μm . Once the epoxy was cured (48 hours) at room temperature and in normal atmosphere, a set screw was placed on one end of the cardboard for mounting to the Kolsky bar apparatus. Furthermore, the right-hand side of the sample was snipped away along the dashed lines prior to each experiment as indicated in Figure 6.1. Since the right-hand side of the sample was snipped away, the prestress of laxation of fibers during sample preparation was avoided. Furthermore, prior to each experiment, the load signal was checked to ensure the starting point was from 0 to avoid pre-stressing the fiber material.

A different method was used for Z-pin sample preparation due to its larger diameter. First, a silicone rubber mold, made from pourable silicone rubber (OOMOO[®] 30, Smooth-On, Macungie PA, U.S.), was produced using an aluminum form (Figure 6.2). Then, SC-15 epoxy was filled in the circular cavity (as indicated in Fig. 2), and the Z-pin was placed in the filled epoxy cavity which was held in place by a Teflon cylinder. The bead size was 1.0 mm in height (embedded length) and 1.2 mm in diameter. The SC-15 epoxy was then cured for 48 hours at room temperature and in normal atmosphere before removing the Z-pin samples from the silicone rubber mold.

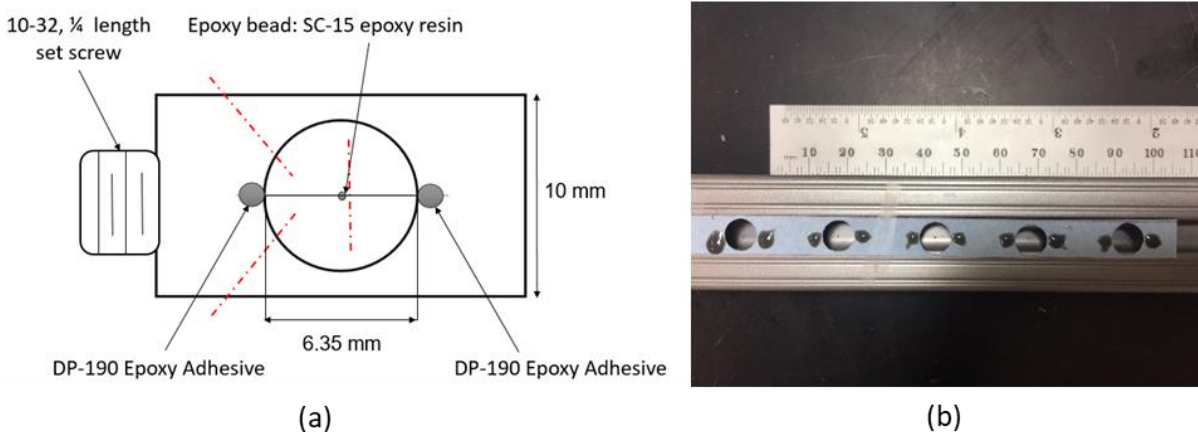


Figure 6.1. A schematic of S-2 glass, tungsten, and steel sample preparation. The two ends of the fiber were fixed in place by epoxy adhesives (DP 190 for S-2 glass and tungsten samples and JB Weld for steel samples) and SC-15 epoxy bead was formed on the center of the fiber. Prior to every experiment, the right-hand side of the sample was snipped away along the dashed lines. (b) Fiber material (with epoxy bead on the fiber) placed across a cardboard strip on top of a slotted aluminum bar.

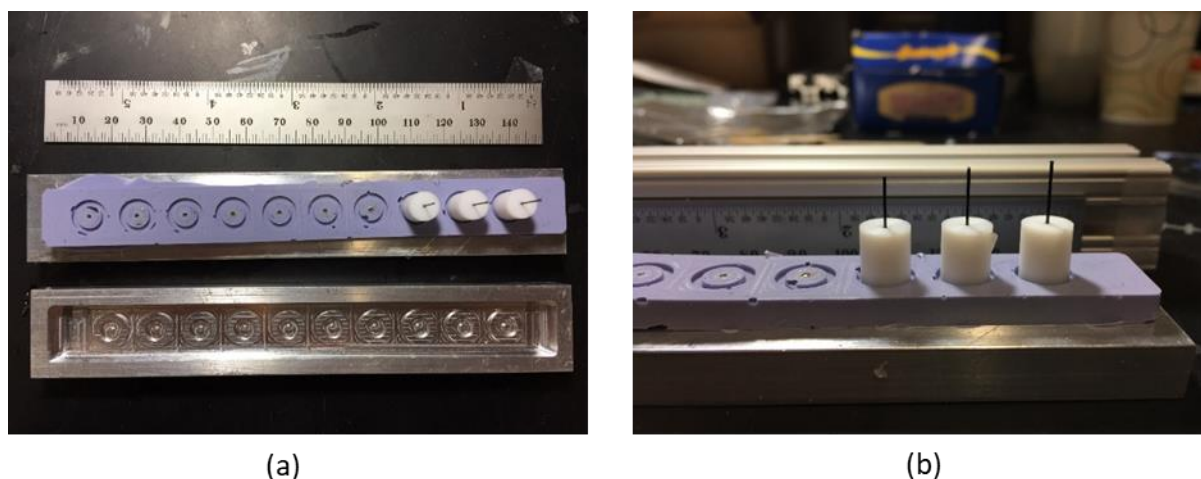


Figure 6.2. (a) Sample preparation for Z-pin. OOMOO® 30 pourable silicone rubber was poured in the aluminum mold. Once cured, the silicone rubber was used to prepare the Z-pin samples. (b) The Z-pin was held in place by machined Teflon cylinders.

High Speed Synchrotron X-Ray Imaging

The high-speed synchrotron X-ray PCI technique was adapted to visualize the *in-situ* debonding initiation and progression along the fiber/matrix interface. X-ray PCI was performed at

beamline 32-ID-B of the Advanced Photon Source (APS) in Argonne National Laboratory, IL, USA. The high-speed X-ray PCI technique has been utilized to study different material behaviors (e.g. energetic materials, high performance fibers, sand particles, bovine bones, and S-2 glass cruciform composite materials) under dynamic loading conditions [8, 14-21]. The high-energy (~25 keV) X-ray allows imaging through opaque materials with high spatial and temporal resolutions. High intensity synchrotron X-rays penetrate through the polymer materials studied here and hence can be used to observe the behavior at the fiber-matrix interface.

At beamline 32-ID-B, X-rays are generated using an undulator (1.8 cm period), where 24 bunches of electrons are maintained in a circular ring (circumference = 1140 m). Two sets of shutters, one slow and one fast, were used at the beamline to define a short time window for the intense white X-ray beam to pass through in order to prevent damage of the experimental apparatus and sample. The X-ray beam is collimated using an adjustable slit (1-2 mm²). A single crystal scintillator (Lu₃Al₅O₁₂:Ce, thickness: 100 μm) was used to convert the transmitted X-rays into visible light which was then captured using a high-speed camera (Shimadzu HPV-X2, Kyoto, Japan) via a 45-degree mirror and an objective lens 5×, 10×, or 20× magnification (depending on desired field-of-view and spatial resolution). The pixel resolutions were 6, 3, and 1.5 μm/pixel for the 5×, 10×, and 20× lenses, respectively.

Experimental Setup

A modified tension Kolsky bar was used because of space limitations inside the beam line hutch [18]. The transmission bar from a traditional Kolsky bar setup was replaced by a load cell to record the load history. The incident bar had a diameter of 12.7 mm and a length of 2200 mm and was fabricated from Aluminum 7075-T6. The coaxial brass striker tube used to generate tensile loading had an outer diameter of 19 mm and an inner diameter of 17 mm with a length of 900 mm and was accelerated by air (a gas gun). A two-layer annular shape masking tape (~0.3 mm) was used as the pulse shaper. A 5-lbf quartz load cell (Model 9712B5, Kistler, Amherst NY, U.S.) was used for S-2 glass fiber, tungsten wire, and steel wire experiments, while a 5000-lbf quartz load cell (Model 9212B, Kistler, Amherst NY, U.S.) was used for the Z-pin experiments. The load cell was fixed on a rigid three-dimensional adjustable stage to record the loading history in the sample. The schematic of the experimental setup is presented in Figure 6.3.

The experimental setups for the S-2 glass, tungsten and steel samples and Z-pin samples were slightly different due to the difference in sample preparation. For S-2 glass fiber, tungsten, and steel samples, the set screw was previously fixed on the cardboard which was then mounted to the incident bar (Figure 6.4). The epoxy bead was held in place by a stainless steel bead holder (a slotted, hollow stainless steel pin). The bead holder was then mounted on a slotted screw which was fixed on the load cell. For Z-pin samples, the Z-pin was clamped between the jaws of a custom grip that was mounted on the incident bar (Figure 6.5). The epoxy bead was held in place by a machined thumb screw which was then mounted on the load cell. The squares around the epoxy beads shown in Figs. 4 and 5 indicate the X-ray window.

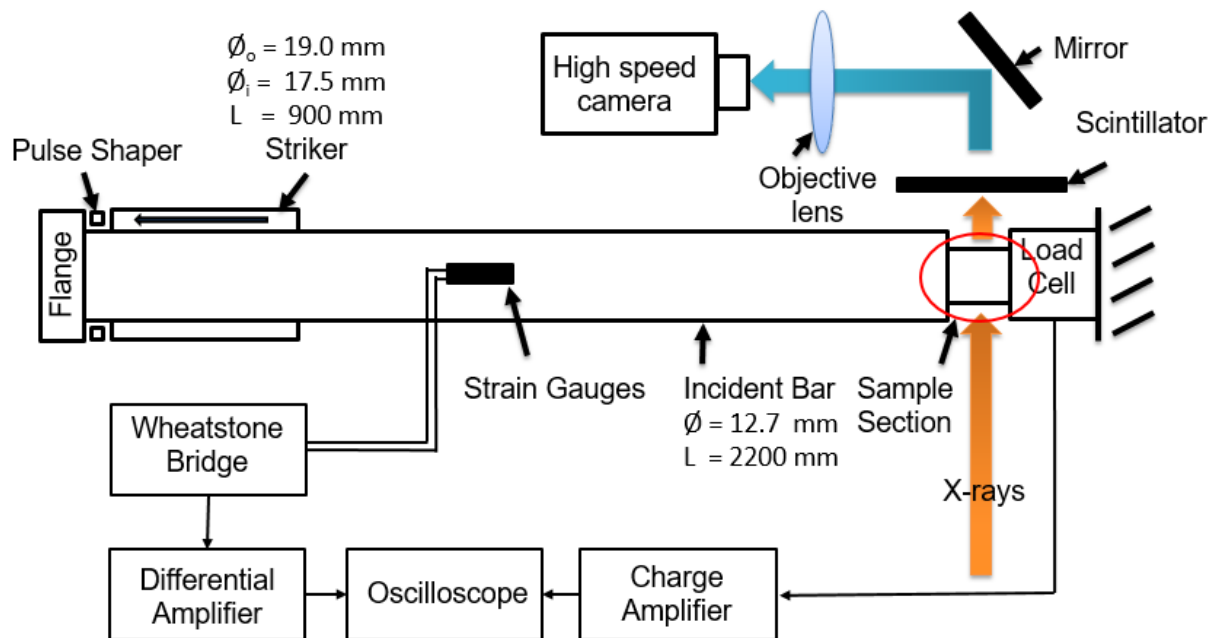


Figure 6.3. A schematic of the experimental setup in APS Beam line 32 ID-B. The section circled indicates the sample section which is further illustrated in Figs. 4 and 5.

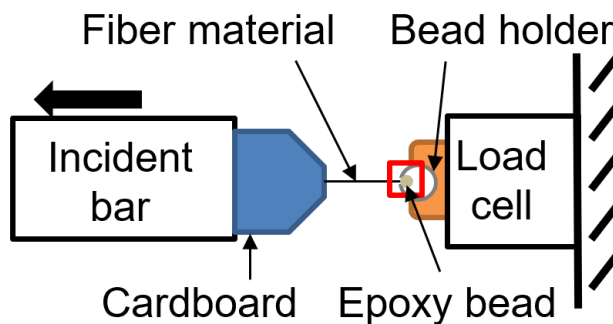


Figure 6.4. Schematic of S-2 glass fiber, tungsten, and steel sample setup. The square around the epoxy bead indicates the X-ray window.

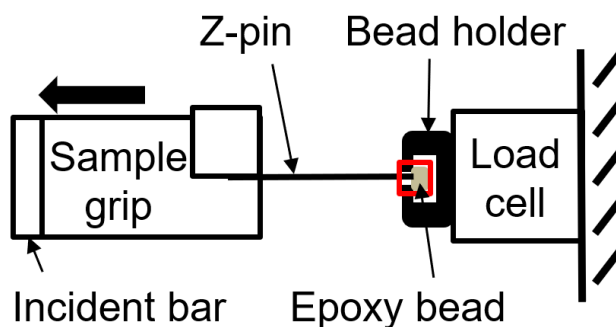


Figure 6.5. Schematic of Z-pin sample setup. The square around the epoxy bead indicates the X-ray window.

6.4 Results

The interfacial behaviors for S-2 glass, tungsten, steel, and Z-pin fiber materials with SC-15 epoxy were studied at pull-out velocities of 2.5 and 5.0 m s⁻¹. At least ten experiments were performed for each fiber material at each velocity. Two interfacial debonding mechanisms were observed from the four fiber materials studied: catastrophic and stick-slip debonding. The average peak debonding forces and interfacial shear stresses (IFSS) of the four fiber materials at 2.5 and 5.0 m s⁻¹ are listed in Table 1. With the known diameters and the obtained peak forces, the interfacial shear stress (IFSS) was calculated via equation (1) [9] where F is the peak debonding force, d is the diameter of the fiber, and l is the embedded length. Due to the large variation of the

bead size for S-2 glass, tungsten, and steel fiber materials, the embedded lengths (listed in Table 1) were measured for each sample prior to every experiment using the image processing software ImageJ [22].

$$\tau = F/(\pi dl) \quad (1)$$

From Table 6.1, the S-2 glass fiber samples exhibited the lowest and Z-pin samples the highest average peak forces. However, S-2 glass fiber at 5.0 m s^{-1} exhibited the highest average interfacial shear stress. Furthermore, for S-2 glass fiber and Z-pin samples, an increase in average peak force and average interfacial shear stress was observed as the pull-out velocity doubled. In contrast, the peak force and interfacial shear stress were observed to decrease as the pull-out velocity was doubled for tungsten and steel samples.

Table 6.1. Peak forces and interfacial shear stresses for the four studied fiber materials at 2.5 and 5.0 m s⁻¹ averaged across all experiments.

Material	Pull-out Velocity (m s ⁻¹)	Average Peak Force (N)	Average IFSS (MPa)	Embedded Length (μm)
S-2 glass	2.5	0.22 ± 0.07	15.73 ± 6.84	421 ± 58
S-2 glass	5.0	0.33 ± 0.10	22.08 ± 9.48	451 ± 85
Tungsten	2.5	2.39 ± 1.10	7.26 ± 3.68	694 ± 52
Tungsten	5.0	1.49 ± 0.73	4.34 ± 2.45	759 ± 103
Tungsten (no particles)	2.5	1.28 ± 0.75	9.77 ± 5.56	827 ± 43
Steel	2.5	7.02 ± 4.32	16.50 ± 9.86	914 ± 75
Steel	5.0	5.32 ± 2.24	11.35 ± 4.88	998 ± 79
Steel (no particles)	2.5	10.61 ± 2.23	22.40 ± 4.95	1009 ± 70
Z-pin	2.5	28.79 ± 8.43	19.12 ± 5.60	1000
Z-pin	5.0	29.94 ± 12.13	19.89 ± 8.06	1000

S-2 Glass Fiber

S-2 glass fiber samples exhibited catastrophic debonding with both pull-out rates (2.5 and 5.0 m s⁻¹) which can be clearly seen from the sudden drop in the force history after the peak force was reached (Figures 6.6 and 6.7). The high-speed X-ray images and the corresponding force-time history for a representative S-2 glass fiber sample at the tensile velocity of 2.5 m s⁻¹ are presented in Figure 6.6. The epoxy bead started to align itself upon loading which caused a change in slope in the force history (Figure 6.6a). Then, the fiber started to pull out, causing a minor drop in the

load (Figure 6.6b). However, the pull-out load further increased until the peak force was reached (Figure 6.6c and 6.6d). The increasing load after Figure 6.6b may have been caused by the epoxy forming a shell behind the epoxy bead which, in turn, required higher force for the fiber to be pulled out. However, this phenomenon was not observed in every S-2 glass experiment. By observing the epoxy residue bead in front of the epoxy bead (pointed with an arrow in Figure 6.6a-d), the movement of glass fiber pull-out initiation and progression could be observed.

The high-speed X-ray images and the corresponding force-time history for S-2 glass fiber at 5.0 m s^{-1} (Figure 6.7) did not reveal the intermediate peaks that were observed in Figure 6.6. In the high-speed X-ray images in Figure 6.7, two small residual epoxy beads were observed in front of the epoxy bead (pointed with an arrow in Figure 6.7). Observing these two beads revealed that the fiber started to pull out after reaching the peak debonding force (Figure 6.7d). Furthermore, the dark particles (dots) observed in the beads were the stainless-steel particles added during sample preparation. These particles were also observed in the beads in tungsten, steel, and Z-pin samples.

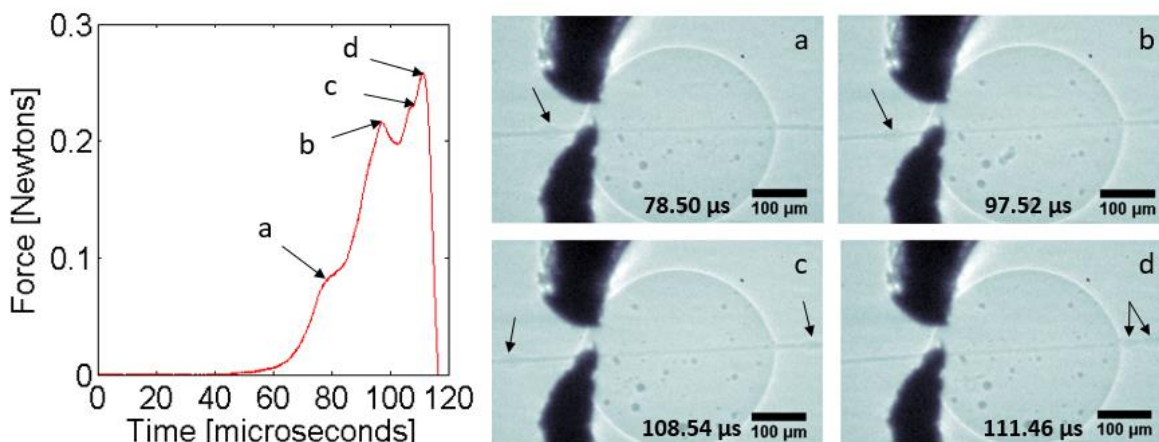


Figure 6.6. Force-time response and the corresponding pull-out image sequence of S-2 glass fiber at 2.5 m s^{-1} with 1 million frames per second recording speed with 200 ns exposure time per frame and a 20 \times lens. Epoxy bead residues were observed in front of and behind the bead which could be the cause of slope changes in the force history. The bead pointed to by the arrows allows us to track the debonding initiation and progression.

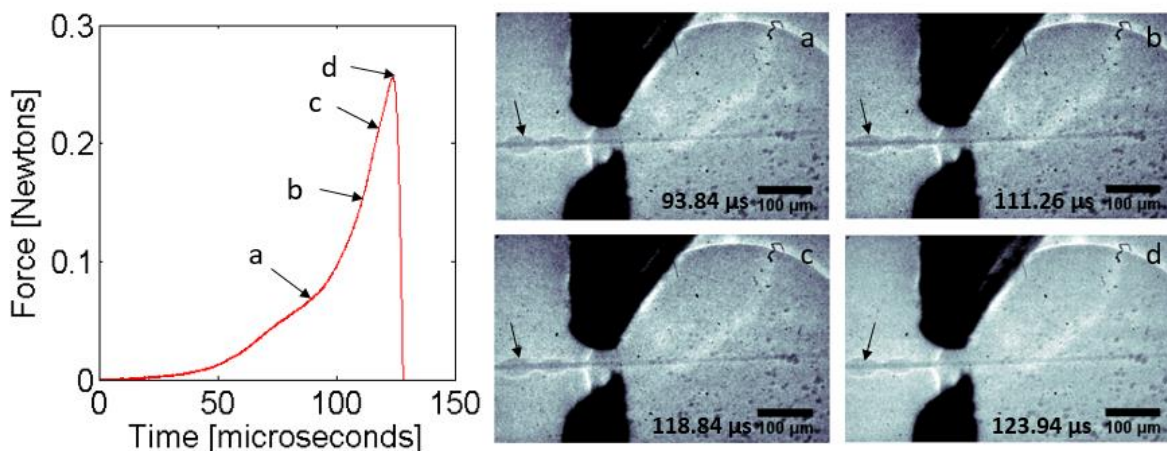


Figure 6.7. Force-time response and the corresponding pull-out image sequence of S-2 glass fiber at 5.0 m s^{-1} with 2 million frames per second recording speed with 200 ns exposure time per frame and a $20\times$ lens. The bead pointed by the arrows allows us to track the debonding initiation and progression.

Tungsten Wire

Tungsten wire pull-out experiments exhibited both catastrophic and stick-slip interfacial debonding at both 2.5 and 5.0 m s^{-1} . A sudden drop after the peak force indicated a catastrophic debonding mechanism, whereas an oscillation back to zero after the peak force indicated a stick-slip debonding mechanism. The high-speed X-ray images and the corresponding force-time history for representative tungsten wire samples at tensile pull-out velocities of 2.5 and 5.0 m s^{-1} are presented in Figures 6.8 and 6.10, respectively.

At the pull-out velocity of 2.5 m s^{-1} , the bead first came into contact with the bead holder (Figure 6.8a). Then, the bead aligned itself and the tungsten wire started to pull out upon loading (Figure 6.8b). The tungsten wire continued to pull out (Figure 6.8c) and the tail of the wire was observed near the end of the pull-out event (Figure 6.8d). The pre-crack (as indicated with an arrow) in Figure 6.8 opened up as the load progressed. A typical stick-slip debonding mechanism is shown in Figure 6.8. However, catastrophic debonding was also observed at this velocity as shown in Figure 6.9a.

At the pull-out velocity of 5.0 m s^{-1} , the meniscus started to stretch as loading progressed (as indicated with an arrow in Figure 6.10a). Then, upon reaching the first peak of the force history, the meniscus and the fiber surface debonded causing a snapback behavior in the meniscus region (as indicated with an arrow in Figure 6.10b). The tungsten wire continued to pull out and crack initiation was observed near the interface between the meniscus and the fiber surface (as indicated with an arrow in Figures 6.10c and 6.10d). Again, Figure 6.10 depicts a typical stick-slip debonding force history whereas Fig. 9b depicts a typical catastrophic debonding force history at 5.0 m s^{-1} .

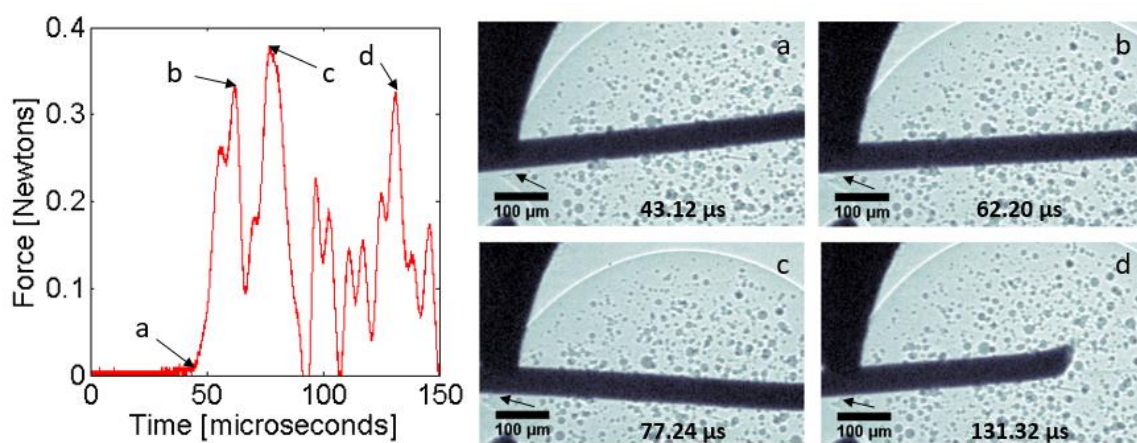


Figure 6.8. Force-time response and the corresponding pull-out image sequence of tungsten wire at 2.5 m s^{-1} with 1 million frames per second recording speed with 200 ns exposure time per frame and a $20\times$ lens. The regions pointed by an arrow indicate the appearance of cracks.

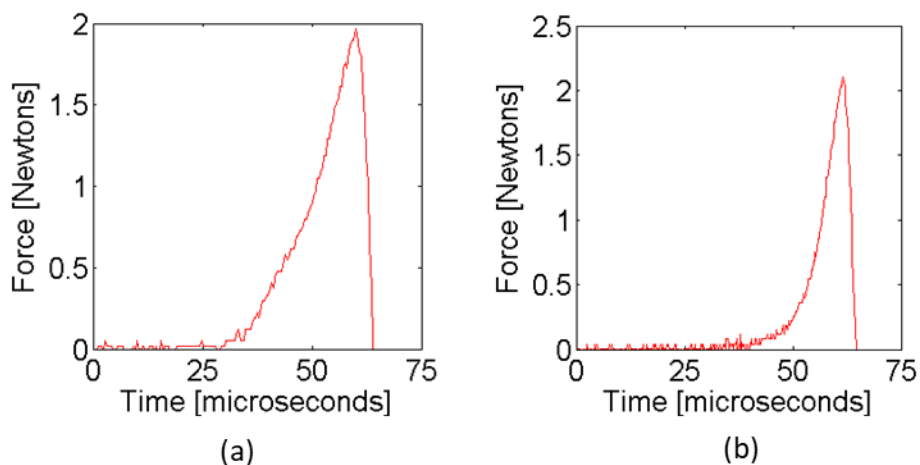


Figure 6.9. (a) A typical force-time response of catastrophic debonding mechanism of tungsten wire at 2.5 m s^{-1} and (b) 5.0 m s^{-1} .

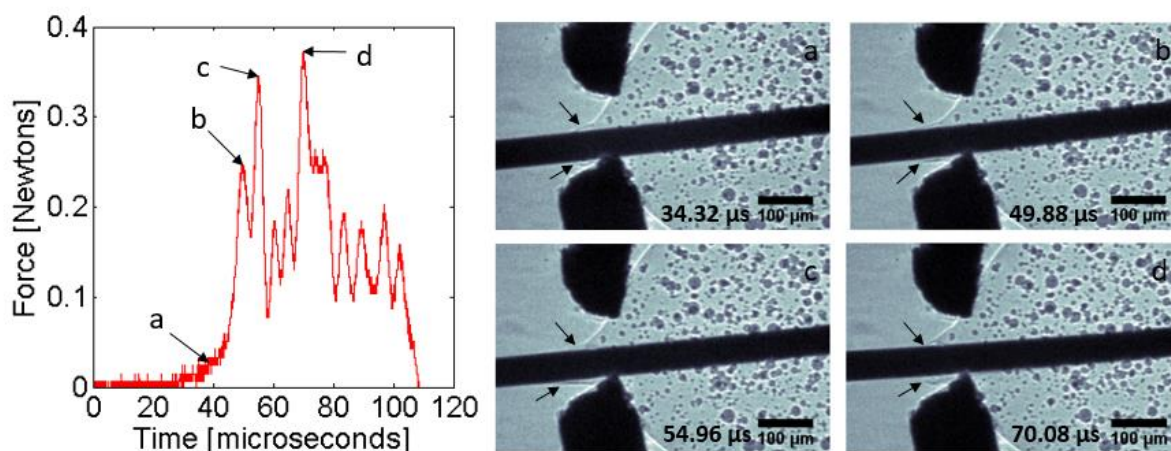


Figure 6.10. Force-time response and the corresponding pull-out image sequence of tungsten wire at 5.0 m s^{-1} with 1 million frames per second recording speed with 200 ns exposure time per frame and a $20\times$ lens. The regions pointed by an arrow indicate the appearance of cracks.

Steel Wire

Steel wire samples also displayed both catastrophic and stick-slip interfacial debonding mechanisms under both 2.5 and 5.0 m s^{-1} . From Figure 6.11 (2.5 m s^{-1}), catastrophic debonding was observed from the force history. The bead came into contact with the bead holder (Figure

6.11a). Then, the interface between the meniscus and fiber surface started to debond (pointed with an arrow in Figures 6.11b and 6.11c) and finally reached the peak force (Figure 6.11d). A typical stick-slip debonding at 2.5 m s^{-1} is shown in Figure 6.11a.

Stick-slip debonding was observed at 5.0 ms^{-1} (Figure 6.13). After the bead came into contact with the bead holder (Figure 6.13a), slight debonding was first observed on the top interface between the meniscus and fiber surface (pointed with an arrow in Figure 6.13b), followed by debonding on the bottom interface between the meniscus and fiber surface (pointed with an arrow Figure 6.13c). As the steel wire continued to pull out, the crack on the interface became more apparent (Figure 6.13d). A typical catastrophic debonding at 5.0 m s^{-1} is shown in Figure 6.12b.

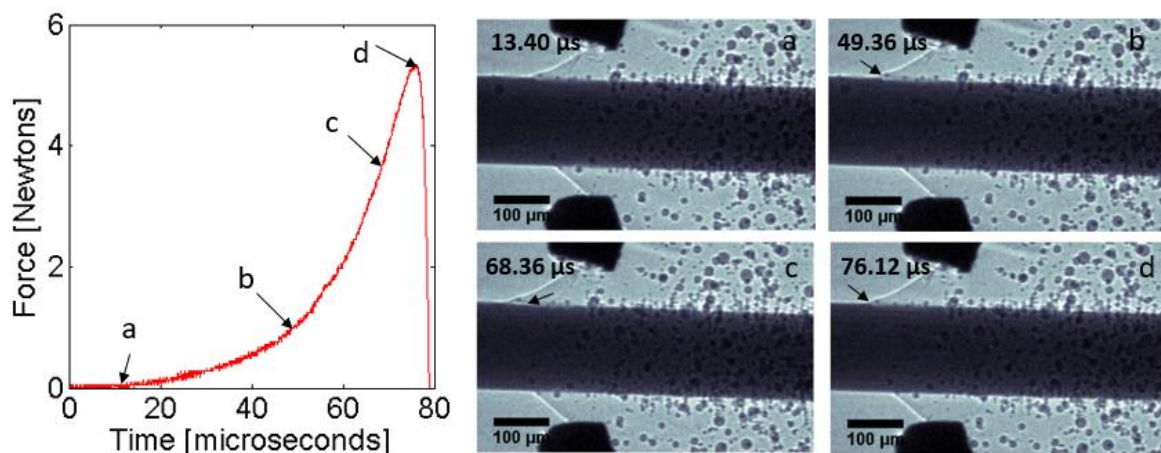


Figure 6.11. Force-time response and the corresponding pull-out image sequence of steel wire at 2.5 m s^{-1} with 1 million frames per second recording speed with 200 ns exposure time per frame and a $20\times$ lens. The regions pointed by an arrow indicate the appearance of cracks.

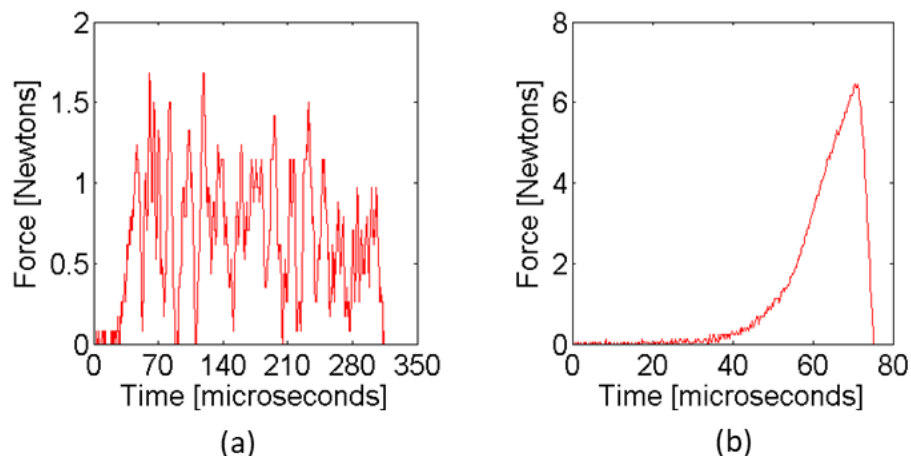


Figure 6.12. A typical force-time response of stick-slip debonding mechanism of tungsten wire at 2.5 m s^{-1} and (b) a typical force-time response of catastrophic debonding mechanism of tungsten wire at 5.0 m s^{-1} .

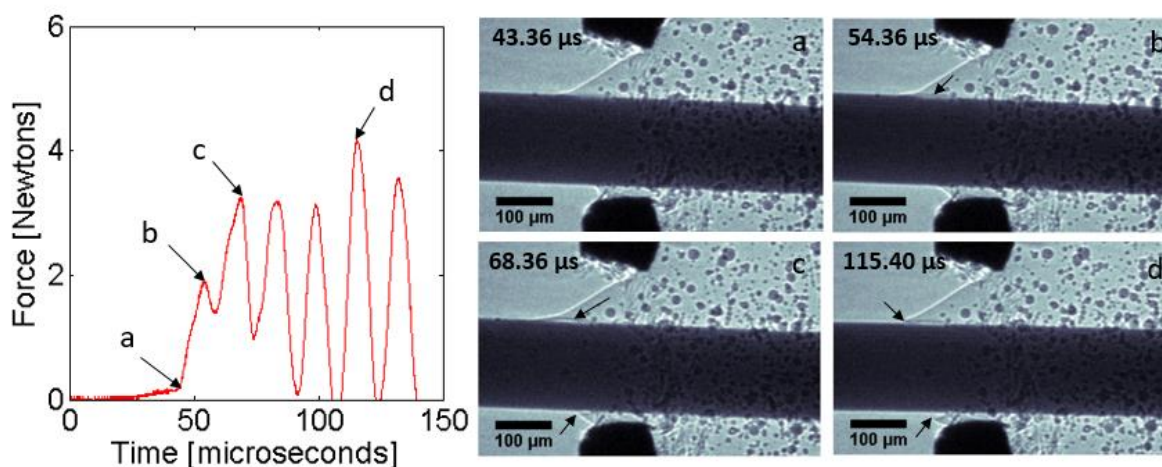


Figure 6.13. Force-time response and the corresponding pull-out image sequence of steel wire at 5.0 m s^{-1} with 1 million frames per second recording speed with 200 ns exposure time per frame and a $20\times$ lens. The regions pointed by an arrow indicate the appearance of cracks.

Z-pin

The debonding mechanism for Z-pin samples was catastrophic, similar to those obtained for the S-2 glass fiber samples. Due to the larger diameter of the Z-pin samples, the interface between the fiber and matrix was more apparent compared to those of the other fiber materials. Upon loading at 2.5 m s^{-1} , the epoxy bead fully contacted the bead holder (Figure 6.14a). Then,

cracks began to initiate at the contacting area between the epoxy bead and the bead holder (pointed with an arrow in Figures 6.14b and 6.14c). Finally, the peak debonding force occurred where the entire pin started to slide through the epoxy bead (Figure 6.14d). A similar debonding mechanism was observed for Z-pin samples pulled at a tensile velocity of 5.0 m s^{-1} (Figure 6.15). In Figures 6.15c and 6.15d, cracks were observed to propagate across the region pointed with an arrow. These were caused by a thin layer of epoxy that was formed around the neck of the pin during sample preparation.

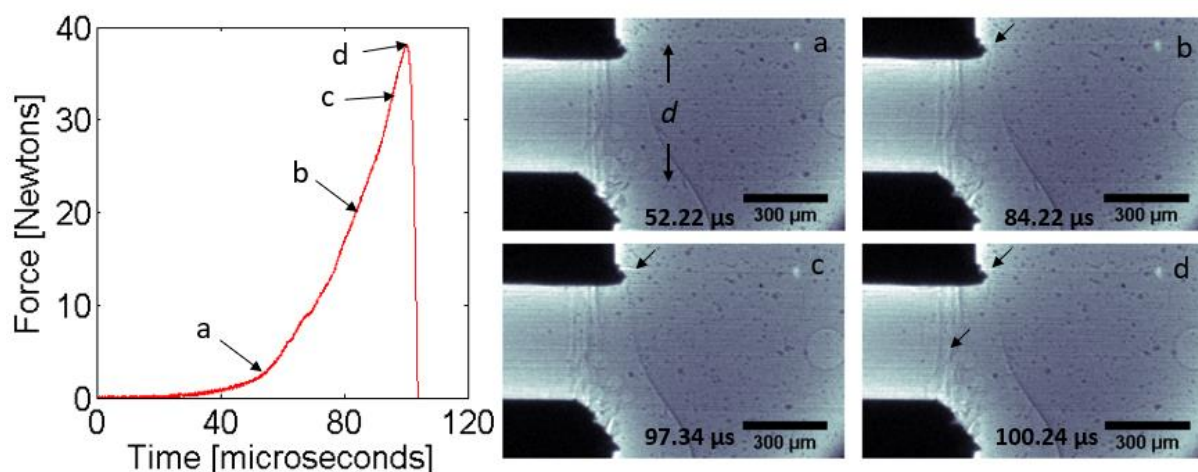


Figure 6.14. Force-time response and the corresponding pull-out image sequence of Z-pin at 2.5 m s^{-1} with 1 million frames per second recording speed with 200 ns exposure time per frame and a $10\times$ lens. The regions pointed by an arrow indicate the appearance of cracks. The diameter of the pin is also indicated in (a).

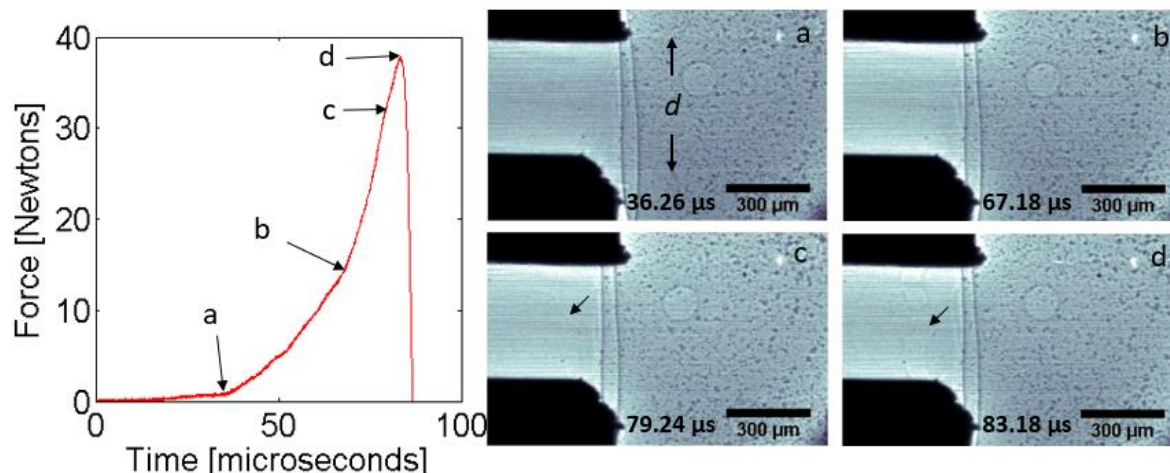


Figure 6.15. Force-time response and the corresponding pull-out image sequence of Z-pin at 5.0 m s^{-1} with 1 million frames per second recording speed with 200 ns exposure time per frame and a $10\times$ lens. The regions pointed by an arrow indicate the appearance of cracks. The diameter of the pin is also indicated in (a).

Effect of stainless steel microsphere inclusions on tungsten and steel samples

As mentioned previously, tungsten and steel samples exhibited both catastrophic and stick-slip debonding behaviors. Such phenomenon may be caused by the inclusion of stainless steel microspheres in the epoxy beads of tungsten and steel samples. Thus, 10 experiments were performed for tungsten and steel samples each at 2.5 m s^{-1} to observe the debonding behavior. Instead of mixing the stainless steel microspheres, the epoxy was doped with 0.1% by mass of $<5 \text{ }\mu\text{m}$ -diameter Iron (III) oxide (Sigma-Aldrich, St. Louis, MO, U.S.) to improve its contrast. The peak debonding forces and interfacial shear stresses for both fiber materials with no embedded stainless steel microspheres are shown in Table 1 (indicated as ‘no particles’). The average interfacial shear stresses for tungsten and steel are both higher for the samples without stainless steel particles embedded.

Furthermore, only stick-slip debonding behavior was found for both tungsten and steel samples from the force-time history (Figures 6.16 and 6.17). From the high-speed X-ray images for tungsten, the tungsten wire first came into contact with the bead holder (Figure 6.16a). Then, the wire started to pull out of the epoxy bead after reaching the peak debonding force (Figure 6.16b). The wire continued to pull out of the epoxy bead (Figures 6.16c and 6.16d). For steel wire, the load started to build (Figure 6.17a) and reached the peak debonding force (Figure 6.17b). Then,

the steel wire started to slide through the epoxy bead (Figures 6.17c and 6.17d). Since only stick-slip debonding was observed in both fiber materials, the catastrophic debonding behavior found in tungsten and steel samples with stainless steel microspheres was speculated to be caused by the inclusion of stainless steel microspheres. These particles act as defects along the interface.

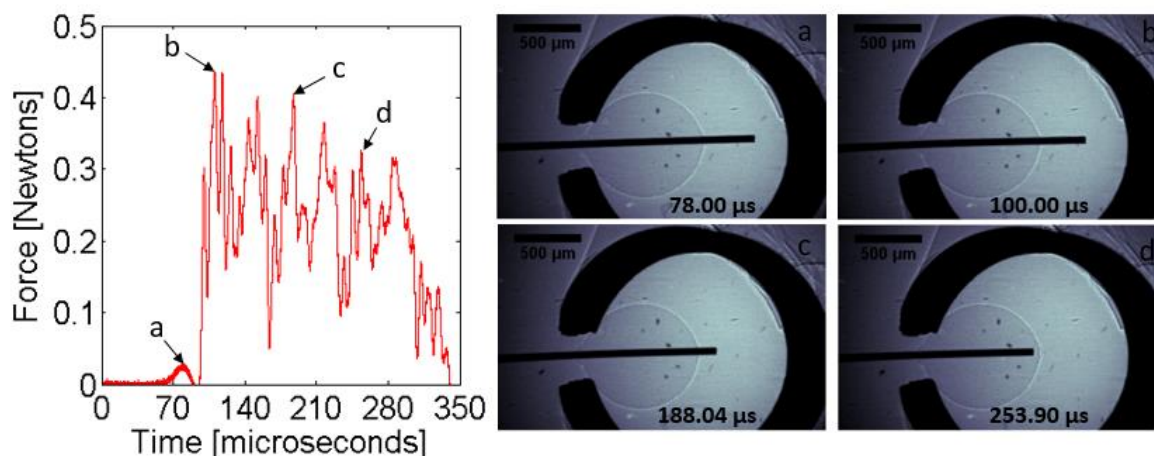


Figure 6.16. Force-time response and the corresponding pull-out image sequence of tungsten wire at 2.5 m s^{-1} with 1 million frames per second recording speed with 200 ns exposure time per frame and a $5\times$ lens.

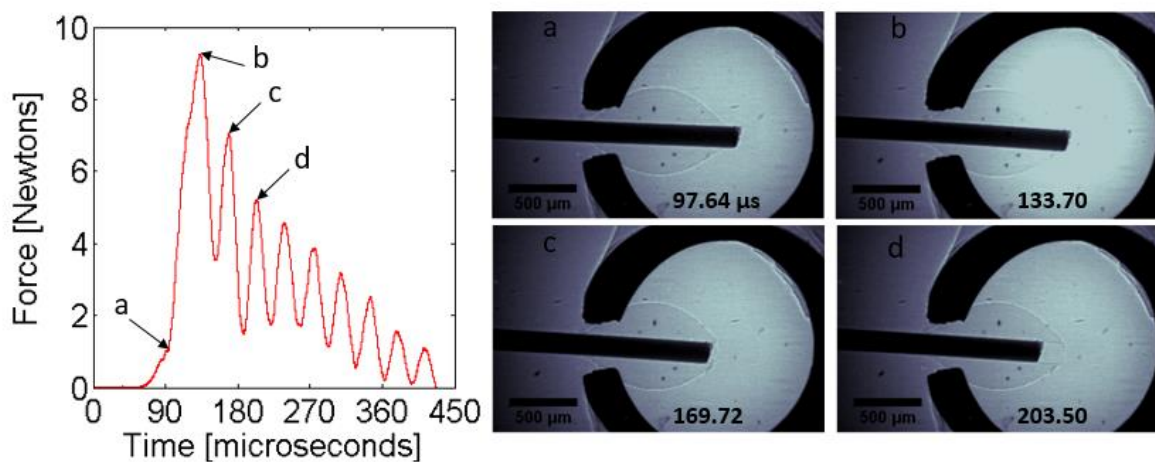


Figure 6.17. Force-time response and the corresponding pull-out image sequence of steel wire at 2.5 m s^{-1} with 1 million frames per second recording speed with 200 ns exposure time per frame and a $5\times$ lens.

Failure Surface of Recovered Epoxy Beads and Fiber Materials

Failure surface of recovered epoxy beads and the four fiber materials were examined using a NovaNano Scanning Electron Microscope (SEM). Two images (fiber surface and epoxy bead) per fiber material at each pull-out rate are shown in Figure 6.18. A meniscus was observed in front and behind on the epoxy beads for S-2 glass, tungsten, steel, and some Z-pin fiber materials. During sample preparation when epoxy beads are formed on the fiber surface, they conform to a cylindrical shape. Depending on the volume of the bead and the contact angle, a meniscus is unavoidable at the contact point of fiber and matrix [6, 23].

The SEM images revealed little to no damage on the bead surface caused by the bead holder and minor epoxy residue on the fiber surface for S-2 glass samples. The images of the epoxy bead from the tungsten samples indicated minor damage on the bead surface caused by the bead holder and no epoxy residue on the tungsten wire surface. On the other hand, the surface of the epoxy bead for the steel samples had apparent damage caused by the bead holder. This may be caused by the differences in the peak debonding forces obtained for tungsten (lower peak force) and steel wire (higher peak force). The damage caused by the bead holder on the bead surface may also affect the force history since the epoxy bead was deformed by the holder upon loading.

A similarity in failure behavior was discovered for S-2 glass fiber, tungsten, and steel wire samples at 5.0 m s^{-1} : a snap-back appearance of the meniscus. Snap-back behavior is defined in the following manner: the meniscus was stretched upon loading (before debonding). Then, when the debonding occurred, the stretched meniscus shrunk back (snap-back) as the fiber started to pull out of the epoxy bead. This phenomenon was also observed in the high-speed X-ray images for tungsten and steel samples (Figures 6.10 and 6.13).

The images for Z-pin samples with meniscus displayed apparent damage on the bead surface whereas those without meniscus revealed little to no apparent damage on the bead surface since the bead holder and the cylindrical bead shares a flat contacting area. Little to no epoxy residue was found on the Z-pin surface.

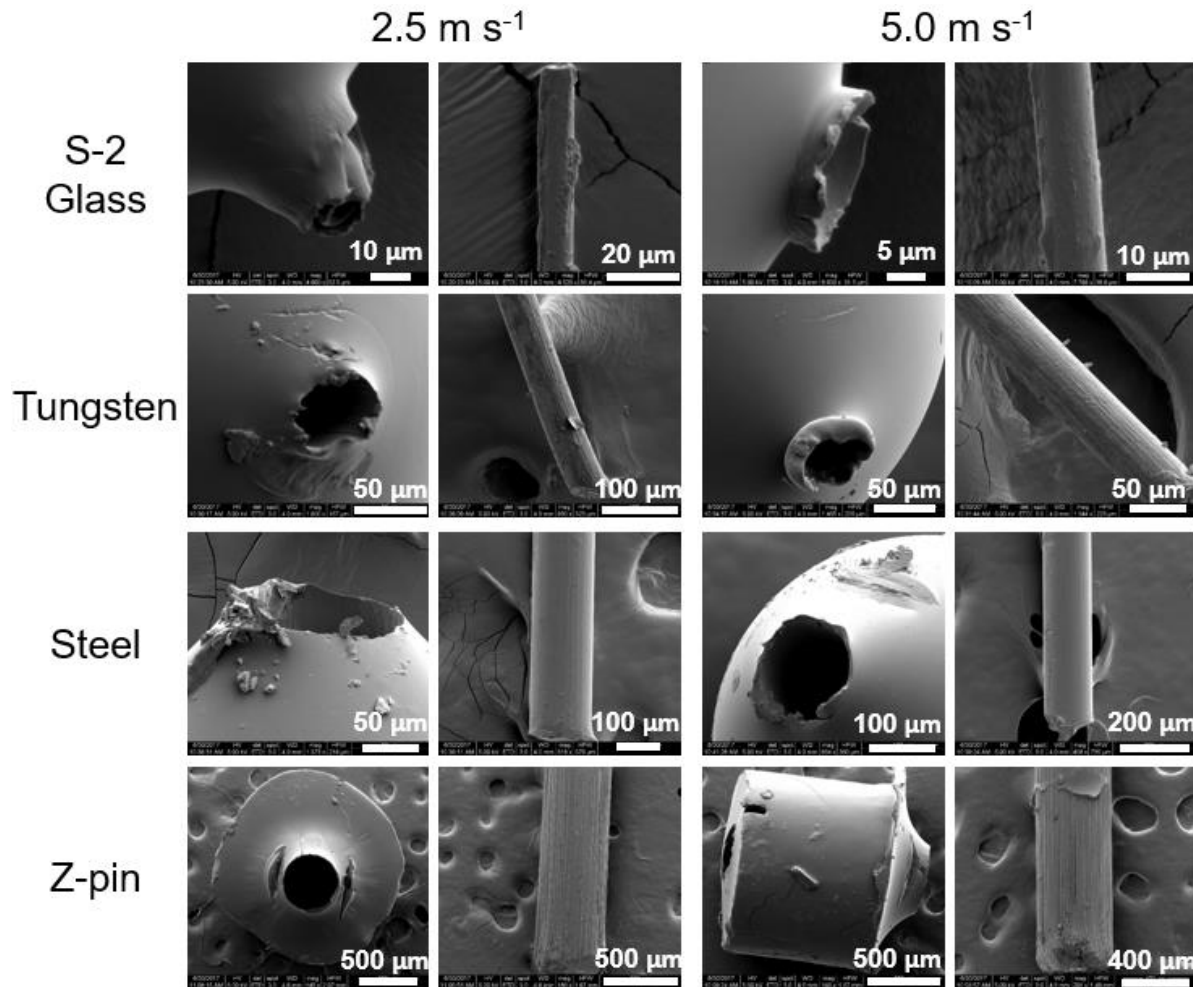


Figure 6.18. Failure surface of recovered epoxy beads and fiber materials examined via a NovaNano SEM.

6.5 Discussion

The scatter of the average peak forces and average interfacial shear stresses found in the four studied materials was speculated to be caused by: (1) non-uniform contacting angle for each experiment, (2) differences in embedded length, (3) meniscus forming around the fiber surface, (4) variation in the bead geometry and size, and (5) the non-uniformity of the fiber surface and embedded stainless steel particles [24-27]. Although the bead size for Z-pin should be more uniform compared to the other three studied fiber materials, the meniscus forming around the pin in some samples could be the cause of the large scatter in the average peak force and average

interfacial shear stress. Furthermore, even though Z-pin samples revealed the highest average peak debonding force among the four materials, the interfacial shear stress was similar to that of S-2 glass fiber samples. The maximum and minimum coefficients of variation of average peak force and average interfacial shear stress among the studied reinforcement were 60% in steel samples and 30% in Z-pin samples at 2.5 m s^{-1} .

Two debonding mechanisms were observed in the current study: catastrophic and stick-slip debonding. The difference in debonding mechanisms could be caused by: (1) the texture of the fiber surface, (2) the size of the fiber material, (3) and the size of the epoxy bead. There is an order of magnitude difference observed between samples sizes, thus, it is likely that different mechanisms may be operative at different fiber sizes. Furthermore, a smaller size of the fiber could also be less likely to have critical defects on the fiber surface and thus be stronger. Further investigation would need to be performed to justify the listed reasons for the difference in debonding mechanisms.

To rigorously analyze rate dependency of the peak debonding force and interfacial shear stress, statistical hypothesis tests (t-tests) were performed. The Anderson-Darling normality test was first performed to examine the normality of the experimental results in order to proceed with the t-test. At the 0.05 level, it was concluded that the majority of the results was significantly drawn from a normally distributed population (Table 6.2). In other words, if the p-value was greater than 0.05, the result was normally distributed. Thus, t-tests were conducted for the peak debonding forces and interfacial shear stresses for all studied fiber materials at 2.5 and 5.0 m s^{-1} . At the 0.05 level, it was concluded that except for the peak debonding force of S-2 glass, the other properties of all studied fiber materials resulted in no significant difference with increasing pull-out velocities. Thus, the peak debonding forces and interfacial shear stresses for tungsten, steel, and Z-pin fiber materials are rate insensitive when increasing the velocity from 2.5 to 5.0 m s^{-1} . Only the peak force for S-2 glass fiber revealed a statistical difference when increasing the velocity. Such a phenomenon could be due to the variation in embedded length of S-2 glass samples.

The Anderson-Darling normality test and t-tests were also performed to examine the statistical significance of the inclusion of stainless steel microspheres for tungsten and steel

samples (at 2.5 m s^{-1}). The results showed that there is no statistical difference in both the peak debonding force and interfacial shear stress for tungsten samples between epoxy beads with and without stainless steel microspheres. However, there is statistical difference in the peak debonding force and no statistical difference in interfacial shear stress for steel samples. Thus, even though different debonding mechanisms were observed between the tungsten and steel samples with and without embedded stainless steel particles, the interfacial shear stresses reveal no significant difference.

Table 6.2. P-values from the Anderson-Darling normality test.

	Peak Force	IFSS
S-2 glass (2.5 m s^{-1})	0.59	0.11
S-2 glass (5.0 m s^{-1})	0.46	0.05
Tungsten (2.5 m s^{-1})	0.94	0.97
Tungsten (5.0 m s^{-1})	0.85	0.23
Tungsten (2.5 m s^{-1} -no particle)	0.54	0.58
Steel (2.5 m s^{-1})	0.21	0.15
Steel (5.0 m s^{-1})	0.02	0.12
Steel (2.5 m s^{-1} -no particle)	0.52	0.45
Z-pin (2.5 m s^{-1})	0.39	0.39
Z-pin (5.0 m s^{-1})	0.01	0.01

Even though the force history obtained in the current study was similar to those obtained by Tamrakar *et al.*, the interfacial shear stress was far lower than the reported values [9]. Tamrakar *et al.* obtained an interfacial shear stress of 80.6 MPa at 1 m s^{-1} with the embedded length ranging from 80 to 120 μm and determined that the interfacial shear stress of S-2 glass fiber was rate sensitive [9]. Thus, such a difference in the interfacial shear stress may be caused by the differences in embedded length, coating on the fiber surface, bead holder contacting angle, the type of the epoxy resin used, and the size of the epoxy bead. This indicates that the interfacial strength in a composite can be very different even though the materials involved are nominally the same. In the current study, even though a wide range of diameters of reinforcements was studied,

the pull-out behavior of individual reinforcements was observed. Thus, size effect was not considered in this study.

Furthermore, even though the average interfacial shear stress increased with increasing pull-out velocity, there is no statistical difference in interfacial shear stress for all studied materials, thus displaying rate insensitivity in the velocity range studied. However, if the range of the velocity widens, rate effects may be more apparent [9]. A stick-slip debonding mechanism was also observed in the study of on stainless steel wire of 150 μm diameter with epoxy resin MY 750 and hardener HY 951 conducted by Takaku *et al.* [28].

6.6 Conclusions

S-2 glass, tungsten, steel, and carbon composite Z-pin reinforcements with SC-15 epoxy beads were used to study the interfacial debonding behavior in shear under fiber pull-out velocities of 2.5 and 5.0 m s^{-1} . S-2 glass fibers and Z-pins displayed catastrophic debonding whereas tungsten and steel wires displayed both catastrophic and stick-slip debonding.

Due to the larger diameter for tungsten wire, steel wire, and Z-pin samples, crack initiation and propagation were more apparent in high-speed images compared to the S-2 glass fiber samples. High-speed images of the Z-pin debonding event revealed that the crack initiated from the contacting area between the bead and the bead holder leading to more crack formation around the neck of the pin. High-speed X-ray images of the tungsten and steel debonding event demonstrated that the crack initiated from the interface on the front end of the epoxy bead (the meniscus region). Even though the average peak debonding forces and interfacial shear stresses (IFSS) increased for S-2 glass fiber and Z-pin samples and decreased for tungsten and steel wire samples with increasing pull-out velocity, there is no statistical difference in both properties with increasing pull-out velocity for all studied fiber materials except for the peak debonding force for S-2 glass fiber samples. Moreover, from the high-speed X-ray images, the interfacial debonding mechanisms for all studied fiber materials at both 2.5 and 5.0 m s^{-1} were similar. Thus, the interfacial debonding behavior was concluded to be rate insensitive as the pull-out velocity doubled from 2.5 to 5.0 m s^{-1} .

From the SEM images, the surface of the epoxy beads for steel and Z-pin samples revealed apparent damage caused by the bead holders whereas those of the S-2 glass and tungsten reveal little to no damage on the epoxy bead surface. Furthermore, the recovered beads for S-2 glass fiber, tungsten, and steel wire samples at 5.0 m s^{-1} revealed a snap-back behavior around the meniscus region.

6.7 Acknowledgements

This research was partially sponsored by the Army Research Laboratory and was accomplished under Cooperative Agreement Number W911NF-12-2-0022. The views and conclusions contained in this document are those of the authors and should not be interpreted as representing the official policies, either expressed or implied, of the Army Research Laboratory or the U.S. Government. The U.S. Government is authorized to reproduce and distribute reprints for Government purposes notwithstanding any copyright notation herein. The authors thank insightful discussions with University of Delaware researchers. The authors also thank Brady Aydelotte from Army Research Laboratory for his insightful and professional input in this research. Lastly, the authors thank Alex Deriy from Argonne National Lab's APS for his professional help during our beam time. This research used resources of the Advanced Photon Source, a U.S. Department of Energy (DOE) Office of Science User Facility operated for the DOE Office of Science by Argonne National Laboratory under Contract No. DE-AC02-06CH11357.

6.8 Conflicts of Interest

No conflict of interest exists in this article.

6.9 References

- [1] Broutman L. (1969). Measurement of the fiber-polymer matrix interfacial strength, In Interfaces in composites, ASTM International.
- [2] Mandell JF, Chen JF, and McGarry FH. (1980). A microdebonding test for in-situ fiber-matrix bond strength and moisture effects. (No. MIT/RR-R80-1). Massachusetts Inst of Tech Cambridge Dept of Materials Science and Engineering.

- [3] Miller B, Muri P, and Rebenfeld L. (1987) A microbond method for determination of the shear strength of a fiber/resin interface, *Composites Science and Technology* 28.1: 17-32.
- [4] Kelly A and Tyson WR (1965) Tensile properties of fibre-reinforced metals: copper/tungsten and copper/molybdenum, *Journal of the Mechanics and Physics of Solids*, 13(6): 329-338.
- [5] Gao X (2006) Tailored interphase structure for improved strength and energy absorption of composites.
- [6] Herrera-Franco PJ and Drzal LT (1992) Comparison of methods for the measurement of fibre/matrix adhesion in composites, *Composites*, 23.1: 2-27.
- [7] Yang L and Thomason JL (2010) Interface strength in glass fibre–polypropylene measured using the fibre pull-out and microbond methods, *Composites Part A: Applied Science and Manufacturing* 41.9: 1077-1083.
- [8] Hudspeth M, Claus B, Dubelman S, Black J, Mondal A, Parab N, Funnell C, Hai F, Qi ML, Fezzaa K, Luo SN (2013) High speed synchrotron X-ray phase contrast imaging of dynamic material response to split Hopkinson bar loading, *Review of Scientific Instruments* 84, no. 2: 025102.
- [9] Tamrakar S, Haque BZ, Gillespie JW. (2016) High rate test method for fiber-matrix interface characterization, *Polymer Testing*, 52:174-83.
- [10] Li Z, Bi X, Lambros J, Geubelle PH (2002) Dynamic fiber debonding and frictional push-out in mode composite systems: experimental observations, *Experimental mechanics*, 42(4):417-25.
- [11] Tanoglu M, McKnight SH, Palmese GR, Gillespie Jr JW (2001) The effects of glass-fiber sizings on the strength and energy absorption of the fiber/matrix interphase under high loading rates, *Composites science and technology*, 61(2):205-20.
- [12] Tanoglu M, McKnight SH, Palmese GR, Gillespie JW (2000) A new technique to characterize the fiber/matrix interphase properties under high strain rates. *Composites Part A: Applied Science and Manufacturing*, 31(10):1127-38.
- [13] Greenfield MJ, Pedicini A, Penn LS. (2000) Development of a single fiber fragmentation test for high strain rates. *International journal of adhesion and adhesives*, (5):403-7.

- [14] Parab ND, Guo Z, Hudspeth M, Claus B, Lim BH, Sun T, Xiao X, Fezzaa K, Chen WW (2017) In situ observation of fracture processes in high-strength concretes and limestone using high-speed X-ray phase-contrast imaging, *Phil. Trans. R. Soc. A.*, 375(2085):20160178.
- [15] Dransfield K, Baillie C, Mai YW (1994) Improving the delamination resistance of CFRP by stitching—a review. *Composites Science and Technology*, 50(3):305-17.
- [16] Ashton T, Negre P, Langer J (2001) Interlaminar Damage Resistance of Z fiber™ Reinforced Structural CFRP, *Extended Abstracts of the 13th International Conference on Composite Materials*.
- [17] Parab ND, Roberts ZA, Harr MH, Mares JO, Casey AD, Gunduz IE, Hudspeth M, Claus B, Sun T, Fezzaa K, Son SF (2016) High speed X-ray phase contrast imaging of energetic composites under dynamic compression, *Applied Physics Letters*, 109(13):131903.
- [18] Levine S, Nie Y, Chen W (2016) Dynamic Transverse Debonding of a Single Fiber. *Journal of Dynamic Behavior of Materials*, 2(4):521-31.
- [19] Hudspeth M, Claus B, Parab N, Lim B, Chen W, Sun T, Fezza K (2015) In situ visual observation of fracture processes in several high-performance fibers, *Journal of Dynamic Behavior of Materials*, 1(1):55-64.
- [20] Parab ND, Black JT, Claus B, Hudspeth M, Sun J, Fezzaa K, Chen WW (2014) Observation of Crack Propagation in Glass Using X- ray Phase Contrast Imaging, *International Journal of Applied Glass Science*, 5(4):363-73.
- [21] Parab ND, Claus B, Hudspeth MC, Black JT, Mondal A, Sun J, Fezzaa K, Xiao X, Luo SN, Chen W (2014) Experimental assessment of fracture of individual sand particles at different loading rates, *International Journal of Impact Engineering*, 8-14.
- [22] Schneider CA, Rasband WS, Eliceiri KW (2012) NIH Image to ImageJ: 25 years of image analysis, *Nature methods*, 9(7):671-5.
- [23] Carroll BJ (1986) Equilibrium conformations of liquid drops on thin cylinders under forces of capillarity. A theory for the roll-up process, *Langmuir*, 2(2):248-50.
- [24] Miller B, Gaur U, Hirt DE (1991) Measurement and mechanical aspects of the microbond pull-out technique for obtaining fiber/resin interfacial shear strength, *Composites science and technology*, 42(1-3):207-19.

- [25] Gaur U, Miller B (1989) Microbond method for determination of the shear strength of a fiber/resin interface: evaluation of experimental parameters, *Composites science and technology*, 34(1):35-51.
- [26] Cen H, Kang Y, Lei Z, Qin Q, Qiu W (2006) Micromechanics analysis of Kevlar-29 aramid fiber and epoxy resin microdroplet composite by Micro-Raman spectroscopy, *Composite structures*, 75(1):532-8.
- [27] Zhi C, Long H, Miao M (2017) Influence of microbond test parameters on interfacial shear strength of fiber reinforced polymer-matrix composites, *Composites Part A: Applied Science and Manufacturing*, 100:55-63.
- [28] Takaku A, Arridge RG (1973) The effect of interfacial radial and shear stress on fibre pull-out in composite materials, *Journal of Physics D: Applied Physics*, 6(17):2038.

CHAPTER 7. CONCLUSIONS

The rate effects on the fiber/matrix interfacial transverse debonding behavior was studied at loading velocities of 0.25 mm/s and 2.5 m/s. Cruciform shaped specimens were manufactured with SC-15 epoxy matrix system and various single fiber reinforcements including, S-2 glass fiber, KM2 fiber, and tungsten wire. A high-speed synchrotron X-ray phase contrast imaging technique along with a high-speed camera was used for dynamic loading condition. On the other hand, a high-speed camera with a laser back-light was used for both quasi-static experiments and dynamic experiments. Two imaging views were used to observe the debonding/failure mechanisms: high-speed imaging and SEM imaging.

The average peak debonding force, the average debonding crack velocity, and the crack geometry were measured and tracked. The average debonding force increased by 81% and the average crack velocity increased by 16% with increasing velocity for S-2 glass fiber reinforced cruciform specimens. The average debonding force increased by 119% and the average crack velocity increased by 11% with increasing velocity for KM2 fiber reinforced cruciform specimens. Finally, the average debonding force increased by 66% and the average crack velocity increased by 8% with increasing velocity for tungsten fiber reinforced cruciform specimens. For the peak debonding force, significant differences were found for all three types of fiber reinforced specimens with increasing loading velocity. For the crack velocity, significant differences were found for S-2 glass and KM2 fiber reinforced cruciform specimens and no significant difference for tungsten fiber reinforced specimens.

The force-displacement histories for all three types of reinforced cruciform specimens revealed different slopes for the quasi-static and dynamic loading conditions. For quasi-static loading, the force-displacement response for the cruciform specimens revealed to be more ductile compared to those of the dynamic loading condition. The rate dependence of epoxy failure patterns was observed through the SEM imaging of the recovered cruciform specimens.

The crack length increased linearly with time. In other words, the crack velocity remained constant within the first 2.0 μ s. The crack length for both quasi-static and dynamic loading

conditions started with similar crack length. However, as time progressed, the crack length for dynamic loading condition exceeded that of the quasi-static loading condition resulting the minor increase in the crack velocities between the two loading conditions. The crack opening velocities at dynamic loading was higher than those at quasi-static loading.

Besides the rate dependence of matrix failure patterns, the SEM images of the failure surface of recovered cruciform specimens also revealed horizontal patterns on the debonding crack initiation region whereas angled patterns were observed as the crack developed indicating the difference in crack velocity along the fiber/matrix interface and the free surface of the matrix. It was observed that the interfacial crack velocity is lower than the matrix surface crack velocity.

For the pull-out experiments, S-2 glass, tungsten, steel, and carbon composite Z-pin reinforcements with SC-15 epoxy beads were used to study the interfacial shear debonding behavior at loading velocities of 2.5 and 5.0 m/s. S-2 glass fibers and Z-pins revealed catastrophic debonding whereas tungsten and steel wires displayed both catastrophic and stick-slip debonding.

Both metal wires and carbon composite Z-pin specimens revealed apparent debonding initiation (around the contacting area between the epoxy bead and the bead holder) and progression in high-speed images compared to the S-2 glass fiber samples due to their larger in diameters. Even though the average peak debonding forces and interfacial shear stresses (IFSS) increased for S-2 glass fiber and carbon composite Z-pin samples and decreased for tungsten and steel wire specimens with increasing pull-out velocity, there is no statistical difference in both properties with increasing pull-out velocity for all studied fiber materials except for the peak debonding force for S-2 glass fiber specimens. Thus, the interfacial debonding behavior was concluded to be rate insensitive as the pull-out velocity increased from 2.5 to 5.0 m/s.

Lastly, from the SEM images, the surface of the epoxy beads for steel and carbon composite Z-pin specimens revealed damage caused by the bead holders upon loading whereas those of the S-2 glass and tungsten reveal little to no damage on the epoxy bead surface. Furthermore, the recovered beads for S-2 glass fiber, tungsten, and steel wire samples at 5.0 m s⁻¹ revealed a snap-back behavior around the meniscus region.

CHAPTER 8. FUTURE WORK

In the current study, we investigated the fiber/matrix interfacial transverse debonding behavior under both quasi-static and dynamic loading conditions in two view-points (Figure 8.1): the high-speed imaging view and the SEM imaging view. From the high-speed imaging view, we observed debonding crack initiation and progression leading to material failure. Using the high-speed synchrotron X-ray, we were able to see through the opaque matrix system to observe the embedded fiber/matrix debonding. For the SEM imaging view, we observed the cross-section view along the fiber length and discovered the crack velocity difference along the fiber/matrix interface and the matrix surface. With the observations discovered in the current study, we found that the potential for future studies and analysis of the topic include: 1. The cross-section view across the fiber diameter, 2. Interfacial stress analysis and fracture mechanics, 3. Curing and post-curing effect of the debonding mechanisms, and 4. Mixed-mode/multi-fiber/toughened epoxy cruciform experiments. The following subsections discuss the preliminary ideas for these potential future studies.

8.1 Cross-Section View of the Cruciform Specimen Across the Fiber Diameter

The cruciform specimen can be better analyzed if it can be presented in an additional view-point: cross-section across the fiber diameter view. The cross-section across the fiber diameter view is desired to observe the sequence of the failure modes (e.g. crack initiation at 90- and 270-degree points or debonding initiation at 0- and 180-degree points). A challenge to observe the cross-section view across the fiber diameter would be the specimen preparation. To observe a 10- μm diameter fiber embedded in epoxy, the surfaces of the cross-section must be polished to a mirrored finish or must have a clean and precise cut. Furthermore, determining the specimen thickness is another concern. The specimen thickness must be able to represent the debonding behavior of the cross-section of the fiber diameter of the actual cruciform specimen. If not, the observation would not resemble that of the behavior in the actual cruciform specimen.

After overcoming the specimen preparation challenges, the experiments can be performed in the SEM chamber using a tensile loading device under quasi-static incremental loading. To

perform dynamic loading experiments, higher resolution of the high-speed imaging is desired to capture the failure mode sequence. With all the views available, we have the potential to precisely characterize the transverse debonding and failure mechanisms of the single fiber reinforced cruciform specimen.

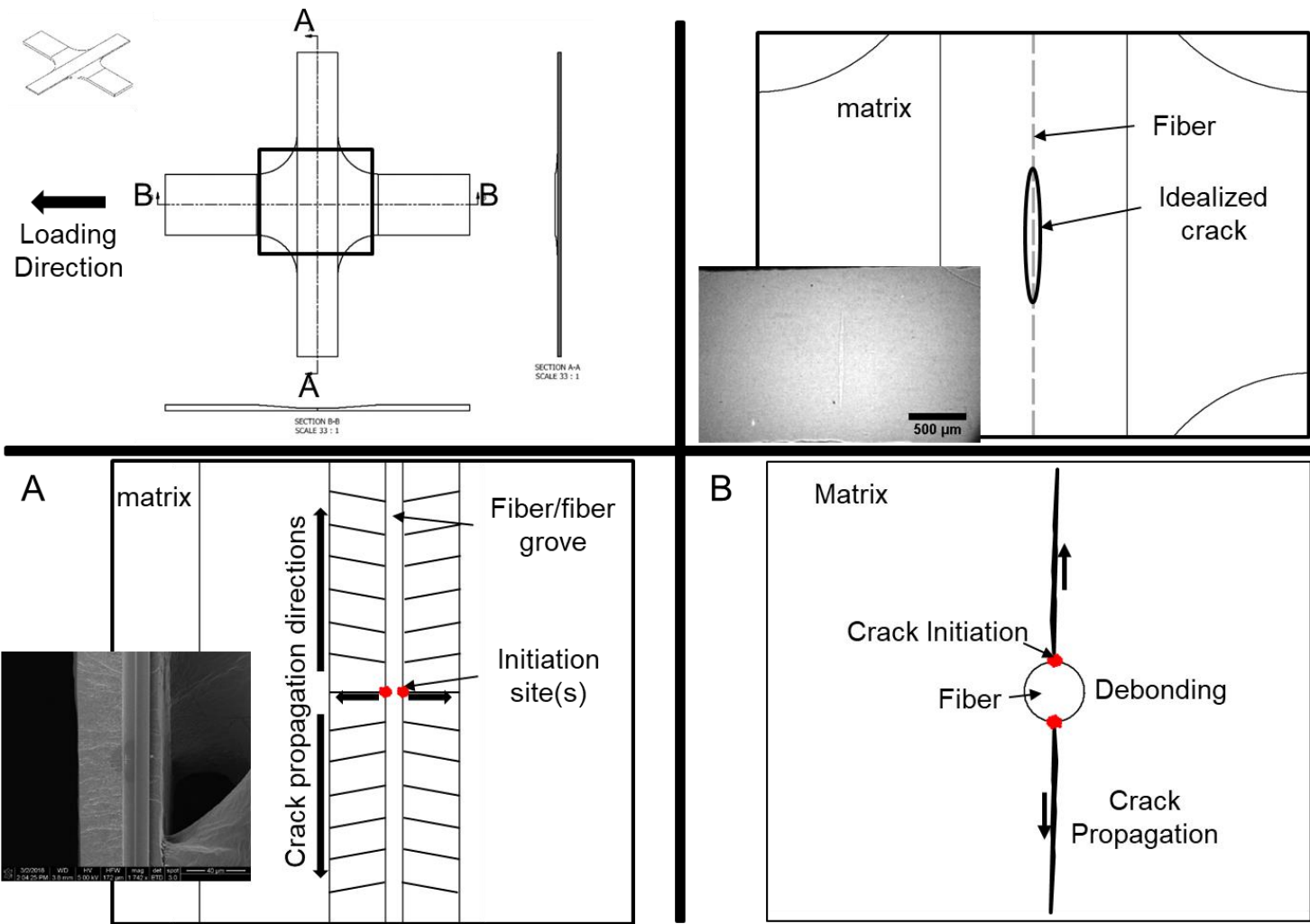


Figure 8.1. Three view-points of the cruciform specimen: (a) high-speed imaging view, (b) SEM imaging view, and (c) cross-section across the fiber diameter view

8.2 Interfacial Stress Analysis and Fracture Mechanics

With the cross-section view across the fiber diameter, interfacial stress field obtained by using a simple plate-filled hole model may be verified. Modeling the cross-section view across the fiber diameter of the cruciform specimen using a plate with a filled hole model in the elastic regime, we can derive the stress field using the Airy Function with the assumed boundary conditions. Using the boundary conditions, we can obtain the constants to obtain the Airy functions for the matrix and fiber materials. With the Airy functions, we can then derive the stress field around the fiber/matrix interface.

It is more difficult to obtain the stress intensity factor for SC-15 epoxy with various reinforcements because the SC-15 epoxy is not transparent. Thus, typical photoelasticity and caustic methods are not sufficient to measure the stress intensity factor. Digital imaging correlation has been used in the literature to obtain the displacement field and thus, the stress intensity factor, of cracks through high-speed imaging. In the transverse debonding cruciform experiments, the DIC method may be utilized to obtain the displacement field of the cruciform specimen as a whole. However, the fiber/matrix interfacial displacement may be very difficult to measure with the current cruciform experiments via the DIC method. However, if the cross-section across the fiber diameter specimens (as mentioned in the Chapter 8.1) can be manufactured, perhaps the DIC could be used in that set of experiments to obtain the displacement field around the fiber/matrix interface. From the measured displacement field, we can calculate the stress intensity factor and the strain energy release rate.

8.3 Curing and Post-Curing Effect of The Debonding Mechanisms

specimen curing and post-curing would greatly affect the result. Levine *et al.* [28] performed experiments using the specimens that were cured in room temperature for 48 hours. The experiments performed in the current study used the specimens that were cured in room temperature for 48 hours and post-cured in the furnace at 125 °C for 2 hours. The peak debonding forces obtained from both studies differed. Levine *et al.* [28] obtained an average peak debonding forces of 7.67 ± 2.97 N and 7.31 ± 2.86 N at 2.6 m/s and 0.01 mm/s, respectively. Only a 4.6%

increase was found [28]. However, for the current study, the average peak debonding forces of 12.89 ± 2.51 N and 7.11 ± 0.83 N at 2.5 m/s and 0.25 mm/s, respectively [28].

The quasi-static loadings remained a similar peak debonding force whereas the dynamic loading experienced a major increase between the post-cured specimens and non-post-cured specimens. Such a different may also affect the crack velocities and the failure mechanisms. Thus, further curing and post-curing investigations can be performed to see how they affect the debonding behaviors since the curing process is an important parameter that can alter the results significantly.

8.4 Mixed-Mode/Multi-Fiber/Toughened Epoxy Cruciform Experiments

From the literature review, researchers have utilized the cruciform geometry specimen for different study purposes such as the mix-mode experiments and the multi-fiber experiments [17, 26]. Both types of the experiments are of interest to perform under dynamic loading with in-situ visualization since the studies from the literature were performed under quasi-static loading conditions. By performing the dynamic mix-mode (tensile and shear), we can observe how the modes affect the peak debonding force, crack velocity, and crack geometry.

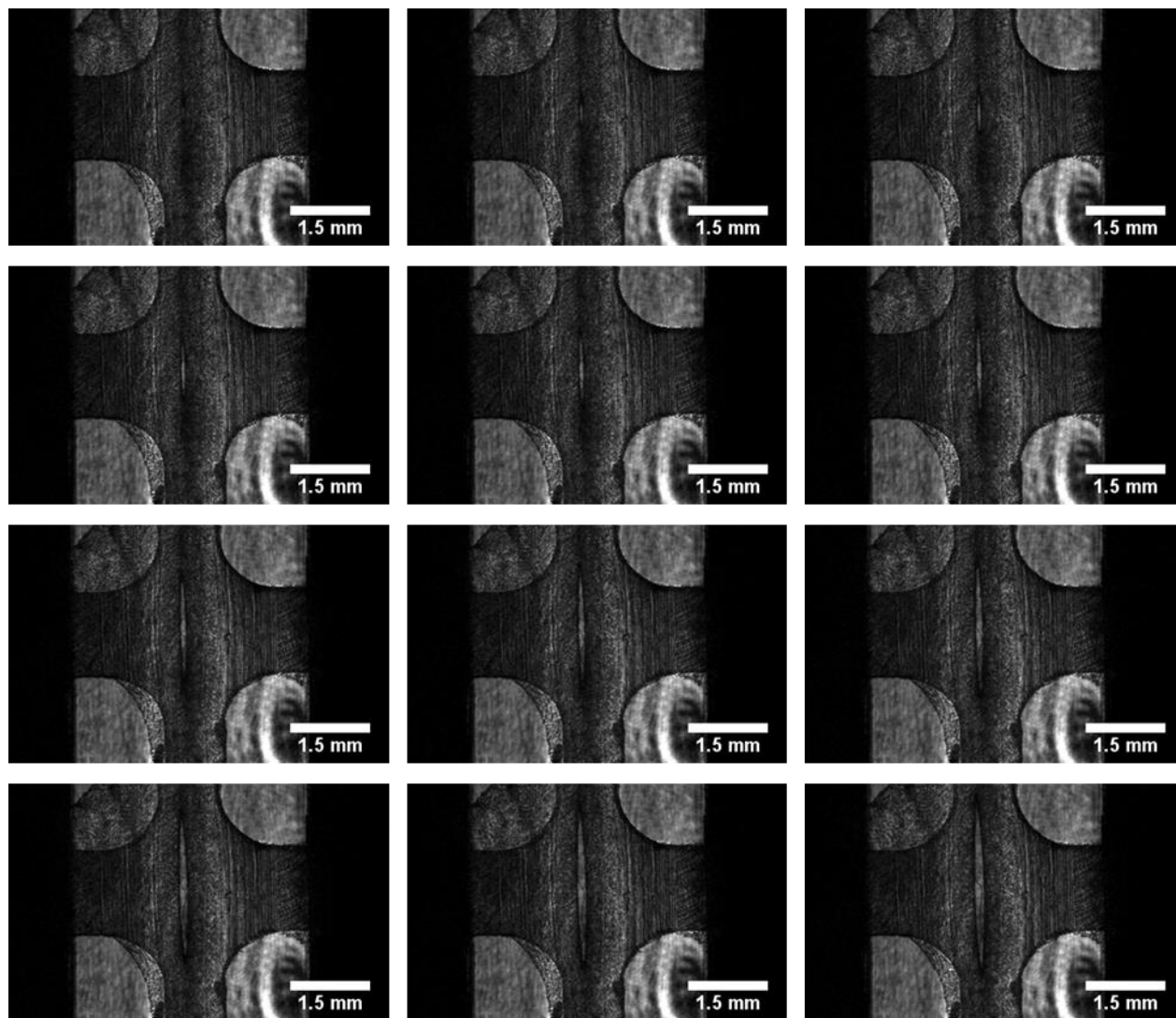
The multi-fiber experiments under dynamic loading conditions can also allow us to see how the fibers would interact with each other and with the surrounding matrix. Perhaps different failure modes including, fiber/matrix debonding, matrix failure, or fiber failure, can be observed with different fiber arrangements in the epoxy matrix system. The results would greatly help to construct more accurate models to predict the dynamic debonding behavior of fiber reinforced polymer composites.

Besides specimen curing, another parameter that would affect the result is the epoxy used. Drexel University has provided a toughened epoxy for us to perform experiments to study the effect of the debonding behavior between the toughened epoxy and the SC-15 epoxy. However, due to the nature of the curing process of the provided toughened epoxy, specimen preparation is a major challenge. The epoxy used was Tetraglycidyl of Diaminodiphenylmethane (TGDDM), curing agent Jeffamine Diamines D-230, and toughening additives mPRS [64]. The epoxy requires

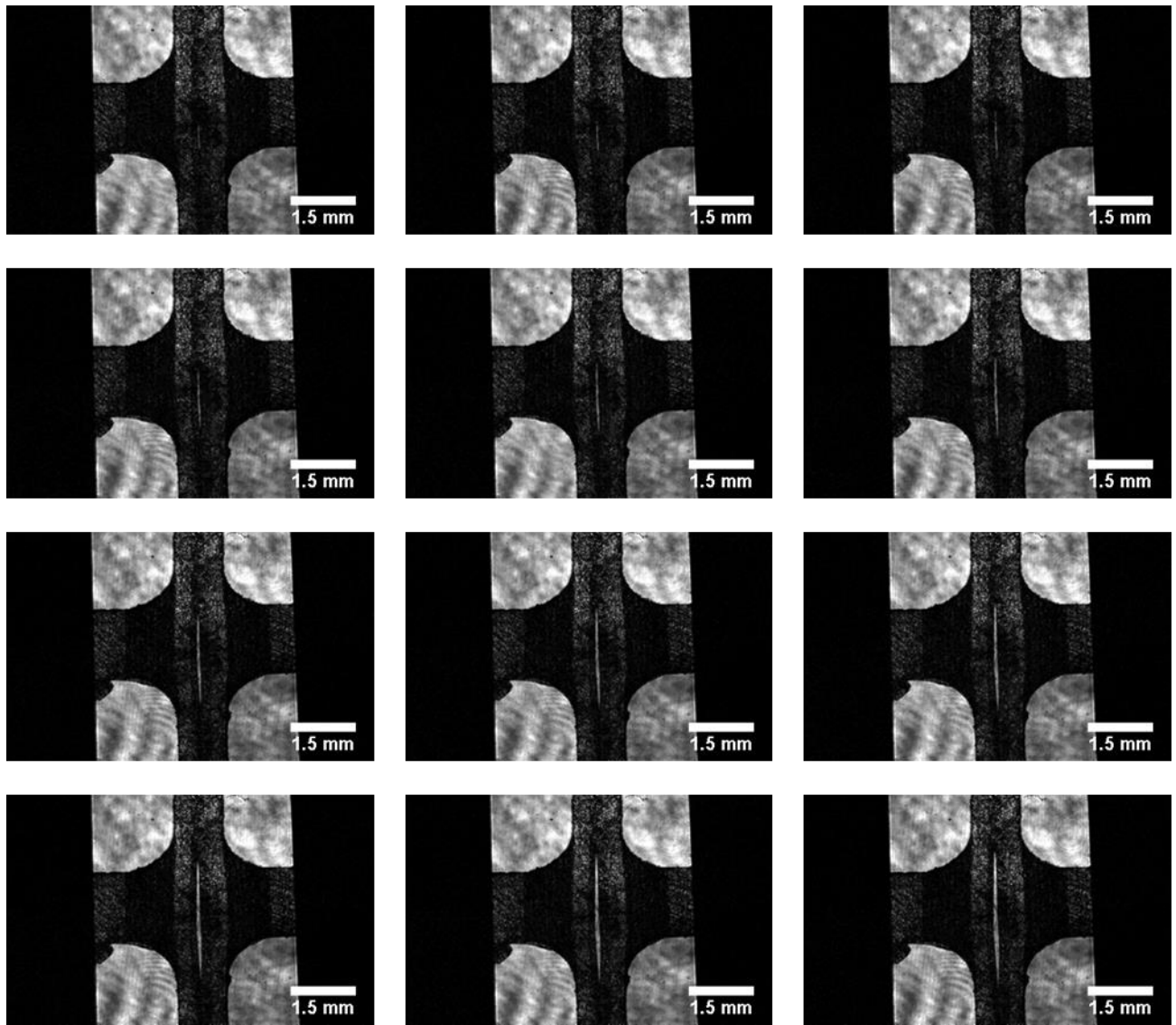
to be cured at 80 °C for 24 hours and post-cured at 160 °C for 3 hours. Using the silicone rubber mold as described in the specimen preparation section, the toughened epoxy would diffuse out from the cruciform cavities after removing from the furnace which prohibited the cruciform specimens from being produced. Thus, a modified specimen preparation procedure should be developed to successfully produce cruciform specimens from the toughened epoxy system. Then, comparison of the interfacial transverse debonding behaviors of the single fiber reinforced cruciform specimens manufactured from a toughened epoxy and the SC-15 epoxy matrix system can be performed.

APPENDIX

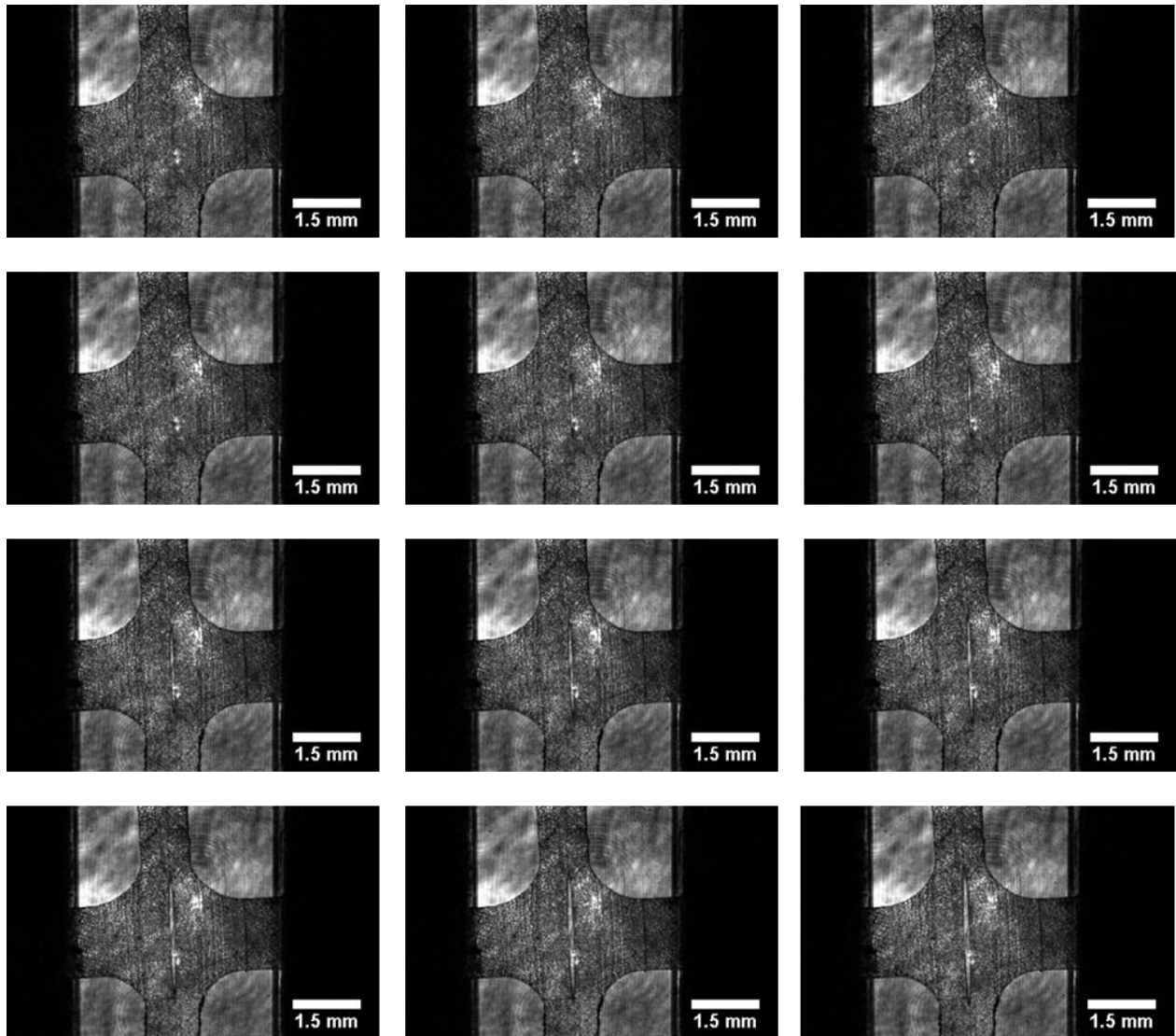
High-Speed Imaging



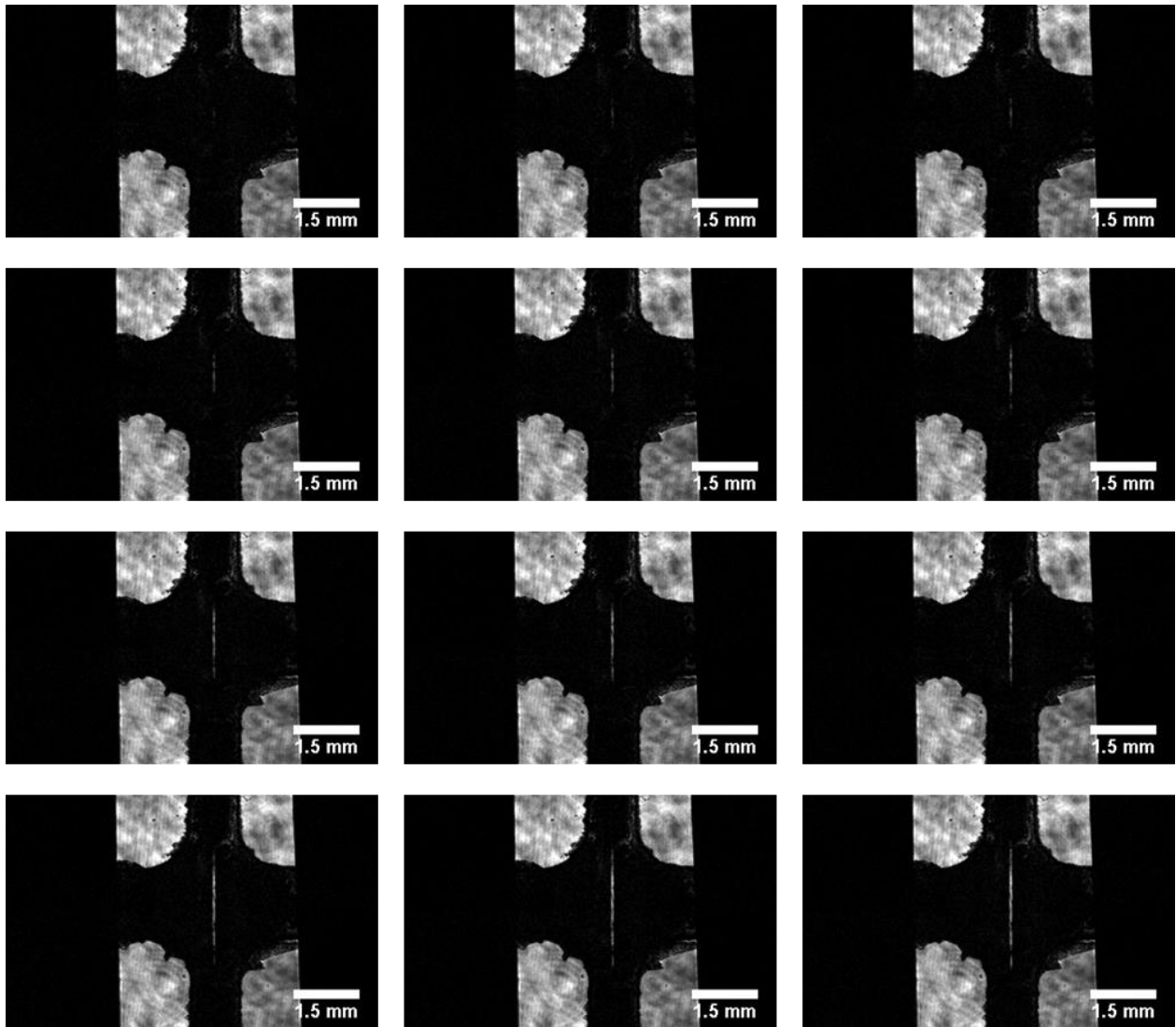
A 1. High-speed images sequence of S-2 glass reinforced specimen at 2.5 m/s.



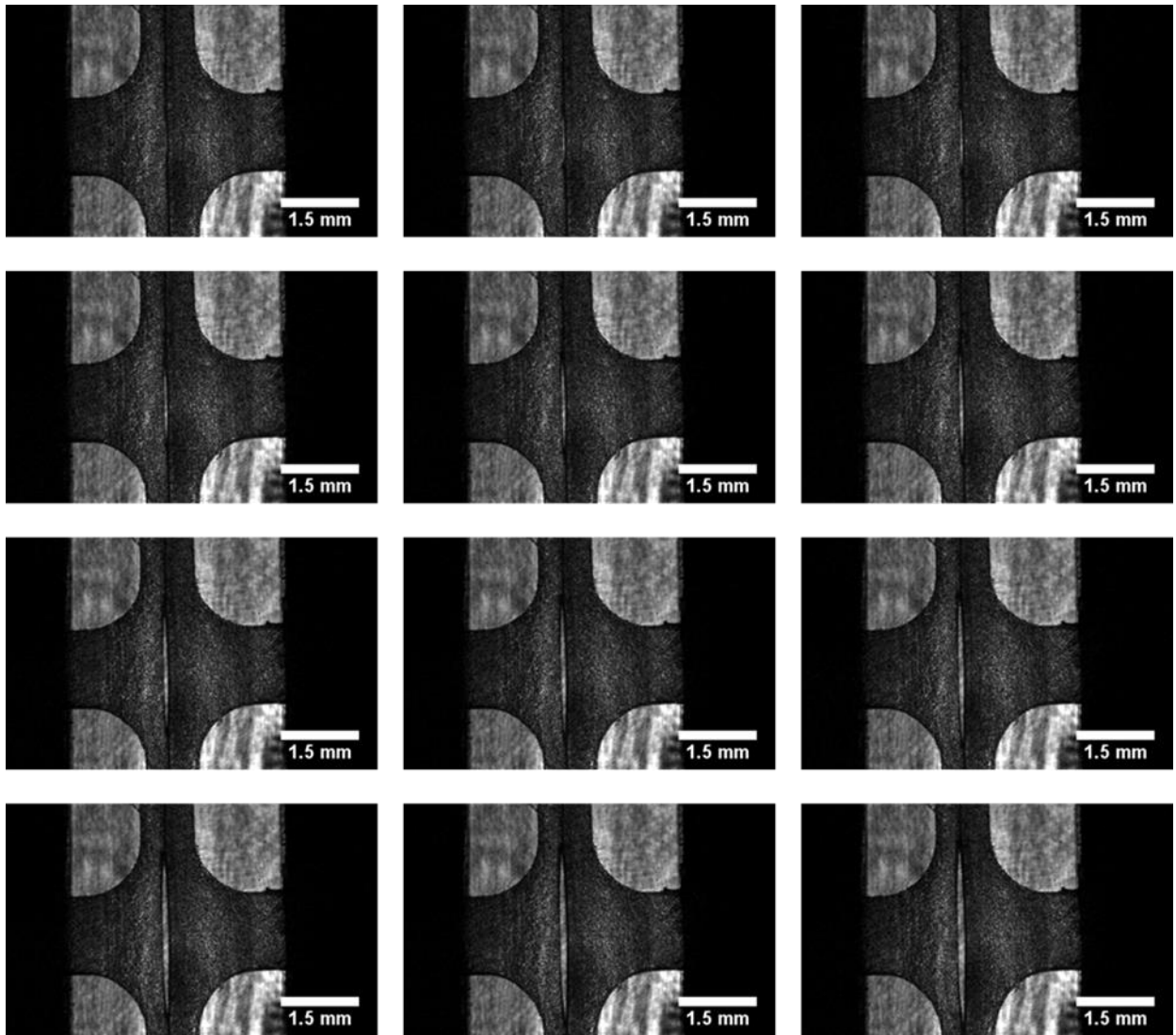
A 2. High-speed images sequence of S-2 glass reinforced specimen at 0.25 m/s.



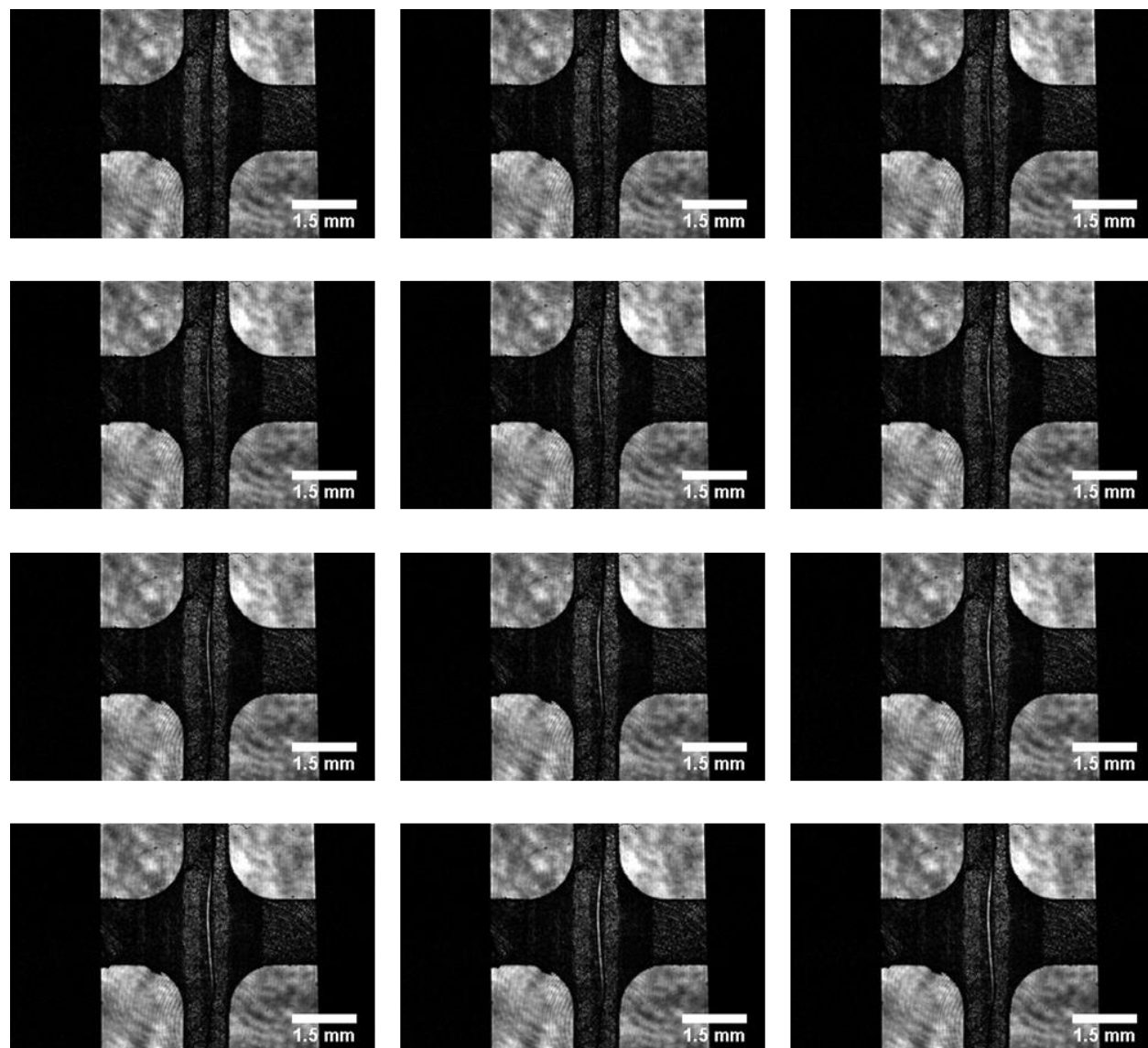
A 3. High-speed images sequence of KM2 reinforced specimen at 2.5 m/s.



A 4. High-speed images sequence of KM2 reinforced specimen at 0.25 mm/s.



A 5. High-speed images sequence of tungsten reinforced specimen at 2.5 m/s.



A 6. High-speed images sequence of tungsten reinforced specimen at 0.25 mm/s.

REFERENCES

- [1] Hale, Justin. "Boeing 787 from the ground up." *Aero* 4.24 (2006): 7.
- [2] Nithin K, Sachhidananda S (2017) Fiber Reinforced Composites - A Review. *J Material Sci Eng* 6: 341. doi: 10.4172/2169-0022.1000341
- [3] Gao X (2006) Tailored interphase structure for improved strength and energy absorption of composites.
- [4] Tamrakar S, Haque BZ, Gillespie JW. (2016) High rate test method for fiber-matrix interface characterization, *Polymer Testing*, 52:174-83.
- [5] Zhandarov, S., & Mäder, E. (2005). Characterization of fiber/matrix interface strength: applicability of different tests, approaches and parameters. *Composites Science and Technology*, 65(1), 149-160.
- [6] Gama, B. A., & Gillespie Jr, J. W. (2011). Finite element modeling of impact, damage evolution and penetration of thick-section composites. *International Journal of Impact Engineering*, 38(4), 181-197.
- [7] Xiao, J. R., Gama, B. A., & Gillespie Jr, J. W. (2007). Progressive damage and delamination in plain weave S-2 glass/SC-15 composites under quasi-static punch-shear loading. *Composite structures*, 78(2), 182-196.
- [8] Broutman L (1969) Measurement of the fiber-polymer matrix interfacial strength, In *Interfaces in composites*, ASTM International.
- [9] Hudspeth M, Claus B, Dubelman S, Black J, Mondal A, Parab N, Funnell C, Hai F, Qi ML, Fezzaa K, Luo SN (2013) High speed synchrotron X-ray phase contrast imaging of dynamic material response to split Hopkinson bar loading, *Review of Scientific Instruments* 84, no. 2: 025102.
- [10] Mandell JF, Chen JF, and McGarry FH (1980) A microdebonding test for in-situ fiber-matrix bond strength and moisture effects. (No. MIT/RR-R80-1). Massachusetts Inst of Tech Cambridge Dept of Materials Science and Engineering.
- [11] Li Z, Bi X, Lambros J, Geubelle PH (2002) Dynamic fiber debonding and frictional push-out in mode composite systems: experimental observations, *Experimental mechanics*, 42(4):417-25.

- [12] Tanoglu M, McKnight SH, Palmese GR, Gillespie JW (2000) A new technique to characterize the fiber/matrix interphase properties under high strain rates. *Composites Part A: Applied Science and Manufacturing*, 31(10):1127-38.
- [13] Miller B, Muri P, Rebenfeld L (1987) A microbond method for determination of the shear strength of a fiber/resin interface, *Composites Science and Technology* 28.1: 17-32.
- [14] Kelly A and Tyson WR (1965) Tensile properties of fibre-reinforced metals: copper/tungsten and copper/molybdenum, *Journal of the Mechanics and Physics of Solids*, 13(6): 329-339-338-3350.
- [15] Greenfield MJ, Pedicini A, Penn LS. (2000) Development of a single fiber fragmentation test for high strain rates. *International journal of adhesion and adhesives*, (5):403-7.
- [16] Gundel, D. B., Majumdar, B. S., & Miracle, D. B. (1995). Evaluation of the transverse response of fiber-reinforced composites using a cross-shaped sample geometry. *Scripta Metallurgica et Materialia*, 33(12), 2057-2065.
- [17] Tandon, G. P., Kim, R. Y., & Bechel, V. T. (2002). Fiber–matrix interfacial failure characterization using a cruciform-shaped specimen. *Journal of composite materials*, 36(23), 2667-2691.
- [18] Herrera-Franco PJ and Drzal LT (1992) Comparison of methods for the measurement of fibre/matrix adhesion in composites, *Composites*, 23.1: 2-27.
- [19] Yang L and Thomason JL (2010) Interface strength in glass fibre–polypropylene measured using the fibre pull-out and microbond methods, *Composites Part A: Applied Science and Manufacturing* 41.9: 1077-1083.
- [20] Tsai, K. H., & Kim, K. S. (1996). The micromechanics of fiber pull-out. *Journal of the Mechanics and Physics of Solids*, 44(7), 1147-1161-1159-1177.
- [21] Zhi C, Long H, Miao M (2017) Influence of microbond test parameters on interfacial shear strength of fiber reinforced polymer-matrix composites, *Composites Part A: Applied Science and Manufacturing*, 100:55-63.
- [22] Meurs PF, Schrauwen BA, Schreurs PJ, Peijs T (1998) Determination of the interfacial normal strength using single fibre model composites. *Compos Part A* 29(9–10):1027–1034
- [23] Hu, S., Karpur, P., Matikas, T. E., Shaw, L., & Pagano, N. J. (1995). Free edge effect on residual stresses and debond of a composite fibre/matrix interface. *Mechanics of Composite Materials and Structures. An International Journal*, 2(3), 215-225.

- [24] Gundel, D.B. and Miracle, D.B., 1998. The influence of interface structure and composition on the response of single-fiber SiC/Ti-6Al-4V composites to transverse tension. *Applied Composite Materials*, 5(2), pp.95-108.
- [25] Gundel, D.B., Warrior, S.G. and Miracle, D.B., 1999. The transverse tensile behavior of SiC-fiber/Ti-6Al-4V composites 2. Stress distribution and interface failure. *Composites science and technology*, 59(7), pp.1087-1096.
- [26] Foster, D. C., Tandon, G. P., & Zoghi, M. (2006). Evaluation of failure behavior of transversely loaded unidirectional model composites. *Experimental mechanics*, 46(2), 217-243.
- [27] Li, Z., Ghosh, S., Getinet, N., & O'Brien, D. J. (2016). Micromechanical modeling and characterization of damage evolution in glass fiber epoxy matrix composites. *Mechanics of materials*, 99, 37-52.
- [28] Levine S, Nie Y, Chen W (2016) Dynamic Transverse Debonding of a Single Fiber. *Journal of Dynamic Behavior of Materials*, 2(4):521-31.
- [29] Tabiaï, I., Delorme, R., Therriault, D., & Levesque, M. (2018). In-situ Full Field Measurements During Inter-Facial Debonding in Single Fiber Composite Under Transverse Load. *Experimental Mechanics*, 58(9), 1451-1467.
- [30] Nishikawa, M., Okabe, T., Hemmi, K., & Takeda, N. (2008). Micromechanical modeling of the microbond test to quantify the interfacial properties of fiber-reinforced composites. *International Journal of Solids and Structures*, 45(14), 4098-4113.
- [31] Khanna, S.K., et al., Sample preparation techniques for nano-mechanical characterization of glass fiber reinforced polyester matrix composites. *Composites Part A: Applied Science and Manufacturing*, 2003. 34(1): p. 53-65.
- [32] Feih, S., et al., The influence of fibre sizing on the strength and fracture toughness of glass fibre composites. *Composites Part A: Applied Science and Manufacturing*, 2005. 36(2): p. 245-255
- [33] Bannister, D. J., Andrews, M. C., Cervenka, A. J., & Young, R. J. (1995). Analysis of the single-fibre pull-out test by means of Raman spectroscopy: Part II. Micromechanics of deformation for an aramid/epoxy system. *Composites science and technology*, 53(4), 411-421.

- [34] Gaur U, Miller B (1989) Microbond method for determination of the shear strength of a fiber/resin interface: evaluation of experimental parameters, *Composites science and technology*, 34(1):35-51.
- [35] DiFrancia, C., Ward, T. C., & Claus, R. O. (1996). The single-fibre pull-out test. 1: Review and interpretation. *Composites Part A: Applied Science and Manufacturing*, 27(8), 597-612.
- [36] Kim, J. K., Baillie, C., & Mai, Y. W. (1992). Interfacial debonding and fibre pull-out stresses. *Journal of materials science*, 27(12), 3143-3154.
- [37] Bowling, J., & Groves, G. W. (1979). The debonding and pull-out of ductile wires from a brittle matrix. *Journal of materials science*, 14(2), 431-442.
- [38] Cook, R. F., Thouless, M. D., Clarke, D. R., & Kroll, M. C. (1989). Stick-slip during fibre pull-out. *Scripta metallurgica*, 23(10), 1725-1730.
- [39] Ravi-Chandar, K., & Knauss, W. G. (1984). An experimental investigation into dynamic fracture: I. Crack initiation and arrest. *International Journal of Fracture*, 25(4), 247-262.
- [40] Ravi-Chandar, K., & Knauss, W. G. (1984). An experimental investigation into dynamic fracture: II. Microstructural aspects. *International Journal of Fracture*, 26(1), 65-80.
- [41] Ravi-Chandar, K., & Knauss, W. G. (1984). An experimental investigation into dynamic fracture: III. On steady-state crack propagation and crack branching. *International Journal of fracture*, 26(2), 141-154.
- [42] Ravi-Chandar, K., & Knauss, W. G. (1984). An experimental investigation into dynamic fracture: IV. On the interaction of stress waves with propagating cracks. *International Journal of Fracture*, 26(3), 189-200.
- [43] Freund, L. B. (1972). Crack propagation in an elastic solid subjected to general loading—I. Constant rate of extension. *Journal of the Mechanics and Physics of Solids*, 20(3), 129-140.
- [44] Chen, W. W., & Song, B. (2010). *Split Hopkinson (Kolsky) bar: design, testing and applications*. Springer Science & Business Media.
- [45] Claus, B., Chu, J., Beason, M., Liao, H., Martin, B., & Chen, W. (2017). Dynamic Experiments using Simultaneous Compression and Shear Loading. *Experimental Mechanics*, 57(9), 1359-1369.
- [46] Chen, W. W. (2016). Experimental methods for characterizing dynamic response of soft materials. *Journal of Dynamic Behavior of Materials*, 2(1), 2-14.

- [47] Chu JM, Claus B, Parab N, O'Brien D, Sun T, Fezzaa K, and Chen W. (2017) Visualization of dynamic fiber-matrix interfacial shear debonding. *Journal of Material Science*. 10.1007/s10853-017-1759-1.
- [48] Parab ND, Roberts ZA, Harr MH, Mares JO, Casey AD, Gunduz IE, Hudspeth M, Claus B, Sun T, Fezzaa K, Son SF (2016) High speed X-ray phase contrast imaging of energetic composites under dynamic compression, *Applied Physics Letters*, 109(13):131903.
- [49] Hudspeth M, Claus B, Parab N, Lim B, Chen W, Sun T, Fezza K (2015) In situ visual observation of fracture processes in several high-performance fibers, *Journal of Dynamic Behavior of Materials*, 1(1):55-64.
- [50] Parab ND, Claus B, Hudspeth MC, Black JT, Mondal A, Sun J, Fezzaa K, Xiao X, Luo SN, Chen W (2014) Experimental assessment of fracture of individual sand particles at different loading rates, *International Journal of Impact Engineering*, 8-14.
- [51] Wang ML, McAninch IM, and La Scala JJ. (2011) *Materials Characterization of High-Temperature Epoxy Resins: SC-79 and SC-15/SC-79 Blend*. ARL-TR-5485.
- [52] Justusson B, Yu J, Chen A, and Yen CF. (2012) *Mechanical Testing of 3D Fabric Composite and Their Matrix Materials SC-15*. ARL-TR-6245.
- [53] AGY, *Advanced Materials: Solutions for Demanding Applications*, 2004.
- [54] Guo, Z., Casem, D., Hudspeth, M., Nie, X., Sun, J., & Chen, W. (2016). Transverse compression of two high-performance ballistic fibers. *Textile Research Journal*, 86(5), 502-511.
- [55] Hudspeth, M., Li, D., Spatola, J., Chen, W., & Zheng, J. (2016). The effects of off-axis transverse deflection loading on the failure strain of various high-performance fibers. *Textile Research Journal*, 86(9), 897-910.
- [56] Tungsten. <https://www.azom.com/properties.aspx?ArticleID=614>
- [57] Jensen, R., Forster, A., Dibelka, J., and Copeland, C. (2005). *Cure Schedule Evaluation of SC15 and SC79 Low-Viscosity Epoxy VARTM Resins*. ARL-TN-249.
- [58] SC-15: Toughened Epoxy Resin System.
- [59] 933 S-2 Glass Roving. https://www.agy.com/wp-content/uploads/2014/03/933_S-2_Roving-Aerospace.pdf.

- [60] Cheng, M., Chen, W., & Weerasooriya, T. (2004). Experimental investigation of the transverse mechanical properties of a single Kevlar® KM2 fiber. *International Journal of Solids and Structures*, 41(22-23), 6215-6232.
- [61] Kevlar® Aramid Fiber Technical Guide. DuPont.
- [62] Purslow, D. (1986). Matrix fractography of fibre-reinforced epoxy composites. *Composites*, 17(4), 289-303.
- [63] Hudspeth, M., Chu, J. M., Jewell, E., Lim, B., Ytuarte, E., Tsutsui, W., ... & Chen, W. (2017). Effect of projectile nose geometry on the critical velocity and failure of yarn subjected to transverse impact. *Textile Research Journal*, 87(8), 953-972.
- [64] Gao J. (2017). ComPro 3: Synthesis of Epoxy Networks and Interphases with Controlled Topology. MEDE Fall Meeting.

VITA

Education

- Doctor of Philosophy in Aeronautics and Astronautics** December 2018
 Purdue University, West Lafayette, IN GPA: 3.9/4.0
 Concentrations: Structures, Materials, and Systems
- Master of Science in Aeronautics and Astronautics** May 2016
 Purdue University, West Lafayette, IN GPA: 3.6/4.0
 Concentrations: Structures and Materials
 Master Thesis: Mechanical Properties of Transgenic Silkworm Silk at High Rate Impact
- Bachelor of Science in Aeronautics and Astronautics** June 2014
 National Cheng Kung University, Tainan, Taiwan GPA: 3.6/4.0
 Concentration: Structures

Skills

Software: MATLAB, Abaqus, Inventor, AutoCAD, CATIA, SolidWorks, Minitab, Mathematica, OriginPro, ImageJ, Microsoft Office

Laboratory Instrument: Kolsky bars, gas/powder guns, MTS, Electron Microscopy, high-speed camera

Professional Experience

Research

- Graduate Research Assistant, Purdue University August 2014 - Present
 -High-Speed Synchrotron X-ray Imaging, *funded by MEDE, US Army Research Laboratory*
- Designed experimental techniques to visualize the fiber/matrix interfacial failure under high rate impact at Advanced Photo Source, Argonne National Laboratory, to improve the ballistic protection system
 - Collected high-speed images using a Phase Contrast Imaging technique to visualize and pinpoint the fiber/matrix debonding event
 - Evaluated fracture parameters by synchronizing high-speed images and the force history via MATLAB and ImageJ
 - Determined the crack velocity and the stress field of single fiber composite upon dynamic loading to identify the failure mechanisms

-Characterization of High-Performance Fibers & Transgenic Silkworm Silk, *funded by US Army PEO Soldiers*

- Conducted low and high strain rate experiments on transgenic silkworm silk and high-performance fibers using an MTS and a modified tension Kolsky bar to investigate the rate effect of the fibers
- Analyzed the material response of various fiber textiles to determine the feasibility for ballistic armor system applications
- Designed gripping methods for tensile loading experiments for acquiring material response for various polymer fiber textiles.
- Tracked the geometry and microstructure of the fiber materials using Electron Microscopy (SEM, TEM) to determine the material behavior and failure mechanisms in detail

-Construction of the Modified Torsion Kolsky Bar

- Participated in building the modified torsion Kolsky bar to implement the dynamic response of materials undergoing complicated stress states

-Post-Mortem Analysis on Different Materials under Various Loading Conditions

- Investigated the failure surface of the recovered textile materials via a SEM to pinpoint the root cause of the textile failure upon impact
- Analyzed the failure surface of the recovered single fiber-matrix composite interface (surface cracks and patterns) to specify the material failure mode

Professional Affiliations

American Society for Composites (ASC), Society for Experimental Mechanics (SEM)

Internships

Taiwan Advanced Composite Center, Taichung, Taiwan Summer 2013

- Involved in the main production line from material storage and preparation, to lay-up, curing, out of autoclave (OOA) process production, machining, inspection, painting and assembly
- Engaged in composite material parts damage inspections and Boeing inspection on composite plies lay-up procedures

China Airlines Engineering and Maintenance Organization, Taoyuan, Taiwan Summer 2012

- Participated in the maintenance organization, including line maintenance, engine maintenance, fleet management, and inventory management

PUBLICATIONS

Journal Articles

- [1] **Chu, J.M.**, Lim, B.H., Claus, B., O'Brien, D., Fezzaa, K., Sun, T., and Chen, W. Mechanical Behavior fiber-matrix interfacial transverse debonding (under preparation)
- [2] Li, Y., **Chu, J.M.**, and Chen, W. Mechanical Response of Precursor and Post-Draw UHMWPE Fiber under Dynamic Uniaxial and Biaxial Shear/Tension Loadings (under preparation)
- [3] **Chu, J.M.**, Claus, B., Lim, B.H., O'Brien, D., Fezzaa, K., Sun, T., and Chen, W. Rate Effect of Fiber-Matrix Interfacial Transverse Debonding Behavior of SC-15 Epoxy and S-2 Glass Fiber (under preparation)
- [4] Lim, B. H., **Chu, J.M.**, Claus, B., Nie, Y., and Chen, W. Critical Velocity of High-Performance Yarn Transversely Impacted by Razor Blade (under preparation)
- [5] Lim, B. H., **Chu, J.M.**, and Chen, W. (2018) Mechanical Behavior of High-Performance Yarn Transversely Loaded by Different Indenters. *Fibers*, 6, 69.
- [6] Nie, Y., Parab, N., **Chu, J.M.**, Sun, T., Fezzaa, K., and Chen, W. (2018) Dynamic Crack Propagation from a Circular Defect in a Unidirectional CFRP Composite. *Journal of Composite Materials*, 0021998318797394.
- [7] **Chu, J.M.**, Claus B., Parab, N., O'Brien, D., Fezzaa, K., Sun, T., and Chen, W. (2018) Visualization of Fiber-Matrix Interfacial Shear Debonding. *Journal of Materials Science*, 53(8), 5845-5859.
- [8] **Chu, J.M.**, Claus, B., and Chen, W. (2017). Mechanical Properties of Transgenic Silkworm Silk under High Strain Rate Tensile Loading. *Journal of Dynamic Behavior of Materials*, 3(4), 538-547.
- [9] Claus, B., **Chu, J.**, Beason, M., Liao, H., Martin, B., and Chen, W. (2017). Dynamic Experiments using Simultaneous Compression and Shear Loading. *Experimental Mechanics*, 1-11.
- [10] Hudspeth, M., **Chu, J. M.**, ... and Chen, W. (2016). Effect of Projectile Nose Geometry on the Critical Velocity and Failure of Yarn Subjected to Transverse Impact. *Textile Research Journal*, 0040517516646040.

Conference Proceedings

- [1] Chu, J.M., Claus, B., Lim, B.H., O'Brien, D., Sun, T., Fezzaa, K., and Chen, W., 2018. American Society of Composites (Sept 2018). Visualization of Fiber/Matrix Interfacial Transverse Debonding. In Proceedings of the American Society for Composites—Thirty-third Technical Conference.
- [2] Chu, J.M., Claus, B., Parab, N., O'Brien, D., Fezzaa, K., Sun, T. and Chen, W., 2017. Visualization of Fiber/Matrix Interfacial Shear Debonding Mechanism at High Rate Loading. In Proceedings of the American Society for Composites—Thirty-second Technical Conference.
- [3] Nie, Y., Parab, N., Chu, J.M., Sun, T., Fezzaa, K., and Chen, W. 2017. Crack Propagation from a Circular Defect in a Unidirectional CFRP Composite under Dynamic Tension. In Proceedings of the American Society for Composites—Thirty-second Technical Conference.

Conference Presentations

- [1] American Society of Composites (ASC). Sept 2018. Visualization of Fiber/Matrix Interfacial Transverse Debonding. Seattle, WA.
- [2] ULITIMA. Sept 2018. Real-Time Visualization of Dynamic Fiber/Matrix Interfacial Debonding. Lemont, IL.
- [3] MACH. Apr 2018. Dynamic Visualization of Fiber/Matrix Interfacial Transverse Debonding. Annapolis, MD.
- [4] American Society of Composites (ASC). Oct 2017. Visualization of Fiber/Matrix Interfacial Shear Debonding Mechanism at High Rate Loading. West Lafayette, IN.
- [5] Society for Experimental Mechanics (SEM). Jun 2017. Visualization of Fiber/Matrix Interfacial Shear Debonding Mechanism at High Rate Loading. Indianapolis, IN.
- [6] MACH. Apr 2017. Visualization of Fiber/Matrix Interfacial Debonding Mechanism at High Rate Loading. Annapolis, MD.